

Ion Acceleration
driven by
High-Intensity Laser Pulses

*Dissertation der Fakultät für Physik
der Ludwig-Maximilians-Universität München*

vorgelegt von
Jörg Schreiber
aus Suhl

München, den 03.07.2006

1. Gutachter: *Prof. Dr. Dietrich Habs*

2. Gutachter: *Prof. Dr. Ferenc Krausz*

Tag der mündlichen Prüfung: 6. September 2006

Zusammenfassung

Die vorliegende Arbeit befaßt sich mit der Ionenbeschleunigung von Hochintensitätslaser-bestrahlten Folien. Mögliche Anwendungen dieser neuartigen Ionenstrahlen reichen von kompakten Injektoren für konventionelle Partikelbeschleuniger über die schnelle Zündung prekomprimierter Fusionstargets bis zur Onkologie und Radiotherapie mit Ionen. Darüber hinaus wird Protonenradiography schon heute zum Studium der Dynamik Lasererzeugter Plasmen mit ps-Zeitauflösung eingesetzt.

Im Rahmen dieser Arbeit wurde ein analytisches Modell entwickelt, basierend auf der Oberflächenladung, die durch die auf der Folienrückseite austretenden laserbeschleunigten Elektronen erzeugt wird. Dieses Feld wird für die Dauer des Laserimpulses τ_L aufrechterhalten, ionisiert Atome an der Folienrückseite und beschleunigt die Ionen. Die vorhergesagten Maximalenergien der Ionen E_m stimmen gut mit den experimentellen Resultaten dieser Arbeit und verschiedenener Gruppen weltweit überein (Abb. 1).

Neben Protonen, die aus Kohlenwasserstoffverunreinigungen auf den Folienoberflächen stammen, werden auch schwerere Ionen, wie zum Beispiel Kohlenstoff, beschleunigt. Mit der Schneidenmethode konnten neben der Verifikation der aus zahlreichen Messungen bekannten Quellgrößen von Protonen auch die Quellgrößen der verschiedenen Kohlenstoffladungszustände bestimmt werden. Aus der Unterdrückung hoher Ladungszustände weit entfernt vom Zentrum der Emissionszone konnte die radiale Feldverteilung des Beschleunigungsfeldes abgeleitet werden (Abb. 2), dessen radiale Ausdehnung die Größe des Laserfokus um zwei

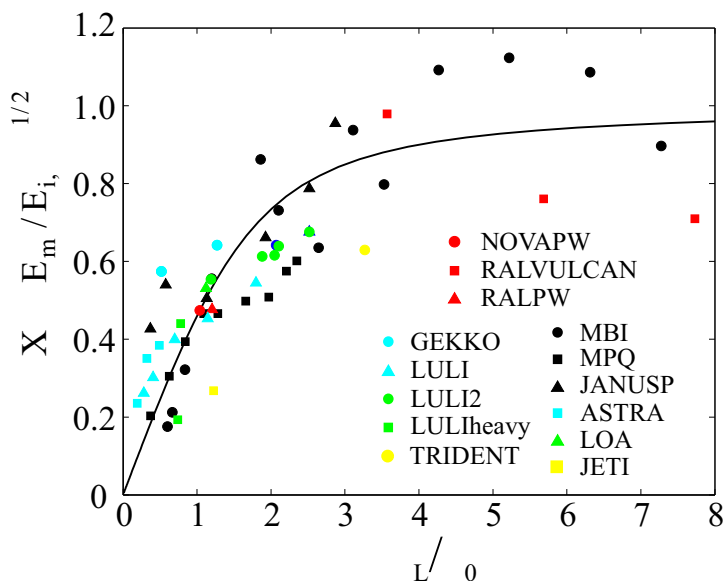


Figure 1: Vergleich experimenteller Ergebnisse mit dem analytischen Modell (Kurve). Die Symbole zeigen die von verschiedenen Gruppen experimentell bestimmten Maximalenergien E_m als Funktion der Dauer der Laserimpulse τ_L .

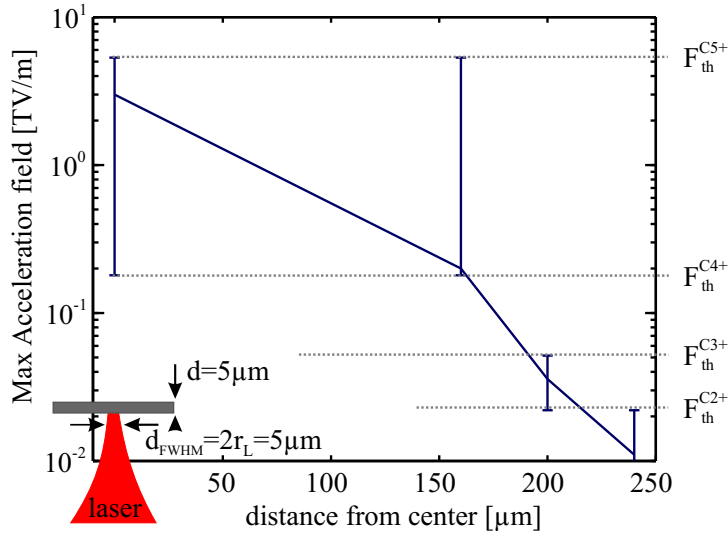


Figure 2: Radiale Feldverteilung an der Folierrückseite einer $d = 5 \mu\text{m}$ dicken Aluminiumfolie bestrahlt mit einem Laserimpuls mit einer Intensität von $2 \cdot 10^{19} \text{ W/cm}^2$ in einem Fokus mit $d_{FWHM} = 5 \mu\text{m}$ Durchmesser. Die mit den Fehlerbalken gekennzeichneten Grenzen markieren die Schwellen für sequenzielle Feldionisation F_{th} .

Größenordnungen übertrifft. Desweiteren konnte mit Hilfe von vergrabenen Schichten gezeigt werden, daß das elektrische Feld Ionen aus einer Tiefe von 50 nm erreichen kann. Aus diesen Einsichten wurde geschlußfolgert, daß monoenergetische Ionenstrahlen durch die Einschränkung der Quelle sowohl in ihrer Dicke ($< 50 \text{ nm}$) als auch transversal zu einer kleinen Fläche mit einem Durchmesser der Größdes Laserfokus ($< 10 \mu\text{m}$), erzeugt werden können. Dies bedeutet, daß alle Ionen die gleiche elektrische Feldstärke während ihrer Beschleunigung spüren.

In einigen Experimenten wurden die bestrahlten Folien geheizt, um die Kohlenwasserstoffverunreinigungen zu entfernen, so daß schwerere Ionen von Lithium bis Wolfram effektiv beschleunigt werden konnten. Die beobachteten Ladungsverteilungen ähnelten Gleichgewichtsladungsverteilungen, wie man sie von Ionen hinter einem Strippermaterial erwartet. Da der Einfluß des Restgases in der Experimentierkammer ausgeschlossen werden konnte, muß sich die Gleichgewichtsladungsverteilung nahe der Folierrückseite, wo auch die eigentliche Beschleunigung stattfindet, einstellen.

Die Erkenntnisse dieser Arbeit führten zu einem verbesserten Verständnis des Prozesses der Ionenbeschleunigung mit Hochintensitätslasern wie sie heutzutage verwendet werden [1, 2, 3, 4, 5, 6, 7, 8, 9, 10, 11, 12]. Die neuartigen Ionenstrahlen könnten ihre Anwendung in der Radiotherapie finden. Die dafür notwendigen monoenergetischen Protonen mit Energien von 140 MeV können mit den künftig weit verbreiteten PW-Lasersystemen erzeugt werden.

Abstract

Within the framework of this thesis the ion acceleration from foils irradiated by high-intensity laser pulses was studied. The application of such laser accelerated ion beams could reach from compact fast-ion injectors for conventional particle accelerators over fast ignition for inertial confinement fusion to oncology and radiotherapy with ion beams. Proton imaging of laser produced plasmas is one application which had already great impact in exploring laser plasma dynamics with ps time resolution. For all applications it is necessary to understand the physical processes to be able to control the properties of the ion beam.

In this work an analytical model could be derived which is purely based on the surface charge created by the laser accelerated electrons which pass the target and exit into vacuum at the rear side. The field of this surface charge is maintained for the duration of the laser pulse τ_L and, after field-ionizing atoms at the target rear side, accelerates the ions. The predicted maximum ion energies E_m are in good agreement with experimental results obtained in this work and by other groups all over the world (Fig. 3). The found scalings are also confirmed by recent PIC simulations.

In addition to protons also the acceleration of heavier ions was investigated. The appearance of different charge states raised questions about their origin for a long time. In all experiments heavy ions such as carbons are accelerated along with protons. Using the knife edge method not only the large source sizes for protons could be verified but also the source sizes of the different carbon charge states

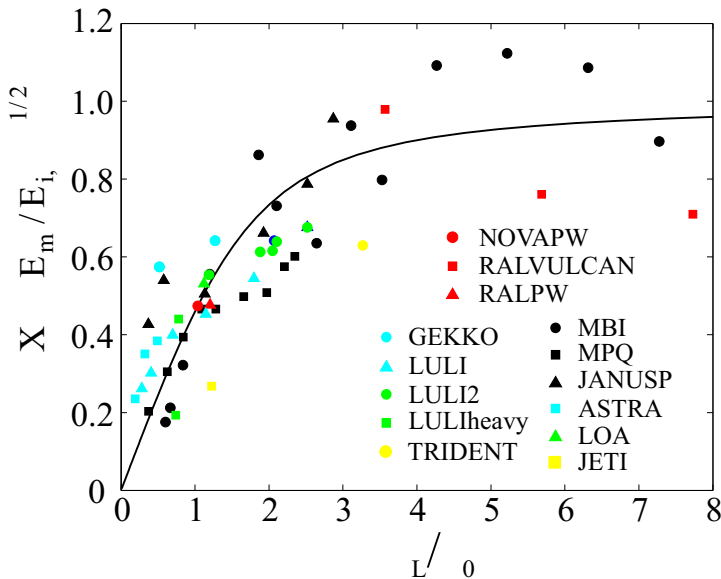


Figure 3: Comparison of experimental results with analytic model (solid line). The symbols denote the experimentally obtained maximum ion energies E_m from different laser systems all over the world as a function of the laser pulse duration τ_L .

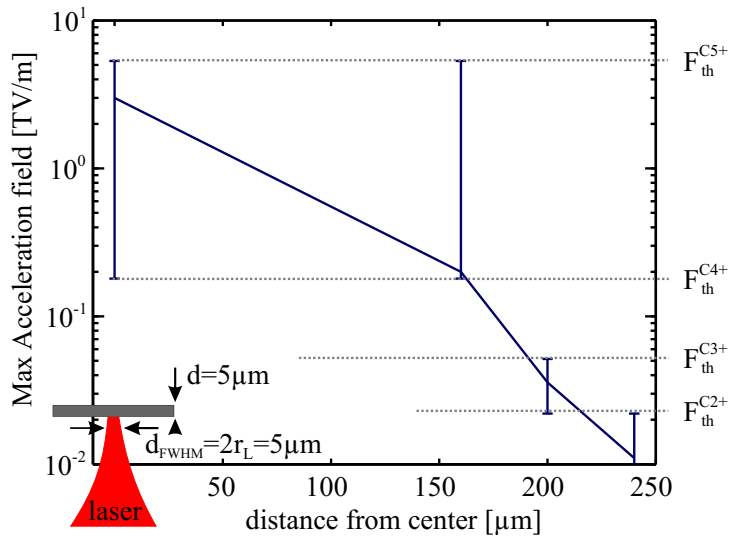


Figure 4: Radial profile of the maximum field at the rear side of a $d = 5 \mu\text{m}$ thick aluminum target irradiated by a laser pulse with an intensity of $2 \cdot 10^{19} \text{ W/cm}^2$ in a focal spot of $d_{FWHM} = 5 \mu\text{m}$ full width at half maximum diameter. The limits marked by the error bars represent the threshold fields for sequential field ionization F_{th} .

could be estimated. The suppression of high charge states at large distances from the center of the emission zone could be used to derive a radial field distribution (Fig. 4). The radial extension was found to exceed the focal spot size by 2 orders of magnitude. Additionally the longitudinal extension of the electric field inside the target was estimated by using buried layers. It was found that the field reaches ions in the target up to a depth of 50 nm. These insights led to the understanding of how mono-energetic ion beams can be produced by constraining the source to a thin layer ($< 50 \text{ nm}$) and a small area with a diameter of the order of the laser focal spot ($< 10 \mu\text{m}$). Thus, the field does not considerably change over the source layer, i.e., all ions are accelerated in the same field.

A number of experiments were performed with heated targets where all hydrogen contaminants were removed thus allowing for an effective acceleration of heavier ions reaching from lithium to tungsten. The observed charge state distributions resembled equilibrium charge state distributions as one would expect from ions passing a stripper medium. The influence of the residual gas in the target chamber could be ruled out, concluding that the charge state distribution arranges near the rear side of the foil where also the acceleration takes place.

The insights attained in this work did lead to a good understanding of the process of ion acceleration with nowadays high-intensity laser pulses [1, 2, 3, 4, 5, 6, 7, 8, 9, 10, 11, 12]. Possible applications are seen in the radiotherapy with ion beams where the required mono-energetic proton beams with energies of 140 MeV could be achieved with PW-class lasers.

Contents

1	Introduction	1
1.1	History of laser-ion acceleration	1
1.2	Recent results	2
1.3	Thesis structure	3
2	Theory	5
2.1	Laser-electron interaction	5
2.1.1	Interaction with a single electron	5
2.1.2	Interaction with a plasma	7
2.2	Ion acceleration	8
2.3	Numerical models	13
2.3.1	Particle-in-cell simulations	13
2.3.2	Hybrid and other numerical models	14
2.3.3	Plasma expansion model (PEM)	14
3	Analytic Model	17
4	Experimental Setup and Diagnostics	23
4.1	General setup and laser systems	23
4.2	The Thomson parabola spectrometer	25

4.3	The detector	28
4.4	Typical spectrum	30
5	Experiments	32
5.1	Variation of experimental parameters	32
5.2	Source-size measurements	36
5.3	Ion acceleration from buried layers	39
5.4	Mono-energetic ion beams	41
5.5	Acceleration of heavy ions ($Z>1$)	42
6	Discussion	44
6.1	Potential of the analytical model	44
6.1.1	Comparison with published results	44
6.1.2	The optimal pulse duration	45
6.1.3	Heavy Ions in the analytical model	47
6.1.4	Limitations of the analytical model	48
6.2	Interpretation of the scraper measurement	49
6.2.1	The radial field profile	49
6.2.2	The source sizes	51
6.3	Ion acceleration from buried layers	53
6.4	Mono-energetic ion beams	54
6.5	Charge state distributions of heavy ions	55
6.5.1	The influence of the residual gas	56
6.5.2	The target rear side	56
7	Summary and Perspectives	59

<i>CONTENTS</i>	iii
7.1 Results of the thesis	59
7.2 Future laser development	60
7.3 Perspectives of laser-ion acceleration	61
7.3.1 Double layer targets	62
7.3.2 The influence of the target size	62
7.3.3 The transition to the laser-piston regime	66
7.4 Application of laser accelerated ion beams	67
A Charge transfer	71
Literature	73

Chapter 1

Introduction

1.1 History of laser-ion acceleration

The interaction of light at high intensities with matter has been studied since the first realization of the laser in 1960 [13], although the meaning of “high intensity“ drastically changed over the last decades (Fig. 1.1). Based on the Q-switch technique it became possible to produce short (ns) and powerful (MW) laser pulses. The ions emitted from the plasmas produced by these giant pulses reached energies in the keV-range [14]. The emission was rather undirected and unordered and could be explained by self-similar plasma expansion models [15]. In 1985, the invention of the chirped pulse amplification (CPA) technique by Strickland and Mourou [16] provided for the next milestone in increasing the power of laser pulses. It is worth noting that the optical pulse stretching and compression with diffraction gratings was demonstrated by Treacy [17] in 1969 already. These techniques were essential for CPA which, in turn, provided for the field of relativistic laser-plasma physics. The term “relativistic“ marks the fact that electrons in the laser focus are accelerated close to the velocity of light within one laser period. This happens for light intensities I_L exceeding 10^{18} W/cm² for common laser wavelengths λ_L of about 1 μ m. The corresponding intensity for the relativistic motion of protons in the laser field exceeds 5×10^{24} W/cm².

The new regime of laser-electron interaction also reflects in the ion acceleration processes. In addition to even higher ion energies, the ion beam characteristics differed tremendously from the early ion beams emitted from nanosecond laser-plasmas, i.e., they are highly directed and have a small transverse emittance. The process of ion acceleration is understood best in the concept of the Target Normal Sheath Acceleration (TNSA). Nowadays, “high power“ addresses the Multi-TW

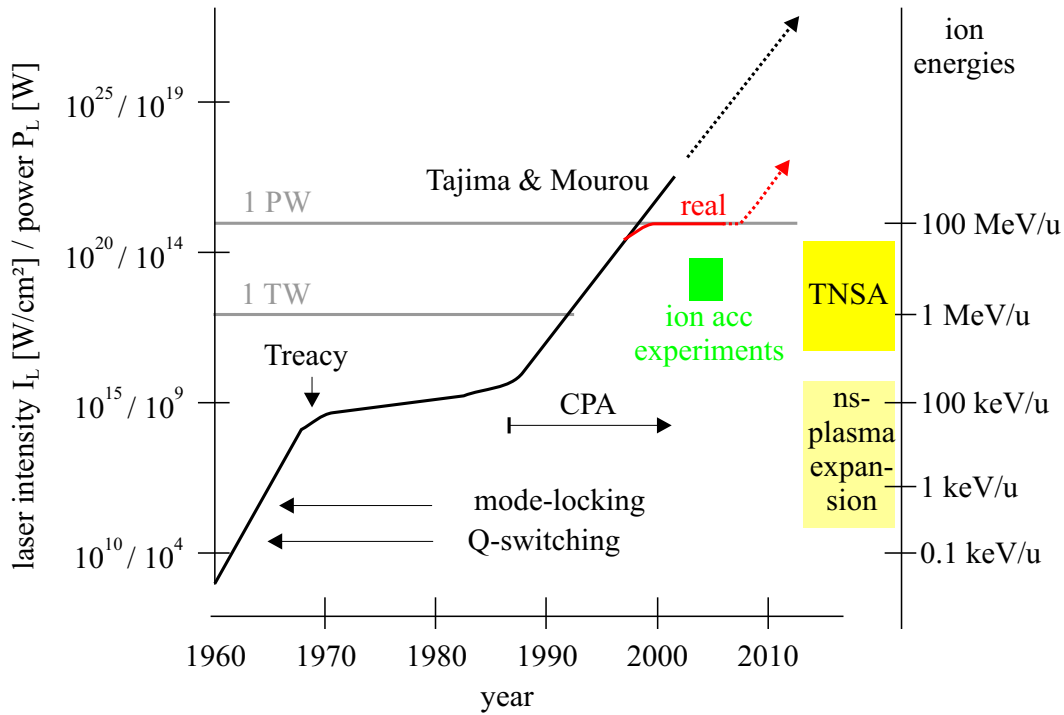


Figure 1.1: History of high intensity/power laser pulses. The solid black curve is taken from Tajima and Mourou [18, 19] and depicts the development of the laser intensity and power resp. since the invention of the laser. This trend needed to be corrected (red line) since the 1PW threshold was not overcome since the first realization at the Lawrence Livermore Laboratory, USA. CPA was successfully applied to increase the laser power in 1989, 4 years after the proposal of Strickland and Mourou [16], although the possibility of stretching and compression of broad band laser pulses was shown in 1969 already by Treacy [17]. The right column shows the evolution of the ion energies observed in laser plasma experiments with the respective intensities. The green rectangle marks the power region where the experiments discussed in this thesis were performed.

and even PW-regime and the term “short pulses“ stands for laser pulse durations below one pico second. The intensities produced by focussing these high-power laser pulses ($10^{19} - 10^{21} \text{ W/cm}^2$) exceed the first giant pulses by ten orders of magnitude and the obtained ion energies were pushed over six orders of magnitude up to 100 MeV during the last 40 years (Fig. 1.1).

1.2 Recent results

Ion acceleration from high-intensity laser irradiated foil targets has been extensively studied during the last decade. Since hydrogen is always present on the target surfaces, namely in hydrocarbon and water contaminants, protons were the

subject of interest in most of the experiments. The emitted ion and, in particular, proton pulses reached large particle numbers between 10^{10} and 10^{13} with energies in the MeV- [20, 21] and multi-MeV-range [22, 23, 24, 25] and are tightly confined in time (\sim ps) and space (source radius few μm). In recent experiments, the high quality in terms of emittance of proton beams emitted from the rear side of laser irradiated thin foils was proven [26, 27, 28]. The outstanding characteristics of the laser accelerated ion beams triggered speculations about their applications in nuclear physics. They have been considered as an ion source for the injection into a conventional particle accelerators (see, for example, ref [29]) and for fast ignition [30]. More practically, potential applications of laser accelerated ions in medicine, i.e., for ion-cancer-therapy were discussed [31, 32]. In fundamental research laser-accelerated protons are successfully used for diagnosing the electromagnetic fields in overdense laser-produced plasmas with a picosecond time resolution [33, 34]. The accelerating electric field as high as several TV/m is set up by the laser accelerated electrons which propagate through the target and exit on the target rear side. Therefore attempts have been made to diagnose the transport of the large electron current (MA) through solid targets by measuring the ion properties [35]. Besides protons, also heavier ions originating from the contaminant layers or the target itself are accelerated in the huge electric field [12, 22, 36]. Heavy ion acceleration up to 5 MeV/u could be demonstrated when the light protons were removed by heating the targets before laser irradiation [37, 38, 8]. Those ions show similar characteristics as protons in terms of ion numbers and beam quality [3].

The energy distributions of the accelerated ions observed so far are broad and have an exponential shape. An important feature of the observed ion spectra is the hard cut-off at a certain maximum ion energy which is observed in all experiments concerning ion acceleration from high-intensity laser irradiated foils. The maximum ion energy thus is widely used to characterize the ion acceleration and to study its dependence on different parameters (see, for example, refs. [11, 39, 5]). Just recently mono-energetic ion beams from laser irradiated foils have been observed by the two groups around Hegelich *et al.* [4] and Schwoerer *et al.* [40] for the first time. This observation is very encouraging for further developments and the applicability of laser accelerated ions.

1.3 Thesis structure

The theoretical descriptions of the ion acceleration from laser irradiated thin foils are mainly based on numerical simulations such as particle-in-cell (PIC) models

[41, 42], fluid [15] or hybrid models [6]. A short introduction to these methods is given in sections 2.3.1 and 2.3.2. Analytical approaches are meant to describe the plasma expansion process by solving the Vlasov-equation in the quasi-neutral approximation [43, 44], or adapting self-similar solutions of the expansion process to fit numerical results of plasma expansion models (PEM, sec. 2.3.3 [45]).

In the scope of this work a simple analytic approach [1] was developed (chapter 3) which treats the accelerated ions as light test particle in a quasi-static electric field set up by the surface charge on the target rear side. This model allows to calculate the observed maximum ion energies in many experimental studies during the last decade.

Following the explanation of the experimental methods (chapter 4) the experimental chapter addresses on the properties of the ion source. The dependence of proton acceleration on different experimental parameters, i.e., laser intensity, pulse duration, energy and target thickness is analyzed (sec. 5.1). The extension of the accelerating electric field is determined both transversely using the knife edge method (sec. 5.2) and longitudinally inside the target probing with buried ion layers (sec. 5.3). These measurements for field characterization are needed to understand the conditions necessary for the creation of mono-energetic ion beams (sec. 5.4). A very complicated issue is the occurrence of different charge states of the accelerated heavy ions (charge number $Z > 1$) as already discussed by Hegelich [36]. Experiments with various ions ranging from lithium to tungsten are described in Sec. 5.5.

In chapter 6 the experimental results will be discussed. The analytical model described in chapter 3 nicely reproduces the obtained ion energies in Sec. 6.1 and conclusions for the perfect laser conditions are drawn. Sec. 6.2 discusses the results from the scraper measurement and the transverse shape of the accelerating electric field is estimated. Its longitudinal range is deduced from the measurements with buried ion layers in Sec. 6.3. Sec. 6.4 concentrates on the mono-energetic ion beams while Sec. 6.5 discusses the appearance of the peaked ion charge state spectra from the heavy ion measurements.

Finally, chapter 7 summarizes the main results of this work and gives a perspective of laser-ion acceleration and its possible applications.

Chapter 2

Theory

In order to understand the process of ion acceleration by high-intensity lasers some relevant quantities and concepts need to be introduced. The huge electric field of the discussed laser pulses (TV/m) immediately ionizes the atoms of the irradiated material. This results in a plasma, a state where outer electrons are not longer bound to their nuclei. Because of their low mass the primary interaction is between laser light and electrons.

2.1 Laser-electron interaction

2.1.1 Interaction with a single electron

It is worth to consider the case of a single electron in the transverse electromagnetic field of a laser pulse. Due to the electric field component with amplitude F_{L0} the electron feels a force

$$K_{\perp} = eF_{L0}\cos(\omega_L t) \quad (2.1)$$

which oscillates with the laser angular frequency $\omega_L = 2\pi/\lambda_L$. In a non-relativistic description the velocity amplitude of this oscillation is

$$v_{\perp} = \frac{eF_{L0}}{m\omega_L}\sin(\omega_L t) \quad (2.2)$$

where e and m are the electrons charge and mass, respectively. At the same time the electron is pushed forward due to the force

$$K_{\parallel} = ev_{\perp}B_L = e\frac{v_{\perp}}{c}\frac{F_{L0}}{2} \cdot \sin(\omega_L t) \quad (2.3)$$

with B_L being the magnetic field component of the laser and c the velocity of light. The laser-electron interaction is called relativistic if the transverse maximum

electron velocity (Eq. (2.2)) approaches c or, more precisely, if the longitudinal force K_{\parallel} exceeds the transversal force K_{\perp} which suggests the definition of the dimensionless laser amplitude

$$a_L \equiv \frac{K_{\parallel}}{K_{\perp}} = \frac{eF_{L0}}{mc\omega_L}. \quad (2.4)$$

For laser systems available today and relevant for this work it is approximately $3 < a_L < 30$. The corresponding amplitudes for electric and magnetic fields then read

$$F_{L0} = a_L \frac{2\pi mc^2}{e\lambda_L} = \frac{a_L}{\lambda_L[\mu\text{m}]} \cdot 3.2 \times 10^{12} \text{V/m} \quad (2.5)$$

$$B_{L0} = a_L \frac{2\pi mc}{e\lambda_L} = \frac{a_L}{\lambda_L[\mu\text{m}]} \cdot 1.07 \times 10^4 \text{T} \quad (2.6)$$

and the intensity is given by

$$I_L = \frac{1}{2} \epsilon_0 c F_{0L}^2 = \frac{a_L^2}{\lambda_L^2[\mu\text{m}^2]} \cdot 1.37 \times 10^{18} \text{W/cm}^2 \quad (2.7)$$

for linearly polarized light. For circular polarized or unpolarized light I_L would have to be multiplied by a factor of 2. Experimentally the laser intensity

$$I_L = \frac{E_L}{\tau_L \pi r_L^2} \quad (2.8)$$

is measurable by determining the laser pulse energy E_L , its duration τ_L and its spot radius r_L . Therefore it is convenient to rewrite Eq. (2.7) to define

$$a_L^2 = \frac{2}{\pi} \frac{I_L \lambda_L^2[\mu\text{m}^2]}{P_R} \quad (2.9)$$

where $P_R = mc^3/r_e = 8.71 \text{GW}$ is the natural relativistic power unit ($r_e = e^2/(4\pi\epsilon_0 mc^2) = 1.4 \text{fm}$ is the classical electron radius).

Up to now the considerations were restricted to a plane wave. In this case an electron initially at rest does not gain energy and will be at rest again after the laser has passed. In a more realistic treatment the laser is focussed to focal spot diameters of several μm and its transversal shape could be, for example, gaussian. In this case one can imagine an electron in the laser spot which is accelerated away from the focal region due to the electric field. When the electric light field changes its sign the force driving the electron back to the center will be smaller because of the transversely varying field amplitude, thus, with every laser cycle the electron is pushed more and more out of the high intensity region and gains energy. This effect can be described by an electron running down the ponderomotive potential of the laser

$$\Phi_{pond} = \frac{mc^2}{4\bar{\gamma}^2} a_L^2 \quad (2.10)$$

thus gaining the energy

$$W_e = mc^2(\bar{\gamma} - 1) \quad (2.11)$$

where

$$\bar{\gamma} = \sqrt{1 + a_L^2/2}. \quad (2.12)$$

is the cycle-averaged gamma factor [46] which is of the order of 2-20 for realistic laser parameters. The real electron emission pattern is radially symmetric [47] and not in the polarization plane of the laser as could be expected by the simple picture explained above.

2.1.2 Interaction with a plasma

As mentioned above the electric field of the laser pulses discussed in this context are much higher than the fields which bind the outer electrons to their nuclei. Thus, already pre-pulses or the pedestal of the laser pulse are intense enough ($> 10^{12}$ W/cm²) to ionize the material so that the highly intense laser pulse interacts with a preformed plasma. When electrons are pushed by the laser pulse they feel a repelling force from the nearly immobile ion background and oscillate with the electron plasma frequency

$$\omega_p = \sqrt{\frac{e^2 n_e}{\epsilon_0 m \bar{\gamma}}}. \quad (2.13)$$

The refractive index of a plasma with electron density n_e reads

$$n_p = \sqrt{1 - \frac{\omega_p^2}{\omega_L^2}} \quad (2.14)$$

and is smaller than 1 for $\omega_L > \omega_p$ allowing light to propagate with phase velocity $v_{ph} = c/n_p$ and group velocity $v_g = cn_p$. For $\omega_L < \omega_p$ the refractive index is purely imaginary expressing that light can not penetrate. The transition between these two scenarios happens for $\omega_p = \omega_L$ at the critical density

$$n_c = \frac{\epsilon_0 m \bar{\gamma} \omega_L^2}{e^2}. \quad (2.15)$$

The interaction of the laser with the plasma electrons depends on many parameters and is not the subject of this thesis. Nevertheless, since the laser accelerated electrons are responsible for the ion acceleration as will be shown later it is worth to summarize the most important electron acceleration mechanisms.

The ponderomotive acceleration of electrons is present as soon as high intense laser light interacts with a plasma. The electrons acquire an exponential energy

distribution with a mean energy of [48]

$$k_B T_e = mc^2 \left(\sqrt{1 + a_L^2} - 1 \right) \quad (2.16)$$

very similar to the kinetic energy obtained from Eq. (2.11).

When the laser propagates through a plasma of low density ($n_e \approx 10^{17} - 10^{19}/\text{cm}^3$) the laser ponderomotively pushes the electrons. The slow reaction of the plasma (Eq. (2.13)) favors the build up of plasma density modulations which move with the group velocity of the laser. Electrons can be caught in the corresponding electric field of the laser wake and are accelerated [49]. Recently it could be shown that for certain circumstances the laser wake field acceleration is transferred into the bubble regime where the energy spectra of the accelerated electrons are not broad and exponential anymore but become mono-energetic [50, 51, 52].

Electrons can also be efficiently accelerated near the critical surface where the electron density approaches n_c and the laser can not propagate any further and is reflected. If the laser is p-polarized and incident under an angle it pulls out electrons into the vacuum. After one half cycle the electrons are repelled back and are smashed into the solid where the field of the laser can not reach them anymore. The electrons gain energy during the half period they spent in vacuum giving the name vacuum heating [53].

2.2 Ion acceleration

Strictly speaking, the notion ion acceleration with high intensity laser pulses is not warrantable. In fact, the field quantities for electrons derived above (Eq. (2.4)-(2.7)) can be applied to ions. Replacing the electron mass m by, for example, the proton mass m_p results in

$$F_{L0,p} = a_{L,p} \frac{2\pi m_p c^2}{e\lambda_L} = \frac{a_{L,p}}{\lambda_L [\mu\text{m}]} \cdot 5.9 \times 10^{15} \text{V/m} \quad (2.17)$$

$$B_{L0,p} = a_{L,p} \frac{2\pi m_p c}{e\lambda_L} = \frac{a_{L,p}}{\lambda_L [\mu\text{m}]} \cdot 1.9 \times 10^7 \text{T} \quad (2.18)$$

$$I_{L,p} = \frac{1}{2} \epsilon_0 c F_{0L,p}^2 = \frac{a_{L,p}^2}{\lambda_L^2 [\mu\text{m}^2]} \cdot 4.6 \times 10^{24} \text{W/cm}^2. \quad (2.19)$$

With intensities available today ($I_L = 10^{18} - 10^{21} \text{W/cm}^2$, $\lambda_L \approx 1 \mu\text{m}$) the ions hardly move in the electric field of the laser. As soon as the laser starts to tear off the electrons its $e\vec{v} \times \vec{B}_L$ -force (Eq. (2.3)) pushes electrons forward and electric

fields evolve due to charge separation. These longitudinal fields can be as high as the electric field of the laser itself but are stationary for the laser pulse duration, which is why they are called quasi-static. Different regimes for ion acceleration were discussed and investigated experimentally, namely the plasma thermal expansion into vacuum [54, 15, 45], Coulomb explosion of strongly ionized clusters [55], transverse explosion of a self-focussing channel [56] and the ion acceleration in the strong charge separation field caused by a strong quasi-static magnetic field [57]. In this present work the ion acceleration from the rear side of high intensity laser irradiated foils will be discussed and is qualitatively explained by the target normal sheath acceleration (TNSA) mechanism [42] which is explained in Fig. 2.1.

In the process of chirped pulse amplification (CPA) parasitic effects such as amplified spontaneous emission (ASE) or spectral modulations favor the formation of pre-pulses which are intense enough ($> 10^{12} \text{ W/cm}^2$) to ionize the target and form a pre-plasma. Thus, the main laser pulse interacts with a plasma with an exponential density profile at the target front side depicted by the ramp in Fig. 2.1. The solid target with ion density n_s is assumed to be q_s -fold ionized. The characteristic length or scale length in which the electron density drops from the solid ($q_s n_s \approx 10^{23} / \text{cm}^3$) to the critical density ($n_c \approx 10^{21} / \text{cm}^3$, (Eq. (2.15)) is of the order of several μm . As mentioned above the laser can propagate to the point where the density becomes critical, the critical surface, and there it is reflected. The electrons are accelerated in forward direction while the ions initially remain at rest so that an electric field F_{front} evolves due to the charge separation (Fig. 2.1). Thus, at the target front side ions can be accelerated (see ref. [58] and ref. [59] for measurement and theory), although this process is not relevant for the ion acceleration experiments within the scope of this work.

The laser accelerated fast electron bunch travels through the foil while it is considered to be dynamically shielded by the cold target electrons, which makes the inner part field-free. The transport mechanisms is still subject of investigation and beyond the scope of this work. Assuming an opening angle θ ($\approx 25^\circ$) for the electron propagation through the foil with thickness d ($\approx 10 \mu\text{m}$) one can write the radius B of the electron bunch at the rear surface as

$$B = r_L + d \cdot \tan \theta \quad (2.20)$$

r_L being the radius of the laser focal spot ($\approx 3 \mu\text{m}$). Still the radius of the electron bunch which exits the foil is rather small ($\approx 10 \mu\text{m}$). The number of electrons N_e accelerated by the laser with energy E_L (1 – 10 J) can be estimated by

$$N_e k_B T_e = \eta E_L \quad (2.21)$$

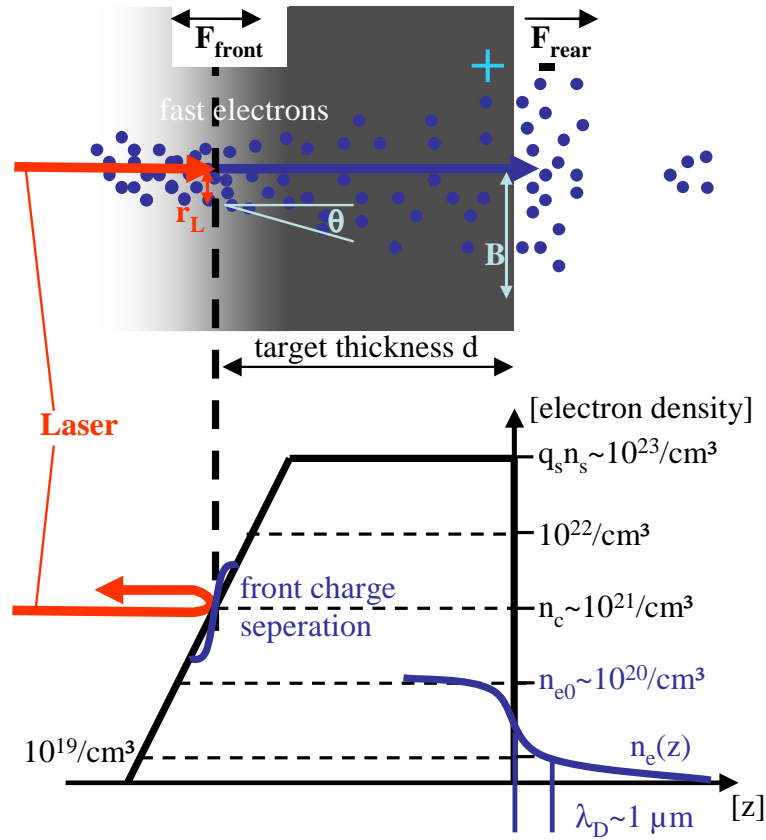


Figure 2.1: Scheme of the laser-solid interaction and ion acceleration. The laser with focal spot radius r_L propagates through the pre-plasma until it reaches the critical density n_c where it is reflected. The accelerated electrons form a bunch which propagates through the target of thickness d while spreading with a certain angle θ . At the target rear side the electrons bunch has spread over a circular area with radius B exhibiting the mean density n_{e0} . When the electrons exit the rear-side, they set up an electric field F_{rear} normal to the target surface, which forces them to turn around at the hot electron Debye-length λ_D resulting in the rear side electron density distribution $n_e(z)$. Atoms sitting at the surface are field-ionized and accelerated in target normal direction, giving the process its name, target normal sheath acceleration (TNSA).

with the mean electron energy of the exponential spectrum $k_B T_e$ (1 – 10 MeV) defined by Eq. (2.16) and the conversion efficiency η of laser energy into hot electrons (10 – 50%). With nowadays common high-intensity laser pulses electron numbers $N_e = 6 \cdot 10^{11} - 6 \cdot 10^{13}$ are accelerated within common laser pulse durations $\tau_L = 50 - 600$ fs. The resulting density of the hot electron bunch can be estimated to

$$n_{e0} = \frac{N_e}{c\tau_L\pi B^2} \approx 2 \cdot 10^{20} - 2 \cdot 10^{21} / \text{cm}^3. \quad (2.22)$$

Inserting Eqs. (2.16), (2.8), (2.9) and (2.20) into Eq. (2.22) the hot electron density

can be written as

$$n_{e0} = \eta \cdot \frac{n_c}{2} \cdot \frac{a_L^2}{\sqrt{1 + a_L^2} - 1} \cdot \frac{r_L^2}{(r_L + d \cdot \tan\theta)^2}. \quad (2.23)$$

Thus, the density of the hot electron pulse is much smaller than the density $q_s n_s$ of the target electrons. This supports the validity of the assumption that the electrons are shielded while they propagate through the target.

At this point it is worth to comment on the conversion efficiency η of laser energy into hot electron energy which is a crucial quantity and can depend on many parameters. Obviously, it is $0 < \eta < 1$. In experiments with foil targets irradiated by high-intensity laser pulses the dependence of η on the laser intensity I_L was studied by Yu *et al.* [60] for $I_L = 10^{16} - 10^{18}$ W/cm² and by Key *et al.* [61] for $I_L = 10^{18} - 3 \cdot 10^{19}$ W/cm². In both works it could be shown that η scales as $I_L^{3/4}$. The experimental results from [61] were fitted by the function

$$\eta = 1.2 \cdot 10^{-15} \cdot I_L^{3/4} \quad (2.24)$$

with I_L in W/cm². It should be emphasized that in case of lower intensities [60] η needs to be corrected by a factor of 2 only. However, as indicated by Hatchett *et al.* [24] who used $I_L = 3 \cdot 10^{20}$ W/cm², it is likely that η can not exceed 0.5 which, according to Eq. (2.24), is reached at an intensity of $I_L = P_L / (\pi r_L^2) = 3.1 \times 10^{19}$ W/cm².

When the electrons exit the rear surface an electric field evolves. The electrons with energies not sufficient to escape their self-induced field turn around and reenter the foil. This leads to an equilibrium situation where the electrons exiting the foils are compensated by electrons reentering. The blue curve in Fig. 2.1 schematically depicts their evolving density distribution $n_e(z)$ whose extension is determined by the hot electron Debye-length

$$\lambda_D = \sqrt{\frac{\epsilon_0 k_B T_e}{e^2 n_{e0}}}. \quad (2.25)$$

Substituting with Eqs. (2.16) and (2.23) reads

$$\lambda_D = \frac{\lambda_L}{\pi} \cdot \frac{1}{\sqrt{2\eta}} \cdot \frac{\sqrt{1 + a_L^2} - 1}{a_L} \cdot \frac{r_L + d \cdot \tan\theta}{r_L} \quad (2.26)$$

and delivers Debye-lengths of the order of the laser wavelength λ_L . The corresponding electric field at the target rear side is estimated by

$$F_0 = \frac{k_B T_e}{e \lambda_D} \quad (2.27)$$

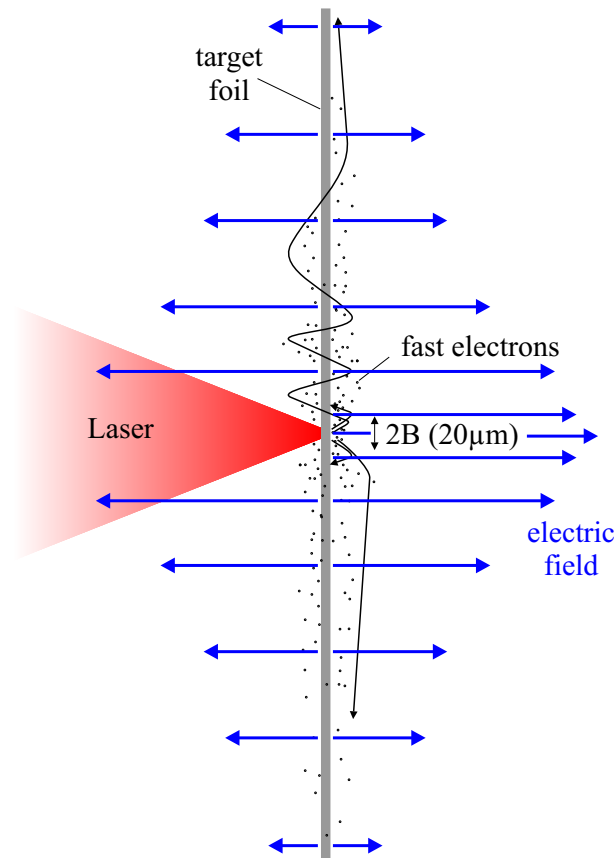


Figure 2.2: Scheme of the transversal spread of electrons causing the large transverse extension of the field. Electrons may be transversely deflected in the field at the rear side or they may be reflected in the fields building up at the surfaces giving rise to the phenomenon of recirculation.

Introducing the dimensionless field $a_0 = eF_0/mc\omega_L$ and using Eq. (2.16) and (2.26) delivers

$$a_0 = a_L \cdot \sqrt{\frac{\eta}{2}} \cdot \frac{r_L}{r_L + d \tan \theta} \quad (2.28)$$

expressing that the field at the target rear side is of nearly the same strength as the laser field itself (TV/m) which is strong enough to field ionize atoms and to accelerate the ions to energies of several MeV/u. The field is pointed normal to the target rear side giving the process its name target normal sheath acceleration (TNSA).

Although the radius of the electron bunch which exits at the target rear side is only of the order of several $10 \mu\text{m}$ the field at the rear side extends over hundreds of μm . This could be caused by electrons which are transversely deflected in the field or spread while they recirculate through the target (Fig. 2.2). Those effects are not fully understood yet but appear in all source size measurements as will be described in Sec. 5.2. Due to the recirculation [39] the accelerating electric field

is also maintained for times longer than the laser pulse duration, i.e., until the electrons are stopped. However, this has no strong influence on the maximum ion energy but may be reflected in the observed energy distributions of the ions.

The following sections address theoretical models used for the quantitative explanation of the ion acceleration processes. The numerical models (PIC, hybrid models and PEM) are reviewed in Sec. 2.3. Chapter 3 is dedicated to a self-evident analytical model which was derived within the scope of this work and explains the maximum ion energies observed in a variety of experiments [1].

2.3 Numerical models

2.3.1 Particle-in-cell simulations

Particle-in-cell (PIC) simulations were used for the theoretical investigation of laser-plasma interaction for a long time. The volume is described by a discrete grid. On this grid the Maxwell equations are solved with certain boundary conditions. The particles like electrons and ions are summarized to macro-particles each representing millions of real particles. The particle dynamics is treated by solving the equations of motion in the fields. The particles produce currents which, in turn, react on the fields via the Maxwell equations. For laser-plasma interaction at low densities, e.g. gases, PIC-methods could explain the underlying processes best and have become one of the most important tools to describe the underlying processes (see, for example, refs. [50, 51, 52]). The extension to higher densities became possible with growing computer capabilities. Still it is very time and computer memory consuming to simulate the real solid density in a sufficiently large volume with three-dimensional geometry. Moreover, in high density plasmas hard collisions as well as ionization and recombination processes play a major role which are usually insufficiently modelled in PIC codes. Some of the effects can be included by using empirical models like the Lotz-formula for collisional ionization and the WBK-model for field ionization (see [62] and references therein). However, even if there are limitations in the applicability of the PIC-method, it provides a powerful tool to get insight into physical phenomena and to explain experimental results [41, 27, 63].

2.3.2 Hybrid and other numerical models

The insufficiency of PIC models in describing high densities can be overcome only by improving the spatial resolution of the computing grid up to a nanometer level, which also leads to an increase of the number of simulated particles. For solid densities, these simulations are very time consuming. An additional problem when simulating solid targets is the low number of fast electrons which interact with the laser pulse. A large number of target electrons need to be taken into account to resolve the fast electrons. One alternative method to avoid these problems is a hybrid code. Here, the low number of fast moving particles (electrons) are treated as quasi-particles within a PIC-model. The behavior of the cold target electrons is described within a fluid model, thus no single particles are considered, but they are treated as a continuous electron background. This type of numerical model works well as long as the fast electron number is much lower than the number of background electrons, which is true for nowadays laser powers. One example, where a hybrid code was used to describe laser ion acceleration experiments is given by Honrubia *et al.* [6].

A totally different approach is based on a hierarchical tree algorithm as used by Gibbon [64]. The field acting on a certain particle is calculated from all other particles in the simulation box without using a grid. This actually is the most natural approach, but also the most time consuming. The problem would grow with the square of the number of particles N , but with the trick, that distant particles are summarized to charge groups whose multipole expansions are calculated, the problem complexity can be reduced to $N \log N$. The clear advantage of such a code is that particles close to each other feel the real coulomb potential of their neighbors so that hard collisions are intrinsically described. Still, so far, the applicability to real experiments was not extensively shown yet.

2.3.3 Plasma expansion model (PEM)

The ion acceleration on the rear surface of a laser irradiated foil was treated like a plasma expansion into vacuum by Mora [45] who applied the numerical method proposed by Crow *et al.* [15]. The starting conditions (Fig. 2.3) are a step-like density profile for ions with density $n_{i0} = n_{e0}/q_i$ where n_{e0} is the density of the laser accelerated electron bunch (Eq. (2.22)). The electron density is in thermal equilibrium with the quasi-static electric potential $\Phi(z)$, expressed by

$$n_e(z) = n_{e0} \exp [e\Phi(z) / (k_B T_e)] \quad (2.29)$$

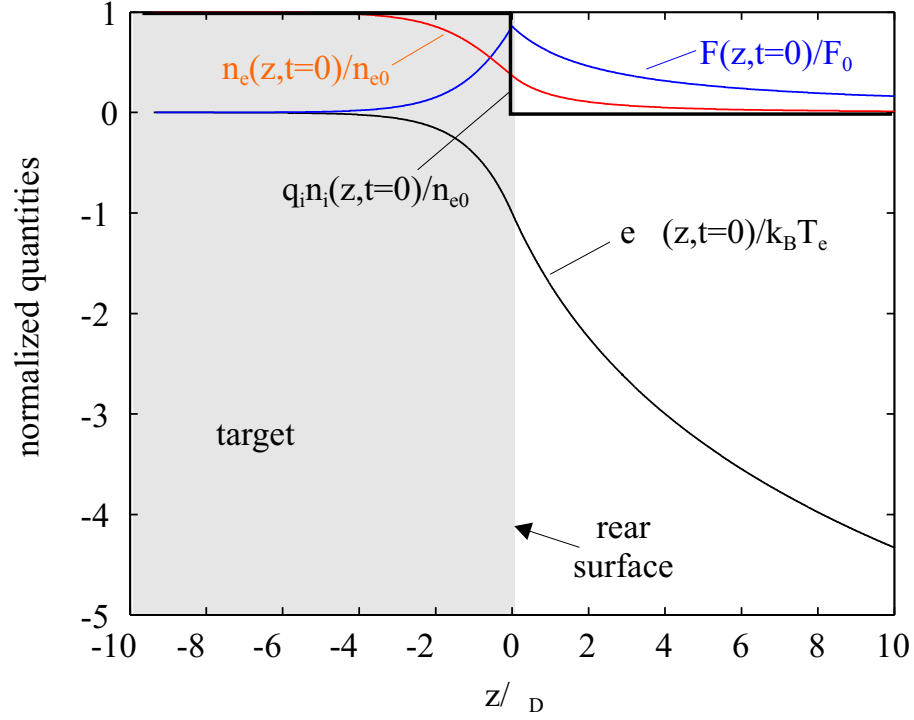


Figure 2.3: Starting conditions for plasma expansion into vacuum [45, 15] for the potential Φ (black), the electron density n_e (red), and the electric field F normalized to $F_0 = k_B T_e / e \lambda_D$ (blue). Note that the maximum density $n_{e0} = q_i n_{i0}$ is the one of the hot electron bunch which is produced by the laser, not the solid density n_s .

where $k_B T_e$ is the mean energy of the hot electrons. This implies the boundary condition for the potential $\Phi \rightarrow -\infty$ for $z \rightarrow \infty$. The potential is defined by the Poisson equation $d^2 \Phi(z, t) / dz^2 = e / \epsilon_0 \cdot (n_e(z, t) - q_i n_i(z, t))$, where q_i is the ion charge number and $n_e(z, t)$ and $n_i(z, t)$ are the densities of the hot electrons and ions as they evolve in space and time. Note, that n_i is not the density of the target ions but the ion density which exactly compensates the hot electrons so that neutrality is maintained over the whole system. For the boundary conditions $d\Phi/dz = 0$, $\Phi = 0$ at $z \rightarrow -\infty$ and $d\Phi/dz = 0$, $\Phi \rightarrow -\infty$ at $z \rightarrow \infty$ the electron density $n_e(z, t = 0)$ and the potential $\Phi(z, t = 0)$ can be calculated by integration of Eq. (2.29) in the vacuum region ($z > 0$) and read

$$\frac{n_e(z, t = 0)}{n_{e0}} = \exp(-1) \cdot \frac{1}{\left(1 + \frac{z}{(2\exp(1))^{1/2} \lambda_D}\right)^2} \quad (2.30)$$

$$\frac{e\Phi(z, t = 0)}{k_B T_e} = -2 \cdot \ln \left(1 - \frac{z}{(2\exp(1))^{1/2} \lambda_D}\right) - 1 \quad (2.31)$$

with the hot electron Debye length λ_D defined by Eq. (2.25). For $z < 0$ the potential, and thus, the electron density can be calculated numerically (Fig. 2.3).

The plasma expansion is described by solving the continuity equation $\partial n_i(z, t)/\partial t + \partial n_i(z, t)v_i(z, t)/\partial z = 0$ and the force equation $\partial v_i(z, t)/\partial t + v_i(z, t)\partial v_i(z, t)/\partial z = -q_i e/m_i \partial \Phi(z, t)/\partial z$ in each time step, where $v_i(z, t)$ is the ion mean velocity and m_i is the ion mass. Details and results of these calculations are given in [45, 15].

According to Mora's model [45], the maximum ion energy can be calculated via

$$E_m^{PEM} = 2q_i k_B T_e \left[\ln \left(\tau + \sqrt{\tau^2 + 1} \right) \right]^2 \quad (2.32)$$

where $\tau = 0.43\omega_{pi}\tau_L$ is usually of the order of 1-10. The ion plasma frequency is given by $\omega_{pi} = \left(n_{i0} (q_i e)^2 / \epsilon_0 m_i \right)^{1/2}$, where $n_{i0} = n_{e0}/q_i$ is the plasma ion density prior to expansion and q_i the charge of the ions. Note, that n_{i0} used in the calculations is usually 3 orders of magnitude smaller than the density n_s of ions in a solid. The hot electron temperature T_e needs to be estimated by Eq. (2.16).

The plasma expansion model was widely used during the last years to explain experimental observations [11, 5]. Nevertheless, there are some inconsistencies within this approach which need to be mentioned. It seems arbitrary to choose $n_{i0} = n_{e0}/q_i$ to be the ion density prior to expansion which is much smaller (2-4 orders of magnitude) than the solid state density of typically $n_s = 10^{23}/\text{cm}^3$. Also the logarithmically diverging character of the maximum ion energy of Eq. (2.32) for large pulse durations τ_L appears unphysical. Last but not least, the mean electron energy $k_B T_e$ is needed for the evaluation of Eq. (2.32) which is usually calculated by Eq. (2.16). However, all these inconveniences could be overcome by an analytic approach derived within the scope of this thesis. This simple model is able to describe most of the experimental observations and will be derived in Chapter 3.

Chapter 3

Analytic Model

In this chapter an analytical model is derived which explains the maximum ion energy observed in a broad variety of experiments where high-intensity laser pulses interact with a thin foil. The accelerating field originates from the surface charge which is built up by hot electrons accelerated by the laser which exit the foil at its rear side. This model recently has been submitted to Physical Review Letters [1].

Consider N_e laser accelerated electrons in an electron bunch with length $L = c\tau_L$, where τ_L is the laser pulse duration. Transversely, the electrons are spread over a circular area with radius B (Eq. (2.20), Fig. 3.1). The electrons have an exponential distribution for the electron energy E :

$$\frac{dN}{dE} = \frac{N_e}{k_B T_e} \exp\left[-\frac{E}{k_B T_e}\right] \quad (3.1)$$

The hot electron number is given by $N_e = \eta E_L / (k_B T_e)$ with the energy conversion efficiency η of laser energy E_L into hot electrons. The mean electron energy $k_B T_e$ and number N_e appear as implicit quantities which can be determined experimentally. It is one of the most astonishing features of this simple model that the quantities connected to the electrons do not play a role in the final equations for the ions.

When the electrons cross the solid/vacuum boundary they induce a positive surface charge Qe on the conducting rear surface, leading to a surface charge density $Qe / (\pi B^2)$ located at $z = 0$, where z is the electron propagation axis. The potential of such a charge density in a cylindrically symmetric geometry where r denotes the radial coordinate can be calculated via

$$\Phi(r, z) = \frac{1}{4\pi\epsilon_0} \cdot \frac{Qe}{\pi B^2} \cdot \int_0^B \int_0^{2\pi} \frac{r' dr' d\phi'}{\sqrt{z^2 + r^2 + r'^2 - 2rr' \cos\phi'}} \cdot \quad (3.2)$$

At the z -axis ($r = 0$) this integral can be calculated and gives

$$-e\Phi(\xi) = E_\infty s(\xi) \quad (3.3)$$

with $\xi = z/B$ and $s(\xi) = 1 + \xi - (1 + \xi^2)^{1/2}$. Only few electrons with energies exceeding

$$E_\infty = Qe^2 / (2\pi\epsilon_0 B) \quad (3.4)$$

can escape the rear surface potential whereas the low energetic electrons reenter the foil. The point $\hat{\xi} = \hat{z}/B$ where electrons with the mean energy $k_B T_e$ turn around is defined by

$$E_\infty s(\hat{\xi}) \approx E_\infty \hat{\xi} = k_B T_e \quad (3.5)$$

for $\hat{\xi} \ll 1$. This approximation is valid for all experiments to be discussed. Using the definition for E_∞ and the electron density $n_{Q0} = Q/(\pi B^2 \hat{z})$ directly at the surface one derives

$$\hat{z} = (2\epsilon_0 k_B T_e / n_{Q0} e^2)^{1/2} \equiv \lambda_D \quad (3.6)$$

where λ_D is called the hot electron Debye-length. Note, that $n_{Q0} = 2n_{e0}$ (Eq. (2.22)) is composed from electrons with density n_{e0} streaming out of and back into the foil, thus, Eq. (3.6) is equal to the earlier definition of λ_D (Eq. (2.25)). It is readily seen from Eq. (3.5) that it holds

$$\frac{\lambda_D}{B} = \frac{k_B T_e}{E_\infty}. \quad (3.7)$$

The electron density distribution which is in equilibrium with the surface charge potential Φ is defined by

$$n_Q(\xi) = \frac{Q}{\pi B^3} \cdot \frac{dN}{dE} \cdot \frac{dE}{d\xi}. \quad (3.8)$$

The exponential energy distribution (Eq. (3.1)) and $E = -e\Phi$ delivers

$$n_Q(\xi) = n_{Q0} \exp[-s(\xi)/\xi_D] \left[1 - \xi / (1 + \xi^2)^{1/2} \right], \quad (3.9)$$

where $\xi_D = \lambda_D/B$. It holds

$$\pi B^3 \int_0^\infty n_Q(\xi) d\xi = Q. \quad (3.10)$$

Electrons propagate over distance λ_D and back before they reenter the foil leading to an obvious density enhancement expressed by $n_{Q0} = 2n_{e0}$. In the equilibrium situation $Q = 2N_e \lambda_D / L$ electrons are permanently outside the foil, which, in turn,

induce Q positive charges in order to maintain charge neutrality also on a scale of λ_D . This picture is true only for long enough pulses so one may write

$$Q = \begin{cases} 2N_e \frac{\lambda_D}{L}, & \text{for } \lambda_D < L \\ N_e, & \text{for } \lambda_D > L \end{cases}. \quad (3.11)$$

However, assuming the practically relevant case $\lambda_D < L$ and using Eqs. (3.7) and (2.21) one can write

$$Q = 2 \cdot \frac{B}{L} \cdot \frac{\eta E_L}{E_\infty} \quad (3.12)$$

and since E_∞ depends only on B and Q (Eq. (3.4)) it is readily seen that both the surface charge number Q and the electron escape energy E_∞ do not depend on the electron properties $k_B T_e$ and N_e .

From Eq. (3.3) together with $F = -d\Phi/dz$ one obtains

$$F(\xi) = \frac{k_B T_e}{e \lambda_D} \left[1 - \xi / (1 + \xi^2)^{1/2} \right] \quad (3.13)$$

for the electric field F in the vacuum region outside the foil. Directly at the surface ($\xi = 0$) the electric field agrees with the well-known result $F_0 = k_B T_e / (e \lambda_D)$ from PEM [15, 45] (Eq. (2.28)). Yet, in contrast to PEM the potential (Eq. (3.3)) stays finite for $\xi \rightarrow \infty$ in the model. Fig. 3.1 shows the shapes of the electron density distribution n_Q , the electric field F , and the potential Φ .

In a second step the potential Eq. (3.3) is used to calculate the energy $E_i(\xi)$ an ion with charge $q_i e$ gains between $\xi = 0$ and ξ

$$E_i(\xi) = -q_i e \Phi(\xi) = E_{i,\infty} s(\xi) \quad (3.14)$$

where $E_{i,\infty} = q_i E_\infty$ defines the energy an ion with charge $q_i e$ could theoretically gain by completely running down the potential well. Here only the most energetic ions are described which are emitted from the center of the emission zone where the field is highest. Ions starting from outer zones or from deeper surface layers ($z < 0$) will gain less energy and are not treated. The ion energy $E_i(\xi)$ of Eq. (3.14) results solely from the repulsion due to surface charges Qe , i.e., the influence of the hot electrons is neglected. This assumption is justified by the following simple picture based on the very different longitudinal spatial distributions of both charge contributions. The positive charge distribution (surface charges) is much more localized (within nm) than the electron cloud n_Q above the rear surface. The electron center of charge is approximately at a distance λ_D above the surface and its longitudinal width is of the same order (μm). Thus, the forces of the electrons on an ion at some distance from the surface compensate each other to some degree.

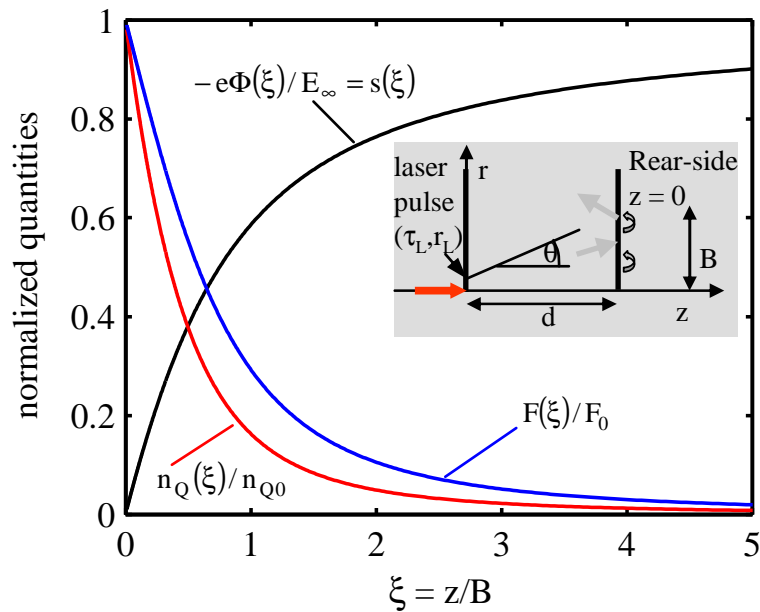


Figure 3.1: Explanation of quantities used in the text. The electrons are accelerated by the laser and then travel through the target with a certain spread. The self-induced field on the rear-side forces the electrons to turn around. The normalized quasi-static potential $-e\Phi/E_\infty$ (black), the electron density n_Q/n_{Q0} and the electric field F/F_0 are drawn as an example for $\xi_D = 1$.

The field appears the same as if the target would be Q -fold positively charged even though the electrons are not totally removed.

Using Eqs. (3.12) and (3.4) one can derive

$$E_{i,\infty} = q_i E_\infty = q_i 2mc^2 (\eta P_L / P_R)^{1/2} \quad (3.15)$$

where $P_R = mc^3/r_e = 8.71 \text{ GW}$ is the relativistic power unit. $E_{i,\infty}$ denotes the maximum possible energy an ion could gain for a certain laser power P_L providing an infinitely long acceleration. Note, that the maximum possible ion energy depends on the square root of the absorbed laser pulse power only [32] and that Eq. (3.15) shows no explicit dependence on the hot electron temperature T_e .

For future reference it is worth to consider the number of surface charges Q in more detail. Again it should be emphasized that Q electrons are permanently outside the foil so that the foil appears to carry a charge of $+Qe$. Using Eqs. (3.4) and (3.15) one finds

$$Q = \sqrt{\frac{4\epsilon_0}{e^2 c} \pi B^2 \eta P_L} \quad (3.16)$$

with no dependence on the special properties $k_B T_e$ and N_e of the laser accelerated electrons. For common values for the charge radius $B \approx 10 \mu\text{m}$, conversion

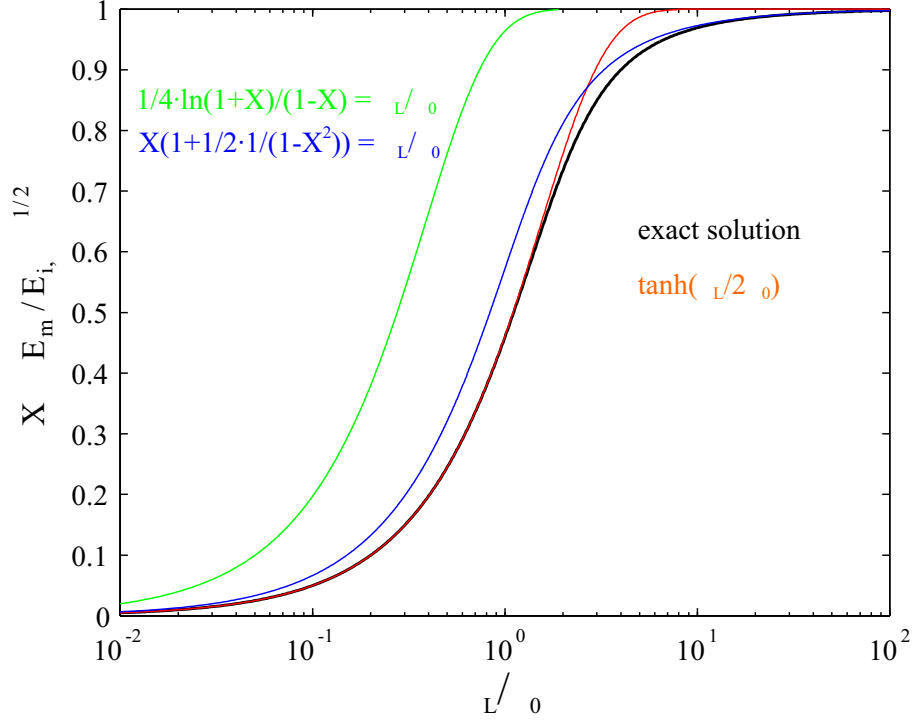


Figure 3.2: Curve sketching of Eq. (3.17). The second term of the right hand side of Eq. (3.17) (green) appears negligible. The exact solution (black) can be approximated by either the first term (blue) when $\tau_L/\tau_0 \rightarrow 1.3 \cdot \tau_L/\tau_0$ or the Taylor expansion of Eq. (3.17) to the third order with respect to $X = 0$ (red).

efficiency $\eta = 25\%$, and laser power $P_L \approx 100 \text{ TW}$ Q is of the order of 10^{11} .

For experimentally observable maximum ion energies E_m the time dependence of the accelerating process needs to be included, i.e., the acceleration stops after the electron pulse has passed. This is expressed by integrating the equation of motion $d\xi/dt = v(\xi)/B$ with $v(\xi) = (2E_i(\xi)/m_i)^{1/2}$ (Eq. (3.14)) and m_i as the ion mass one has

$$\frac{\tau_L}{\tau_0} = X \left(1 + \frac{1}{2} \frac{1}{1 - X^2} \right) + \frac{1}{4} \ln \frac{1 + X}{1 - X} \quad (3.17)$$

where $\tau_0 = B/v(\infty)$ with

$$v(\infty) = \sqrt{\frac{2 \cdot E_{i,\infty}}{m_i}} \quad (3.18)$$

and $X = (E_m/E_{i,\infty})^{1/2}$. This equation (3.17) is the main result of this analysis and will be discussed in the following. It should be mentioned that the quantities N_e and λ_D depend on the mean hot electron energy $k_B T_e$, but they do not appear in the final equation (3.17).

The black curve in Fig. 3.2 shows the solution of Eq. (3.17) which is not resolvable to obtain an explicit expression for the maximum ion energy E_m but the

taylor expansion of Eq. (3.17) around $X = 0$ when processed to the third order leads

$$X = \tanh \frac{\tau_L}{2\tau_0} \quad (3.19)$$

which is close to the exact solution (red curve, Fig. 3.2). It is also obvious that the second term on the right hand side of Eq. (3.17) (green) has minor importance compared to the first term (blue). However, it turns out that none of the approximations is able to account for the complete properties of the exact solution and are therefore not used in this work.

Chapter 4

Experimental Setup and Diagnostics

4.1 General setup and laser systems

All experiments were performed with high-intensity laser systems which are based on the chirped pulse amplification technique. Laser pulses from a conventional fs-oscillator are temporally stretched by 4-5 orders of magnitude to several ns duration. These stretched pulses are amplified from the nJ-level to several Joules in several stages and finally recompressed to the initial pulse duration in the fs range. The amplified short pulses are guided to the experimental chamber (Fig. 4.1) under vacuum to avoid nonlinear interactions with air. An off-axis parabolic mirror focusses the laser pulse on to the target in the center of target chamber obtaining spot sizes of several μm full width half maximum (FWHM) diameter. In this work laser irradiated thin foils, typically aluminum, gold, tungsten, or other metals, with thicknesses ranging from 1 – 100 μm were studied. The main concern was with the energy distributions of the ions emitted from the non-irradiated side of the foils. A Thomson parabola spectrometer looking in target normal direction at a distance of usually one meter served for this purpose and will be explained in more detail in Sec. 4.2.

During the amplification process, spectral modulations and amplified spontaneous emission (ASE) in the different stages lead to pre-pulses and a ns pedestal which one always needs to be aware of while performing an experiment. These pre-pulses usually have 7 orders of magnitude lower intensity ($\approx 10^{12} \text{ W/cm}^2$) which is enough to ionize the target before the arrival of the main laser pulse. Thus, a solid density foil could be evaporated, which drastically changes the experimental

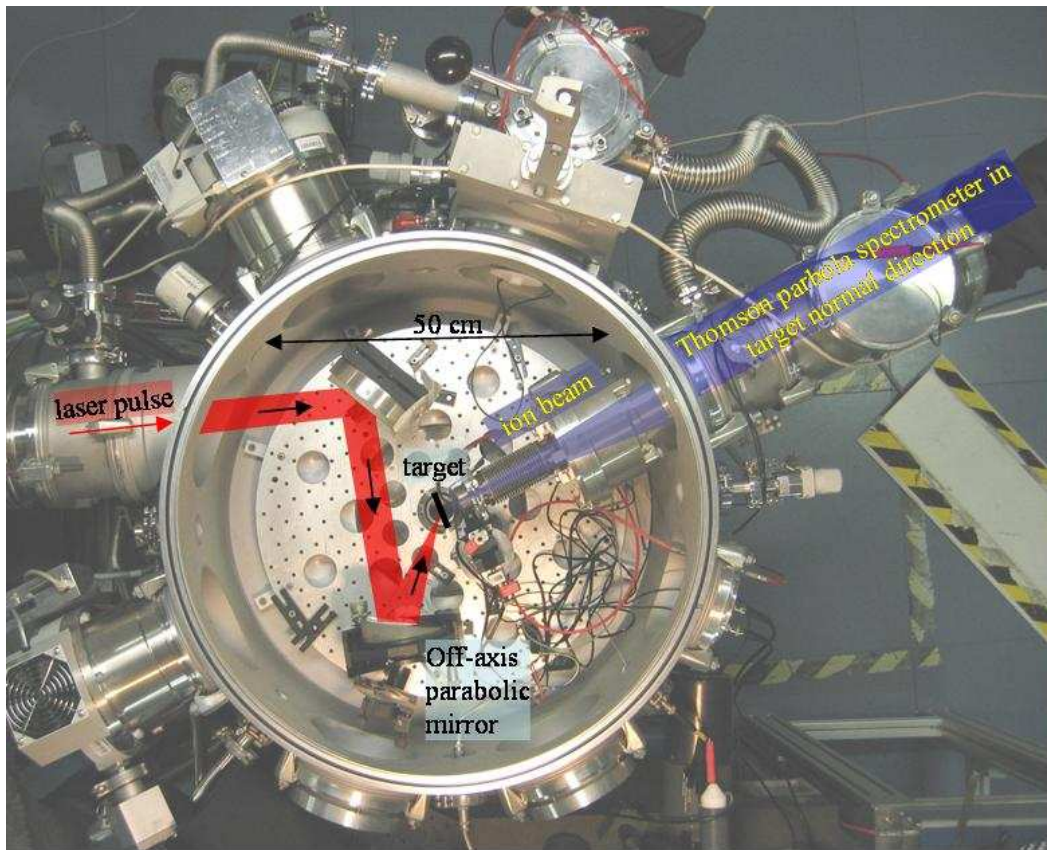


Figure 4.1: Typical setup in the experimental chamber (MBI, Berlin). The laser pulse (red) is guided through vacuum tubes into the chamber and focused with the off-axis parabolic mirror on to the target. The ion beam emitted mainly in target normal direction is detected with a Thomson parabola spectrometer with a single pinhole located at the chamber wall ($\approx 0.5 - 1.5$ m).

conditions.

The experiments were performed on a variety of different high-intensity CPA laser systems (Tab. 4.1). Their peak powers ranged from 5 to 30 TW corresponding to laser pulse energies from 1 to 20 J compressed into durations varying from 50 to 800 fs. The two comparably small laser systems (Max-Planck-Institute for Quantum Optics, Germany and Max-Born-Institute, Germany) had a repetition rate of 10 Hz, though this could not be committed because of the time consuming ion diagnostics. Nevertheless, a comprehensive study of the ion emission characteristics and the influence of different experimental parameters became accessible and will be discussed in sections 5.1 and 5.2. The remaining laser systems (LULI and LANL) were run in single shot mode which considerably constrained the number of shots (20 shots per week) and therefore the statistical accuracy. Due to their higher power (100 TW) experiments with heavy ions ($Z > 1$, Sec. 5.5) could

Location	MPQ Garching	MBI Berlin	LULI France	LANL USA
Medium	Ti:Sa	Ti:Sa	Nd:Glass	Nd:Glass
Wavelength λ_L [μm]	0.8	0.8	1.054	1.054
Rep. rate	10 Hz	10 Hz	1 shot/30 min	1 shot/30 min
Energy E_L [J]	0.7	0.7	10	16
Duration τ_L [fs]	150	50	350	800
Spot size r_L [μm]	2.9	4.7	3.8	8.0
Peak Power P_L [TW]	5.3	14	28	20
Peak intensity I_L $\left[\frac{\text{W}}{\text{cm}^2}\right]$	2×10^{19}	2×10^{19}	6×10^{19}	10^{19}
a_L	3	3	7	3

Table 4.1: Survey of laser-systems used for the experiments in the scope of this work. MPQ: Max-Planck-Institute for Quantum Optics, Garching, Germany; MBI: Max-Born-Institute, Berlin, Germany; LULI: Laboratoire pour l'Utilisation des Lasers Intenses, École Polytechnique-Univ. Paris VI, Palaiseau, France; LANL: Los Alamos National Laboratory, Los Alamos, USA.

be performed (Laboratoire pour l'Utilisation des Lasers Intenses, France). The demonstration of mono-energetic ion beams (Sec. 5.4) and a study of the longitudinal range of the accelerating field (Sec. 5.3) was done with the TRIDENT laser system at the Los Alamos National Laboratory, USA.

4.2 The Thomson parabola spectrometer

The ion energy distributions were measured with a Thomson parabola spectrometer invented by Joseph John Thomson in 1912. Although this diagnostic tool appears antic, it is the best solution for the experimental conditions in laser plasma experiments. It allows to determine the energy distributions of all participating particles in a single shot. The different ion species and charge states which are accelerated from the laser irradiated foil are deflected by a parallel electric and magnetic field onto parabolas giving the spectrometer its name. The curvature of the parabolic traces depend on the charge-to-mass ratios of the respective ions. The deflection along each parabola is a measure for the particle energy. The

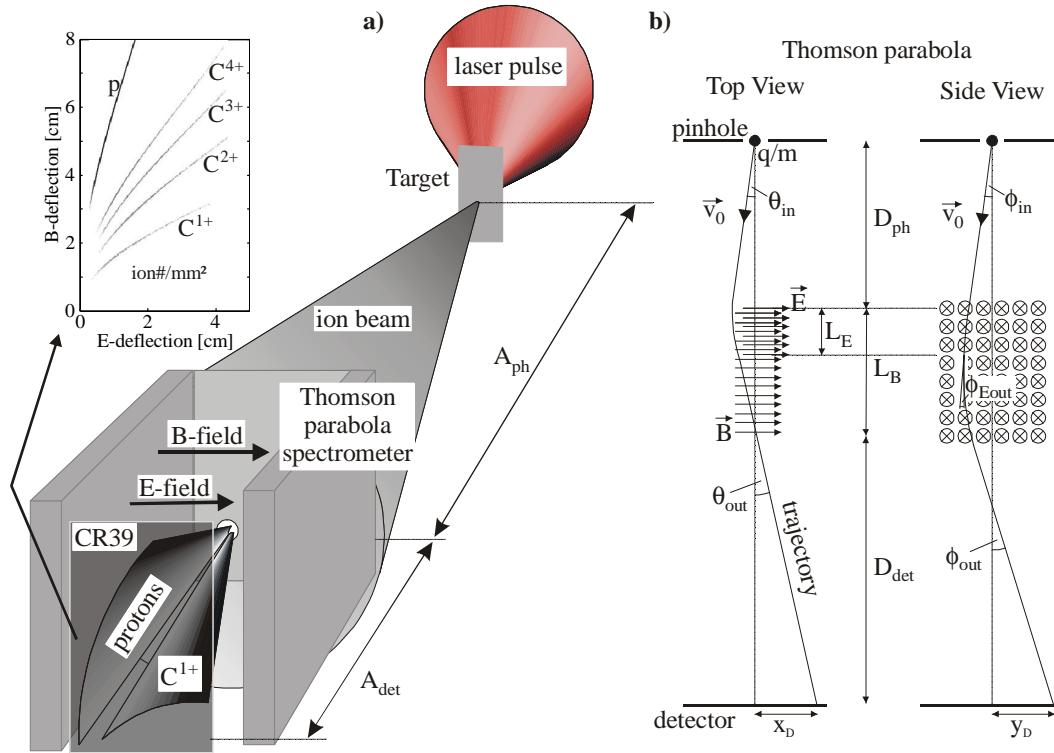


Figure 4.2: (a) Experimental setup with an example of the CR39-density image. The distances between target-pinhole and pinhole-detector are usually $A_{ph} \approx 1$ m and $A_{det} \approx 0.3$ m. (b) Sketch of the Thomson parabola spectrometer introducing the variables used in equations (4.1). Ions with charge-to-mass ratio q_i/m_i , e.g. 1 for protons, entering the pinhole ($\approx 300 \mu\text{m}$ diameter) with velocity $v_0 \approx 0.05c$, eventually under certain angles ϕ_{in} and θ_{in} which are usually zero. In the electric field $E_{TP} (\approx 1 \text{ MV/m})$ applied over a length of $L_E \approx 5$ cm the ions are deviated and exit under an angle $\theta_{out} (\approx 1.3^\circ)$. Due to the magnetic field $B_{TP} \approx 500 \text{ mT}$ the ions are deflected at $\phi_{Eout} \approx 10^\circ$ when they leave the shorter electric field and at $\phi_{out} \approx 20^\circ$ when they exit the magnetic field after $L_B = 10$ cm. Finally, after another ballistic propagation over $D_{det} \approx 3 - 20$ cm they hit the detector.

deflected ions are detected on a two dimensional screen (Fig.4.2). In usual experiments a single pinhole with a diameter of $100 - 300 \mu\text{m}$ is used at the entrance of the Thomson parabola spectrometer. Due to the large distance between target and pinhole ($A_{ph} \approx 1$ m) the solid angle of the spectrometer is of the order of 10^{-4} msr. Using a single pinhole at the spectrometer entrance has some important consequences. Neglecting the electromagnetic field, the setup would depict an ion pinhole camera. Therefore the chosen spectrometer setup combines both an energy and a spatially resolved measurement. For most experiments this effect is negligible, since the target size is small (≈ 2 mm wide) and the distance to the pinhole A_{ph} is much larger than the distance between pinhole and detector ($A_{det} \approx 30$ cm).

One exceptional experiment is discussed by Schreiber *et al.* [2].

To determine the observed ion species and charge states the equations of motion in the static electromagnetic fields need to be solved. The most general form is given by

$$\begin{aligned}
x_D &= D_{ph} \tan \theta_{in} + v_0 \sin \theta_{in} t_B + \frac{q_i e}{m_i} E_{TP} t_E t_B - \frac{q_i e}{2m_i} E_{TP} t_E^2 + D_{det} \tan \theta_{out} \\
y_D &= D_{ph} \tan \phi_{in} + R \cos \phi_{in} - \sqrt{R^2 - (L_B - R \sin \phi_{in})^2} + D_{det} \tan \phi_{out} \\
R &= \frac{m_i v_0 \cos \theta_{in}}{q_i e B_{TP}} \\
\tan \phi_{Eout} &= \frac{L_E - R \sin \phi_{in}}{\sqrt{R^2 - (L_E - R \sin \phi_{in})^2}} \\
\tan \phi_{out} &= \frac{L_B - R \sin \phi_{in}}{\sqrt{R^2 - (L_B - R \sin \phi_{in})^2}} \\
t_E &= \frac{R}{v_0 \cos \theta_{in}} (\phi_{Eout} - \phi_{in}) \\
t_B &= \frac{R}{v_0 \cos \theta_{in}} (\phi_{out} - \phi_{in}) \\
\tan \theta_{out} &= \frac{q_i e E_{TP} t_E}{m_i v_0 \cos \theta_{in} \cos \phi_{out}} + \frac{\tan \theta_{in}}{\cos \phi_{out}}
\end{aligned} \tag{4.1}$$

where the variables are explained in Fig. 4.2. In quite a few Thomson parabola spectrometer setups [36, 65] the length of the electric field L_E differs from the length of the magnetic field L_B . As a consequence the traces at the detector are not parabola like, which is often misattributed to the non-homogeneous magnet field. Assuming the standard setup, i.e., $L_E = L_B \equiv L$, $D \equiv D_{det} \gg L$ and $R \gg L$ with normal incidence of particles the well known parabola equation

$$x_D = \frac{m_i}{q_i e} \cdot \frac{E_{TP}}{L D B_{TP}^2} y_D^2 \tag{4.2}$$

is obtained.

However, in reality the electric and the magnetic field is inhomogeneous. Especially in the fringe regions additional field components appear and contribute to the particle deflection. Therefore, it is convenient to solve the equations of motion numerically in the realistic three-dimensional fields. The magnetic field geometry can be measured with a Hall probe or calculated numerically from the given geometry of the magnets (CST EMStudioTM [66]). The used spectrometer had a magnetic field of 500 mT over a length of $L_B = 10$ cm. Fig. 4.3a shows the good agreement of the measured and simulated main magnetic field component on the axis of the magnet which was used in the present experiments.

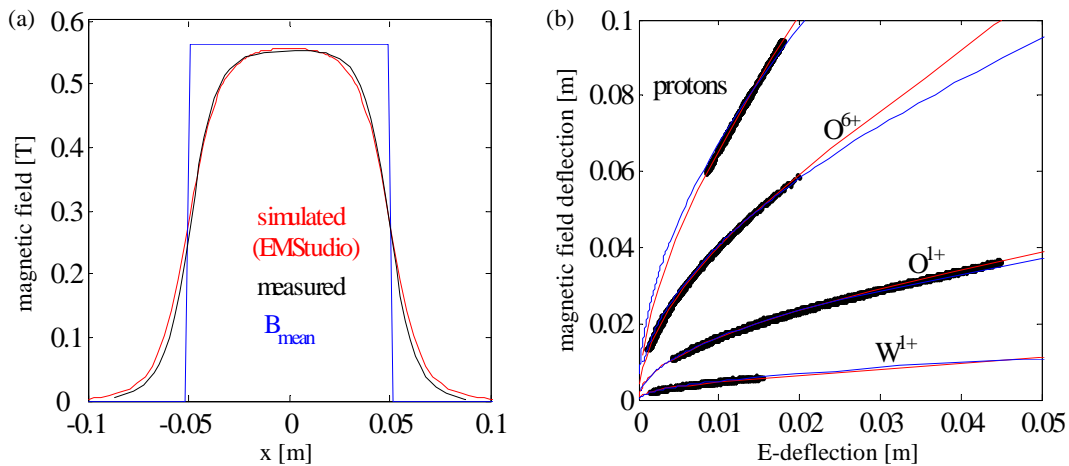


Figure 4.3: (a) Comparison between the measured (black) and simulated (red) (EMStudio) on-axis magnetic field of the Thomson parabola spectrometer magnet. The blue curve depicts the mean magnetic field B_{mean} obtained from $B_{TP} \cdot L_B = \int B_{\text{real}}(x) dx$. Similarly the electric field was approximated by $E_{TP} \cdot L_E = \int E_{\text{real}}(x) dx$. (b) Detector view with overlaid traces obtained from the analytic expression (eq. 4.1, blue) and the particle tracking (red) for the respective ion species. The black dots show experimental data.

The electric field was simulated, since the measurement is not straight forward at all. It was produced by 2 electrodes with a voltage of ± 15 kV placed 2 cm apart resulting in a field of 1.5 MV/m which is maintained over a length of $L_E = 5$ cm.

The measured traces can be reproduced well by the particle tracking (red) using the calculated three-dimensional field distributions, as shown in Fig. 4.3b for ions with a variety of charge-to-mass ratios and energies. The blue lines depict the traces obtained from Eq. (4.1) by using the constant mean magnetic (blue line in Fig. 4.3) and electric field and neglecting inhomogeneities and additional components. In fact, the particle tracking reproduces the shape of the measured traces better only for the low energetic protons which take a longer way through the magnetic field and are strongly deviated so that field inhomogeneities and additional field components become important.

4.3 The detector

The deflected ions are detected on a two-dimensional screen which is sensible in the keV/u- and MeV/u-energy range. Two solutions are widely used in laser-plasma experiments, i.e., micro channel plates (MCP) and plastic track detectors (CR39).

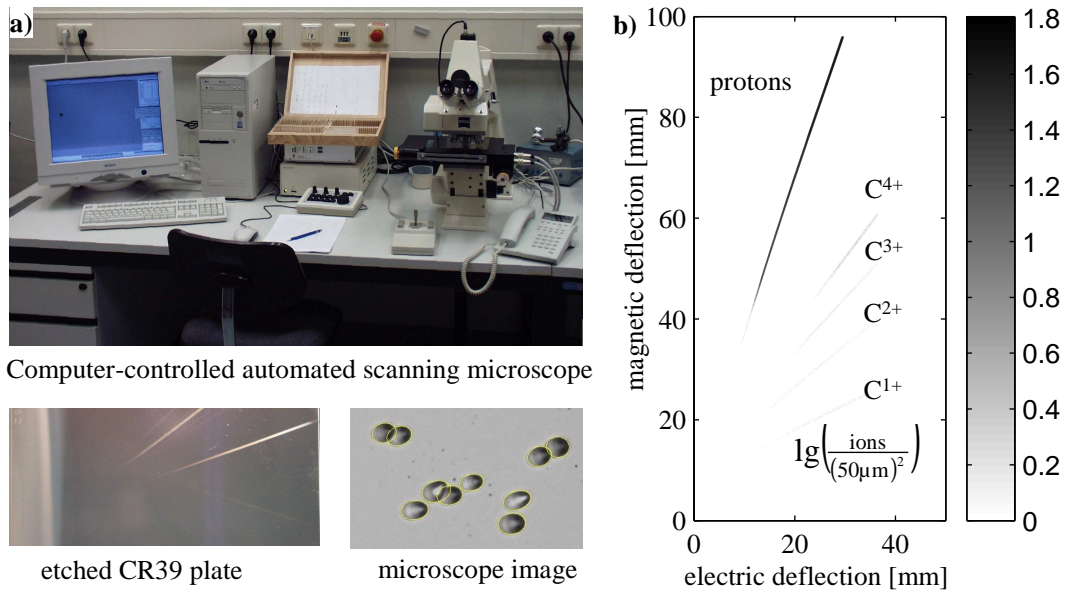


Figure 4.4: (a) The automated CR39-scanning system (SAMAICA) with computer and microscope. For more information see the PhD-thesis of Hegelich [36]. (b) Ion-intensity-image of a counted CR39-plate.

An MCP is a two-dimensional electron multiplier. In the first plate ions expel electrons which are accelerated on to the second plate where they in turn produce an electron avalanche. These secondary electrons are accelerated and hit a phosphor screen. The scintillating light is imaged on a coupled charge device (CCD) camera. Single ion events are measurable and the maximum signal is limited by the saturation of one micro-channel (≈ 10 ions per $50 \times 50 \mu\text{m}^2$). However, the ion spectra can be obtained online, although the electronics of the detection system usually requires some effort in shielding because of the strong electromagnetic pulse due to the laser impact.

Plastic track detectors, e.g. CR39, do not underlay such problems, but the evaluation is time consuming (approximately 4 hours per shot). After the irradiation the plates need to be etched in 6-molar sodium leach. This process expands the small destruction in the polymer matrix caused by the energy deposition of the ion to visible craters of several micrometer size. Each crater corresponds to a single ion hit allowing single ion detection. The size of the craters does depend on the ion species, its energy and the etching temperature and duration. The craters on the etched CR39-plates need to be counted which is a time consuming procedure even with the automated system consisting of a computer-controlled microscope with a movable stage and a CCD-camera (SAMAICA, Fig. 4.4a). With this device the CR39-plates are scanned and on each position a pattern recognition software analyzes the picture and counts the craters. After the whole procedure one can

obtain an image of the CR39 (Fig. 4.4b). Although the resolution of this image is of the order of a few μm , a pixel-size of $50 \times 50 \mu\text{m}^2$ was chosen. The maximum value in this picture is ≈ 100 , exceeding the MCP maximum by approximately one order of magnitude. By choosing proper etching conditions, i.e., etching for shorter times, this number can be easily increased by 2 orders of magnitude.

In this work mainly CR39-plastic track detectors were used in the Thomson parabola spectrometer. Most of the presented experiments were done on high power laser facilities, where one can expect only 20 shots per beam time (1 week) or less, so the post-processing time was still acceptable. The setup during the experiment was very simple and insensitive to disturbances. The ability of CR39 to detect a large number of ions in a single shot was an additional basic necessity, because it is unthinkable to improve statistics by doing multiple identical shots.

4.4 Typical spectrum

Once the observed ion species and charge states have been identified, their corresponding energy distributions can be calculated. This is done by dividing the respective trace into spatial bins and counting the particles therein. From the single pinhole setup (Fig.4.2) it is obvious that the bin-size should be larger than $b_{min} = d_{ph}(1+V)$, where d_{ph} is the pinhole diameter, and $V = A_{det}/A_{ph}$ (Fig. 4.2a) is the magnification of the ion pinhole camera and usually of the order of 0.3. Since the deflection along a certain parabola depends nonlinearly on the energy (Eq. (4.1)) the constant spatial bin-size b_{min} leads to an energy dependent energy resolution, i.e., the resolution in the low energy part of the spectrum is better (Fig. 4.5). This also leads to an energy dependent lower detection threshold (dotted lines Fig. 4.5). The spectral distributions were observed from a laser irradiated contaminated aluminum foil at the MPQ, Garching. The hydrocarbon contaminants reflect in the observation of protons and carbon ions up to the fourth charge state, where the protons are most prominent and accelerated to the highest velocities (0.1c). The spectral distributions show a clear cutoff at the respective maximum ion energy E_m (see also Fig. 4.3) well above the detection threshold. These cutoff energies are of major importance for this work and will be used to compare with the theories.

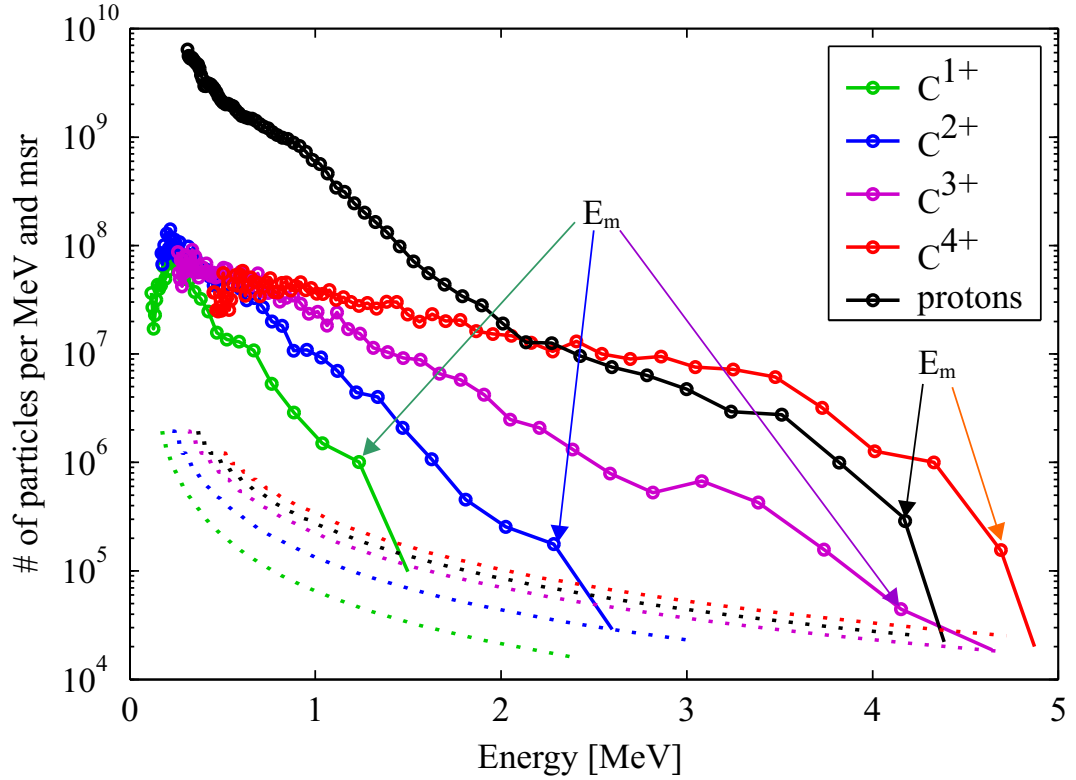


Figure 4.5: Typical energy distribution of ions observed from hydrocarbon contaminated aluminum foils irradiated by a high-intensity laser pulse with an intensity of $\approx 2 \times 10^{19} \text{ W/cm}^2$ containing 0.7 J in a spot of $5 \mu\text{m}$ FWHM diameter and 150 fs duration (MPQ). The circles depict the points at which the energies are defined depicting the higher resolution in the low energy part of the spectrum. The dotted lines show the lower detection threshold resulting from a single ion hit in the respective energy interval. The spectra show a cutoff at a the maximum energy value E_m .

Chapter 5

Experiments

5.1 Variation of experimental parameters

In this section the dependence of the maximum proton energy on different experimental parameter is explored and compared with the analytical theory (chapter 3) and PEM (Sec. 2.3.3). The experiments were performed at the MPQ and the MBI laser systems delivering laser pulses with energies of $E_L < 1$ J and pulse durations τ_L of 150 and 50 fs, respectively. In the focal spot of 5 and 8 μm full width at half maximum (FWHM) diameter the intensity reached approximately 2×10^{19} W/cm². The targets were common aluminum foils with thicknesses of 5 and 13 μm contaminated with the usual amount of hydrocarbon caused by the poor vacuum conditions ($\approx 10^{-6} - 10^{-4}$ mbar). The maximum proton energies were measured as a function of laser energy E_L , focal spot size r_L , and target thickness d (MPQ) and pulse duration τ_L (MBI). Only one of those parameter was varied while the others were kept constant.

Fig. 5.1 shows the maximum proton energy E_m as a function of laser energy E_L . The dependence is reproduced quite well by the analytical model (solid line, Eq. (3.17)) and PEM (dashed line, Eq. (2.32)). At higher laser energies the measured ion energies seem to saturate, which could be due to the shock wave launched by the laser pre-pulse (ASE) which causes a destruction of the rear surface at higher laser energies.

In a second experiment the radius of the laser focal spot was varied by moving the focussing off-axis parabolic mirror along the laser propagation direction in steps of 50 μm . This not only changes the focal spot size but also the intensity distribution which was imaged on to a CCD camera (Fig. 5.2a). The FWHM

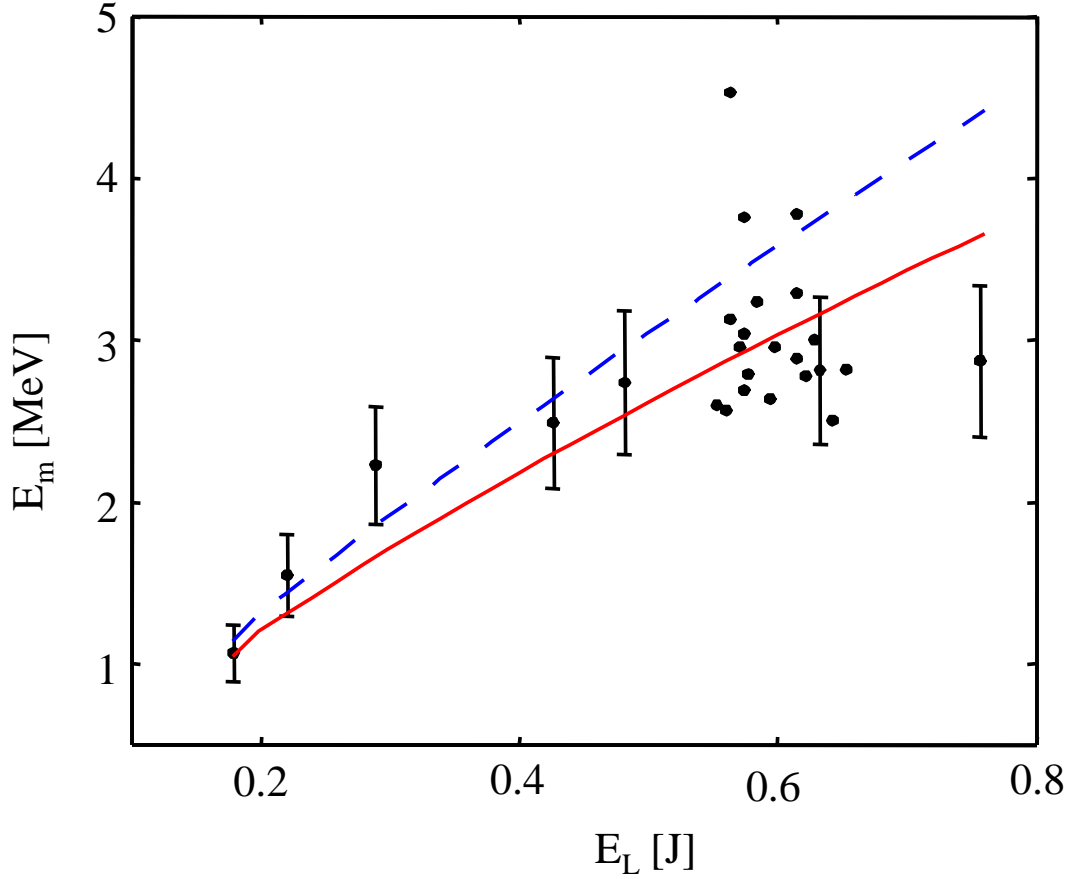


Figure 5.1: Dependence of the maximum proton energy on the energy of the laser pulse ($\tau_L = 150$ fs, $r_L = 3 \mu\text{m}$, $d = 5 \mu\text{m}$). The result of the analytical model (solid line, Eq. (3.17)) and PEM assuming $n_{i0} = 0.3 - 1.2 \cdot 10^{21}/\text{cm}^3$ (dashed, Eq. (2.32)) are compared to the data.

diameter ($2r_L$) of the distributions were determined by counting the area of the pixels with values higher than half of the appearing maximum and assuming this total area to form a circle. The assigned values d_{FWHM} and the corresponding mean intensities (blue and green curve in Fig. 5.2b) were used for the theoretical predictions of Eq. (3.17) (solid line) and PEM (dashed) and are compared to the experimental data in Fig. 5.2.

Fig. 5.3 shows the experimentally observed values for the maximum proton energy as a function of the laser pulse duration again keeping $d = 13 \mu\text{m}$, $r_L = 4 \mu\text{m}$ and $E_L = 0.7$ J constant. Both the experimental data and the models (analytic model, solid and PEM, dashed) show an optimal maximum proton energy of ≈ 3 MeV at an optimal pulse duration of around 250 fs. This observation will be discussed in more detail in section 6.1.2. The maximum in the data points is more pronounced than both theories predict eventually showing deficiencies in the

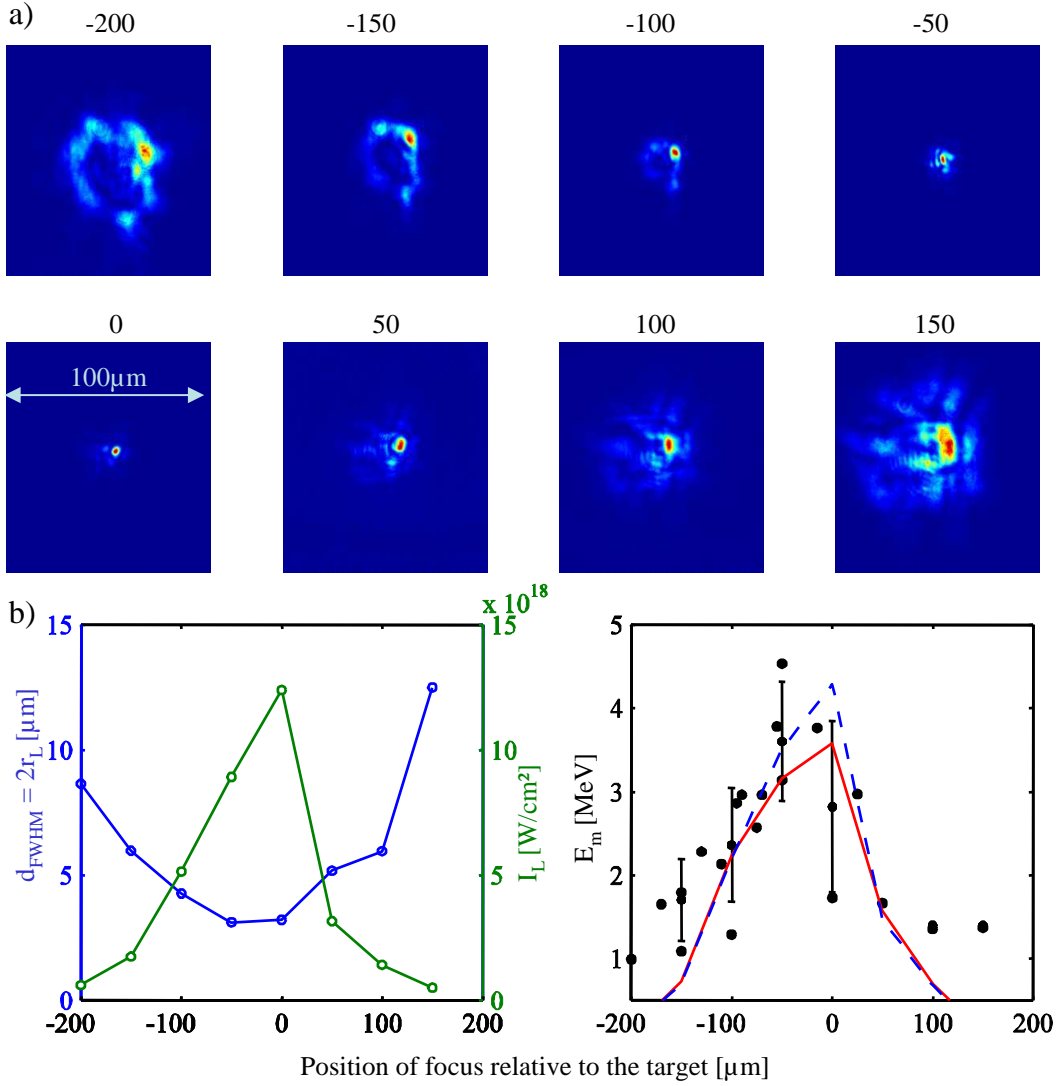


Figure 5.2: (a) Focal intensity distributions for the focal scan. The numbers give the position of the focus relative to the target in μm . Although the distributions are inhomogeneous far from the focus it is possible to assign a mean intensity I_L and FWHM diameter d_{FWHM} (b). Negative values mean the laser focus is placed in front of the target and defocuses again. (c) Dependence of the maximum proton energy on the position of the laser focal spot relative to the target position compared to the analytic theory (solid) and PEM ($n_{i0} = 0.4 - 1.2 \cdot 10^{21}/\text{cm}^3$ (dashed)). The aluminum target thickness ($d = 5 \mu\text{m}$), the laser pulse duration ($\tau_L = 150 \text{fs}$) and energy $E_L = 0.8 \text{J}$ were kept constant.

models.

The experiment with varying target thickness was part of a study performed in the very beginning of this thesis in cooperation with Malte Kaluza at the Max-Planck-Institute for Quantum Optics, Garching [67]. The influence of the amplified

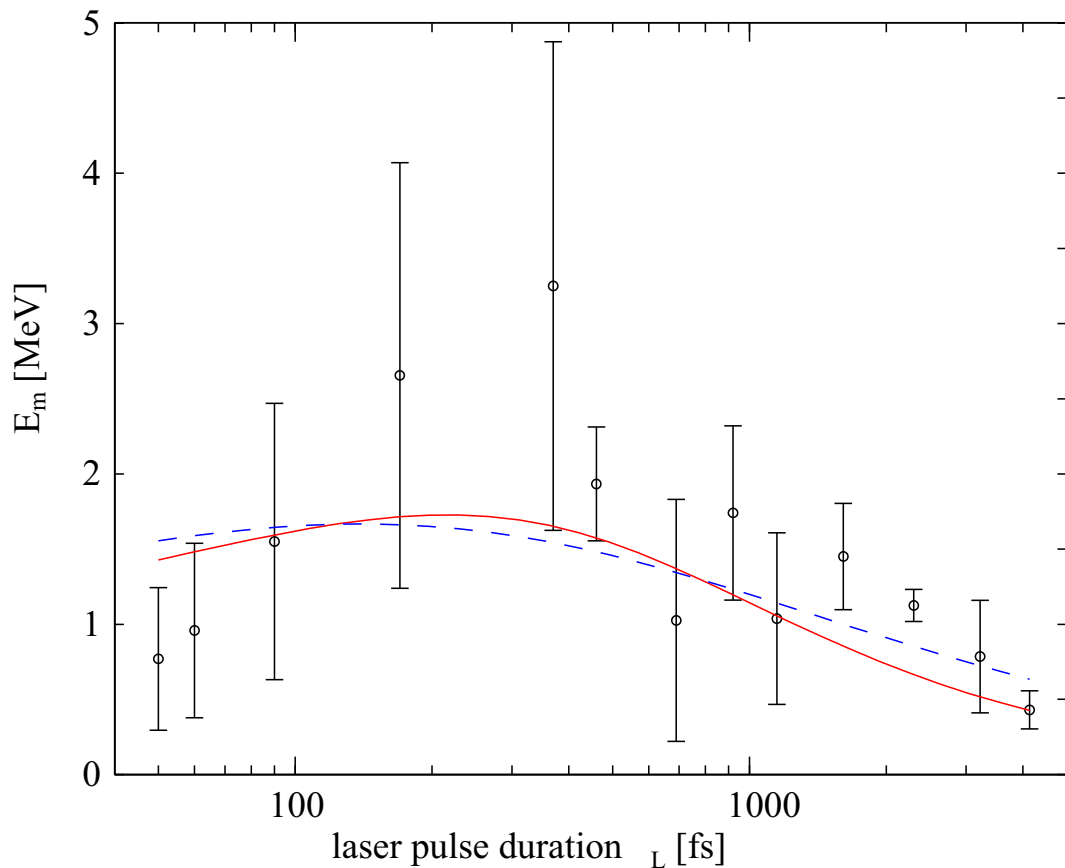


Figure 5.3: Dependence of maximum proton energy on laser pulse duration for constant laser energy ($E_L = 0.7$ J) and laser focal spot size ($r_L = 4 \mu\text{m}$). The experimental data are compared with the analytical model (solid) and PEM with $n_{i0} = 0.02 - 1.46 \cdot 10^{21} / \text{cm}^3$ (dashed). The data show a more pronounced maximum than predicted by both theories.

spontaneous emission (ASE) pedestal, which is present in all CPA laser systems, on the acceleration of ions accelerated from the rear side of laser irradiated thin foils was explored (For detailed information see, for example, refs. [11, 67]). The laser pulse had an energy of ≈ 0.6 J within 150 fs FWHM-duration and was focussed to a spot of $4 \mu\text{m}$ FWHM-diameter. The ASE intensity ($4 \times 10^{12} \text{W}/\text{cm}^2$) and duration (0.5 ns) was kept constant. Fig. 5.4 compares the observed maximum proton energies with the predictions of the analytical theory (solid curve) and PEM (dashed curve). For thin targets ($< 5 \mu\text{m}$) the maximum proton energy drops unlike as predicted by the theory. This is a consequence of the shock wave launched by the ASE pre-pulse which destroys the target rear side before the arrival of the main laser pulse thus suppressing the ion acceleration process as discussed by Kaluza *et al.* [11, 67].

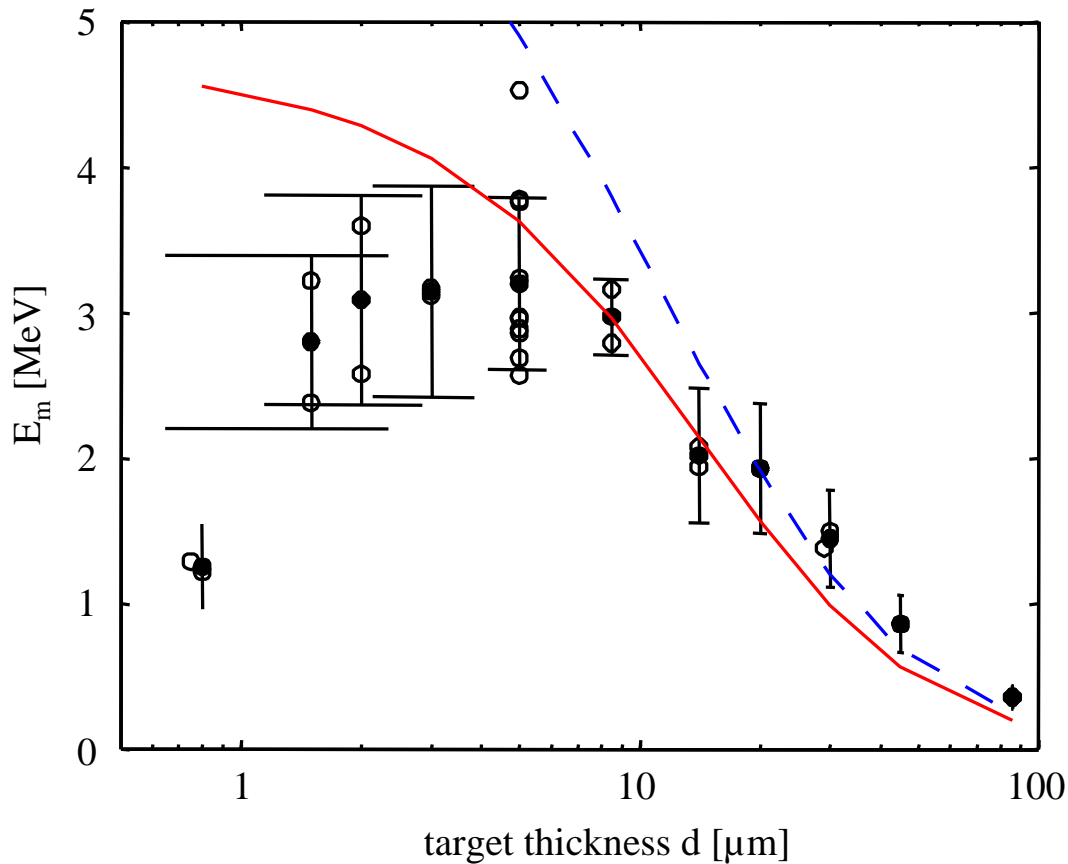


Figure 5.4: Dependence of maximum proton energy on aluminum target thickness. The laser energy (0.6 J), focal spot diameter ($4\ \mu\text{m}$) and pulse duration (150 fs) were kept constant. The intensity of the ASE pedestal was on a level of 2×10^{-7} with respect to the intensity of the main pulse ($I_L = 2 \times 10^{19}\text{W}/\text{cm}^2$) and it was set to a duration of 0.5 ns. The data are compared with the analytic theory (solid) and PEM with $n_{i0} = 0.05 - 1.18 \cdot 10^{21}/\text{cm}^3$ (dashed).

5.2 Source-size measurements

Up to now only the maximum proton energy was discussed. The ions which gain the maximum energy originate from the center of the emission zone while the source gets larger for the lower energetic protons. The acceleration field spreads transversely over large distances as confirmed by recent measurements of the source sizes of protons [26, 27, 28]. Usually for these measurements, the rear surface was grid-structured on a μm -scale. Radiochromic film-stacks were used to measure both the proton energy distribution and their beam profile. The grid structure was visible in the different RCF-layers of the stack which gives rise to a very low emittance of only $0.01\ \text{mm}\cdot\text{msr}$ [26, 27]. Furthermore, by simply counting the number of grid lines visible in the RCF-layers, the source-sizes could be estimated

for different proton energies. The estimation of the source-sizes of the heavier ions such as carbon and oxygen which are usually co-accelerated with the protons from the hydrocarbon and water contaminants on the target surfaces is rather complicated. The heavy ion numbers are a factor of 100 smaller than the proton numbers so that their signal in the RCF-layers is negligible. The only way to determine the source-sizes of heavy ions using the RCF-stack method is to heat the target to get rid of the contaminating proton layers [3]. Still the energies of the heavy ions are too small to penetrate more than the first two RCF-layers, giving a rather insufficient energy resolution. These considerations clearly motivate the performed scraper measurement which additionally allows a rough transversal field characterization.

The source-size measurements were performed at the ATLAS10 10-Hz-tabletop-laser-system at the MPQ Garching providing laser pulses with energies of about 0.8 J and 150 fs FWHM duration at a center wavelength of 790 nm. Single laser pulses were focused onto 5 μm thick aluminum foils with an incident angle of 30° reaching an intensity of $2 \times 10^{19} \text{ W/cm}^2$ in a spot of 5 μm FWHM diameter. The ion spectra were recorded in the target normal direction ($\pm 5 \text{ mrad}$) using the Thomson parabola spectrometer with a pinhole of 300 μm diameter placed 80 cm behind the target while the distance pinhole-detector (CR39) was 30 cm. The standard experimental setup was extended by the introduction of a scraper placed 8 mm behind the target to perform the knife-edge measurements by moving the scraper across the beam. A stainless steel razor-blade served for this purpose. Since the solid angle of the ion beam ($\sim 25 \text{ msr}$, see, for example, ref. [67]) was about 5 orders of magnitude larger than the detector solid angle (10^{-4} msr), only a small fraction of the signal passing the scraper was detected.

Fig. 5.5 shows the spectra of protons and carbon ions with charge states 1+ to 4+ for six selected scraper positions, namely with the scraper at the center of the ion beam (a) and successively moved inwards in 40 μm -steps (b-f). For the next scraper position, following (f) corresponding to 240 μm off center, no ions are detected. The high-energy protons ($E_{\text{kin}} > 0.8 \text{ MeV}$) and highly charged carbon ions (C^{4+} , $E_{\text{kin}} > 2.5 \text{ MeV}$) already vanish after the first scraper step (40 μm) whereas the low-energy protons ($< 0.8 \text{ MeV}$) and the lower carbon charge states appear to be unaffected. The maximum kinetic energy both of protons and C^{4+} -ions decreases with the scraper sliding into the ion beam. Only protons and singly-charged carbon ions remain at the last scraper position (Fig. 5.5f).

In order to rule out influences of the scraper itself the deflection of the ions with the lowest energies was calculated assuming that the scraper is charged with

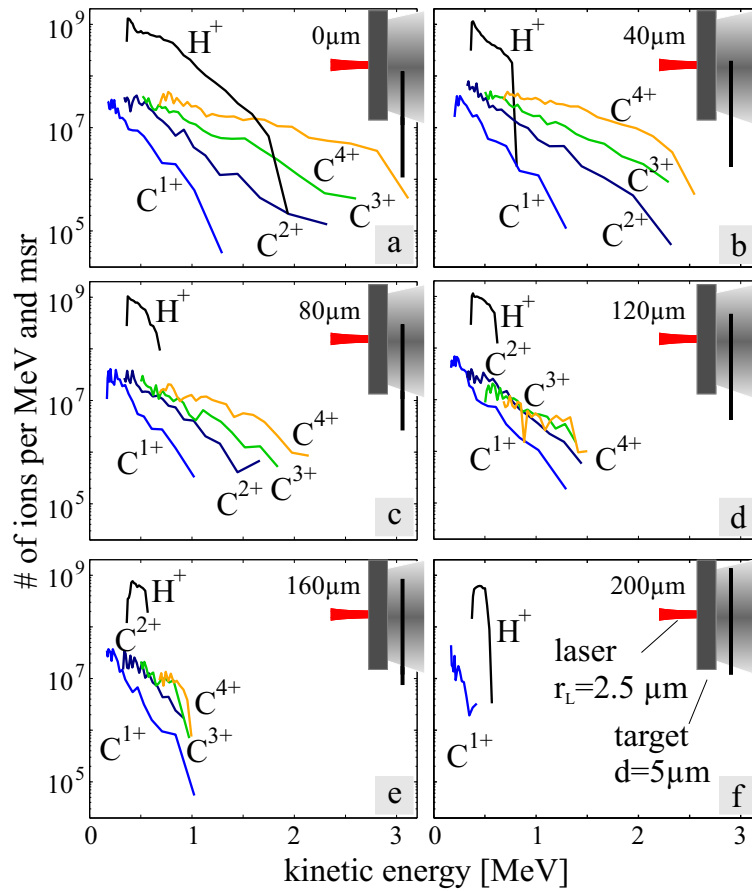


Figure 5.5: Proton and carbon spectra for different scraper positions, starting from the center (a). The aluminum target was $5\ \mu\text{m}$ thick and the laser was focussed to a FWHM diameter of $5\ \mu\text{m}$. The scraper was moved in $40\ \mu\text{m}$ -steps into the ion beam.

1 nC. This is a reasonable value for the charge carried by the fast electrons leaving the target. The deflection in the plane of the Thomson parabola spectrometer pinhole was $40\ \mu\text{m}$ and $100\ \mu\text{m}$ for protons and C^{4+} -ions, respectively. Since the pinhole diameter was $300\ \mu\text{m}$ the influence of the scraper on the passing ions was negligible.

The measurements provide information of the energy dependent source sizes of not only the protons but also the accelerated carbon ions. This allows the approximation of the electric fields which were present during the acceleration process and will be discussed in Sec. 6.2.

5.3 Ion acceleration from buried layers

While the previous sections dealt with maximum proton energies and the transversal characteristics of the electric field and the ion sources the aim of this experiment was to characterize the acceleration field longitudinally, i.e., its extension into the solid target. The measurement described in this section provides information about the depth from where ions can be accelerated and thus contribute to the observed spectrum.

The experiments were performed at the TRIDENT laser facility at the Los Alamos National Laboratory, Los Alamos, USA, delivering 16 J pulse energy in a duration of 800 fs reaching an intensity of $\approx 10^{19}$ W/cm² in the focal spot. Up to now the experiments addressed on the acceleration of ions from the target rear surfaces. Here an experiment is presented where the laser pulse was focussed onto 25 μ m thick platinum foils with thin titanium nitride layers (~ 3 nm) buried in different depths (3–200 nm) measured from the rear side. The nitrogen ions should serve as test ions to probe the electric field inside the target having the advantage that, unlike protons, carbon or oxygen ions from water and oil contaminants, nitrogen is not observed in usual experiments. The targets were produced by sputtering titanium onto the platinum foils in a nitrogen atmosphere which should be sufficient to build the TiN compound. After that another layer of platinum was sputtered on top for different time spans achieving a variety of cover layer thicknesses.

Fig. 5.6a shows the depth distribution of nitrogen determined by the Elastic Recoil Detection Analysis (ERDA) [68, 69, 70] at the tandem accelerator in Garching, Germany. In this method gold ions with energies of several MeV/u are shot on the target rear side under a small angle. In the material they loose energy and slow down. Target ions are Rutherford-scattered and observed under a certain angle with a detector which is able to measure both incident energy and energy loss. This allows the identification of the particles and their original depth in the target.

Obviously carbon atoms were included into the buried layer during the sputtering process (Fig. 5.6a). The surface contaminants were removed by heating the targets to $\approx 800^\circ$ K for several minutes which had no influence on the distributions of the different elements inside the target as proofed by ERDA measurements. Still the number of carbon atoms near the surface was enhanced (red curve in Fig. 5.6b).

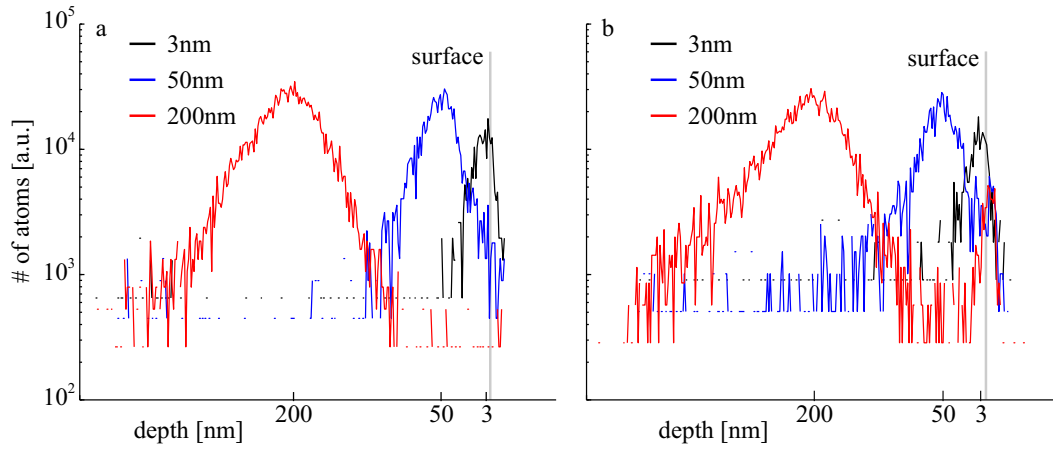


Figure 5.6: Depth-Distributions of nitrogen (a) and carbon (b) in three different platinum foils which were used in the experiments. The ions were buried in three different depth, i.e., 3 nm (black), 50 nm (blue), and 200 nm (red). Clearly, nitrogen is contained only in the buried layers. Carbon atoms contaminate the buried layers and appear also on the target surface even when heated to moderate temperatures (800°K).

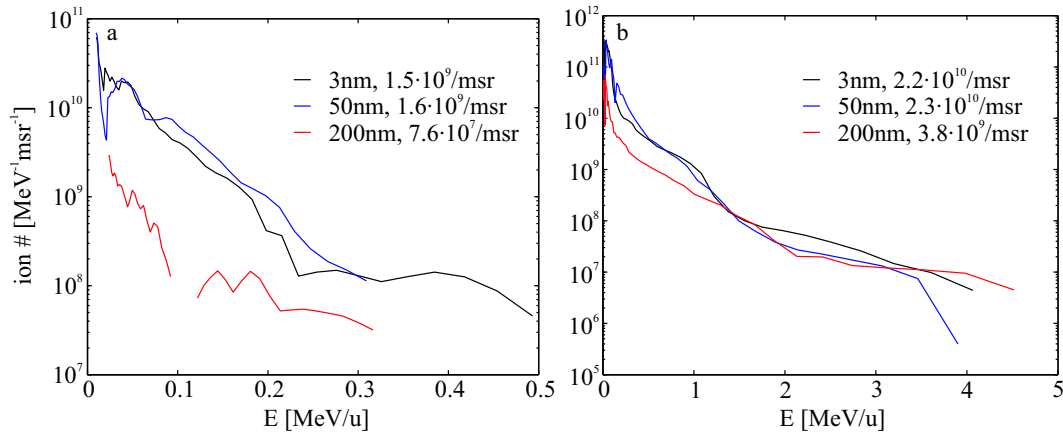


Figure 5.7: Energy distributions of nitrogen (a) and carbon ions (b) for layer depths 3 nm (black), 50 nm (blue), and 200 nm (red). No differentiation into different charge states was made for simplicity. The numbers in the legend give a relative ion number per msr obtained from integral over the ion spectrum $\int_0^\infty dN_i/(dE_i d\Omega) dE_i$.

Fig. 5.7 shows the energy distributions of nitrogen (a) and carbon ions (b) as they were observed from the laser irradiated foils. Here only the total energy distributions are shown without differentiation into charge states. The shape of the energy distributions hardly changes with the depth of the layer. The nitrogen almost vanishes for the case of the deepest layer (red curve, fig. 5.7a), i.e. 200 nm, where the number of ions per msr (integral over the ion spectrum, $\int_0^\infty dN_i/(dE_i d\Omega) dE_i$) is reduced by factor of 20. Also the number of carbon ions is six times lower for this case (red curve, fig. 5.7b).

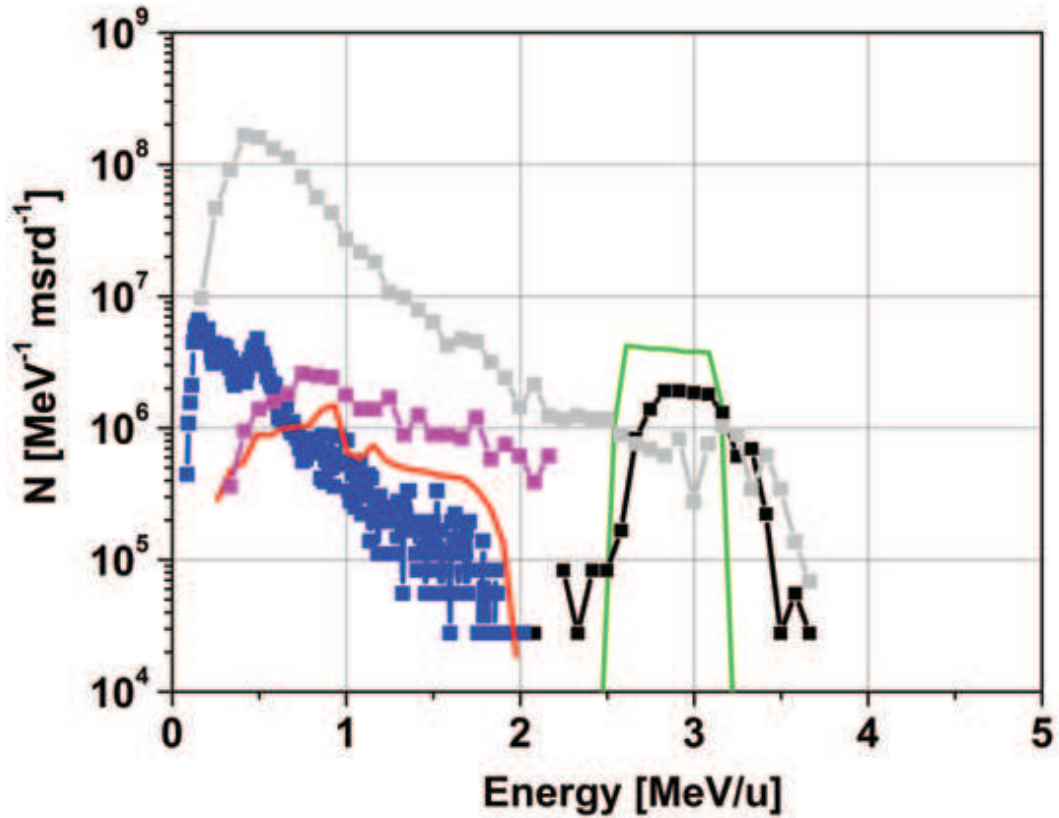


Figure 5.8: Ion spectra measured from 20 μm Pd-foils. The plot shows the mono-energetic C^{5+} -ion energy distribution (black), the dominant substrate charge state Pd^{22+} (blue) and the corresponding results from the 1D-BILBO-simulation (green and red, respectively). The magenta curve shows a typical C^{5+} -spectrum obtained from an unheated Pd-foil, and the grey curve represents a C^{4+} -spectrum from a heated tungsten target. In the last two cases the carbon contaminant layer is thick and does not form a monolayer source, resulting in continuous energy distributions.

5.4 Mono-energetic ion beams

In the previous experiments wide exponential energy distribution were observed. This can be qualitatively understood by the fact that the acceleration field drops transversely over several 100 μm (section 5.2), thus ions starting at different transverse positions experience different ionization and acceleration field strengths. Moreover, if the source sheath of ions is thicker than some monolayers, the most energetic ions starting from the topmost layer can modify the field for the proximate ones. In this section an experiment is discussed, where the source volume of the ions is reduced in a way that quasi mono-energetic ion beams were observed [4].

The experiments were performed at the TRIDENT laser facility, Los Alamos

National Laboratory, USA. The targets (20 μm thick Palladium foils) were heated in order to remove the hydrogen contaminants, which is achieved for temperatures above 600 K. The carbon from the various hydrocarbon contaminants remains on the surfaces. The special catalytic surface chemistry of palladium causes these carbons to form thin graphite layer (only some monolayers) when heated to temperatures above 1100 K. Further increasing the temperature above 1300 K would lead to a complete removal of the carbon layers. The measured ion spectra are shown in Fig. 5.8. The black curve shows the mono-energetic energy distribution of C^{5+} -ions measured from a Pd-foil heated to approximately 1100 K. The ratio $\Delta E/E$ is $\sim 17\%$, where ΔE is the width of the distribution and E its mean energy. The corresponding highest substrate charge state Pd^{22+} (blue) is accelerated after all of the C^{5+} -ions have detached and were accelerated. Both spectra are well reproduced by 1D-numerical simulations (green for carbon, red for palladium). The magenta and the grey curves show energy distributions of C^{5+} -ions from cold Pd-foils and C^{4+} -ions from heated W-foils. In both cases the carbon layer is comparably thick and not monolayer-like, leading to a continuous energy spectrum. A detailed discussion is found in Sec. 6.4.

5.5 Acceleration of heavy ions ($Z > 1$)

As indicated in the previous sections the accelerated ions appear with certain energy and charge state distributions which, in general, cover a broad energy range. In this section the ion acceleration is explored under the aspect of different elements and their corresponding charge state distribution.

The experiments were performed at the Laboratoire pour l'Utilisation des Lasers Intenses (LULI) at École Polytechnique. It delivered pulses with an energy of 8 – 10 J and a FWHM duration of 320 fs in a focal spot of 8 μm FWHM diameter reaching an intensity of $\approx 6 \times 10^{19} \text{W}/\text{cm}^2$. The targets were resistively heated to remove the contaminating hydrogen. Different ion species could be observed by varying the target material, i.e., tungsten foils with layers of lithium, beryllium, carbon, oxygen and argon as well as vanadium and zirconium foils. Nevertheless, the remaining oxide- and carbide-layers on the targets could not be removed by heating. Since oxygen and carbon is usually ionized up to the helium like charge state (O^{6+} and C^{4+}) these ions provided the highest charge-to-mass-ratio and were preferentially accelerated. Figure 5.9 shows typical energy distributions obtained from the rear side of a laser irradiated 25 μm -thick tungsten foil with a layer composed from beryllium, oxygen and argon, which was heated to a temperature

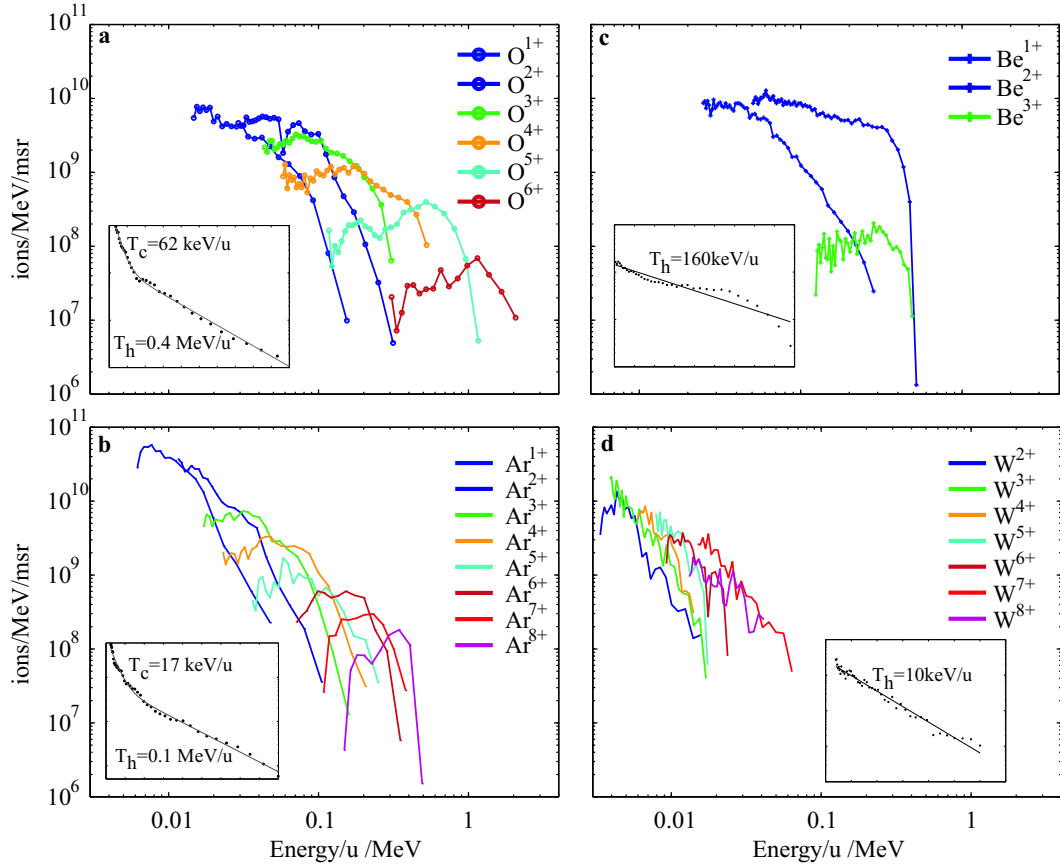


Figure 5.9: Typical ion spectra from heated W-foils irradiated at LULI-laser conditions. The lighter elements oxygen, argon and beryllium are contained in the surface layers and show the energy distribution depicted in a, b and c, respectively. Ions from the tungsten foil itself reach only very low energies (d) because of the small charge-to-mass ratio. For each ion species, higher charge states are shifted towards higher energies. The total ion energy distributions show a single- or double-exponential energy distribution (insets) with a larger mean energy T_h for larger charge-to-mass ratios.

of 1300 K. The total energy distribution of each element, obtained by summing up the charge state spectra, can be described by a single- or a double exponential function as shown in the insets of Fig. 5.9. The mean ion energy T_h gets larger for higher charge-to-mass ratios, i.e., for oxygen $T_h = 400\text{keV/u}$ and $T_h = 10\text{keV/u}$ for tungsten. When considering each ion species separately, higher charge-states are shifted towards higher energies. However, the explicit shape of the single charge state spectra especially for the case of oxygen (fig. 5.9a) and argon (fig. 5.9b) show distinct maxima. This phenomenon will be considered in more detail in section 6.5.

Chapter 6

Discussion

6.1 Potential of the analytical model

6.1.1 Comparison with published results

The good agreement between the analytical model described in chapter 3 could be shown in the experiments where several experimental parameter were varied (sec. 5.1). Here the result of Eq. (3.17) will be compared to experimental results obtained from other groups. The data shown in Fig. 6.1b are divided into three groups with comparative laser pulse parameters in terms of energy and pulse duration. For the electron propagation angle θ (Eq. (2.20)) a value of 10° was estimated following [11] for the 1 J-laser-group (ASTRA, ATLAS, MBI, LOA, JANUSP), of 25° as used in [5] and confirmed by source-size-measurements [35] for the 10 J-laser-group (GEKKO, LULI, TRIDENT), and of 45° for the 100 J-laser-group (NOVAPW, RALVULCAN, RALPW) as indicated by angular resolved X-ray measurements [71]. Apart from the experimental evidence for the electron propagation angles θ with respect to the laser parameters this behavior is not understood. Regarding the range of parameters, the comparison presented in Fig. 6.1b shows a remarkably good agreement with the analytical theory within a factor of two and thus supports its generality. In case of PEM (Fig. 6.1a) the data marked with a green circle scatter up to one order of magnitude around the theoretical curve. Although the origin of this large disagreement is not clear the analytical theory depicts a major improvement.

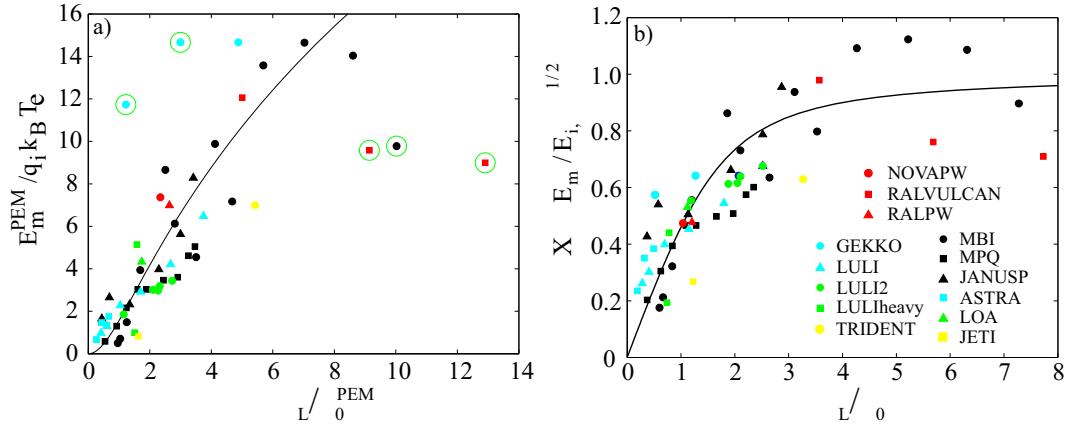


Figure 6.1: Comparison of experimental results with theory (solid lines) for PEM (a) and the analytical theory (b). The symbols denote the experimentally obtained maximum ion energies from different laser systems split in three groups with respect to the laser pulse energy; ≈ 1 J (MBI, data presented in Fig. 5.3, MPQ[11], janusp[39], ASTRA[72], LOA[73], JETI[40]); ≈ 10 J (GEKKO[74], LULI and LULI2[5], LULIheavy[37], TRIDENT[4]); and > 100 J (RALPW[38], RALVULCAN[71], novaPW[23]). A single value of θ is assigned to each group. All data refer to protons, except [37], where also C^{4+} - and F^{7+} -ions were accelerated, and [4] where monoenergetic C^{5+} ions were observed. The green circles in the left graph mark data points with maximum deviation from the theoretical curve.

6.1.2 The optimal pulse duration

Regarding the power dependence of Eq. (3.15) the final ion energy $E_{i,\infty}$ could be increased for laser systems with constant pulse energy E_L by shortening the pulse duration τ_L . However, short laser pulse duration means a reduction of the acceleration time so that massive ions cannot reach the final energy any more. That this effect is of practical relevance was demonstrated in sec. 5.1 and emphasized in Fig. 5.3 where E_m is given as a function of pulse duration for four fixed laser energies E_L . In both PEM (dashed lines) and the analytical model (solid lines) it is evident, that highest ion energies E_m^{opt} are obtained for a an optimum value τ_L^{opt} . In addition, Fig. 6.2 reveals that for ion acceleration it is not favorable to build a PW-laser with pulse duration smaller than about 100 fs for the chosen set of parameters. On the other hand, keeping the laser power P_L constant while increasing E_L and τ_L does not result in an increase of the maximum ion energy once the optimal pulse duration τ_L^{opt} is exceeded. This saturation effect ($E_m = E_{i,\infty}$ for $\tau_L \rightarrow \infty$ visible in the slope of the shaded area in Fig. 6.1) was also observed in recent PIC-simulations [75]. Note, that PEM does not show the mentioned saturation effect as depicted by the blue $P_L = 1$ PW curve in Fig. 6.2.

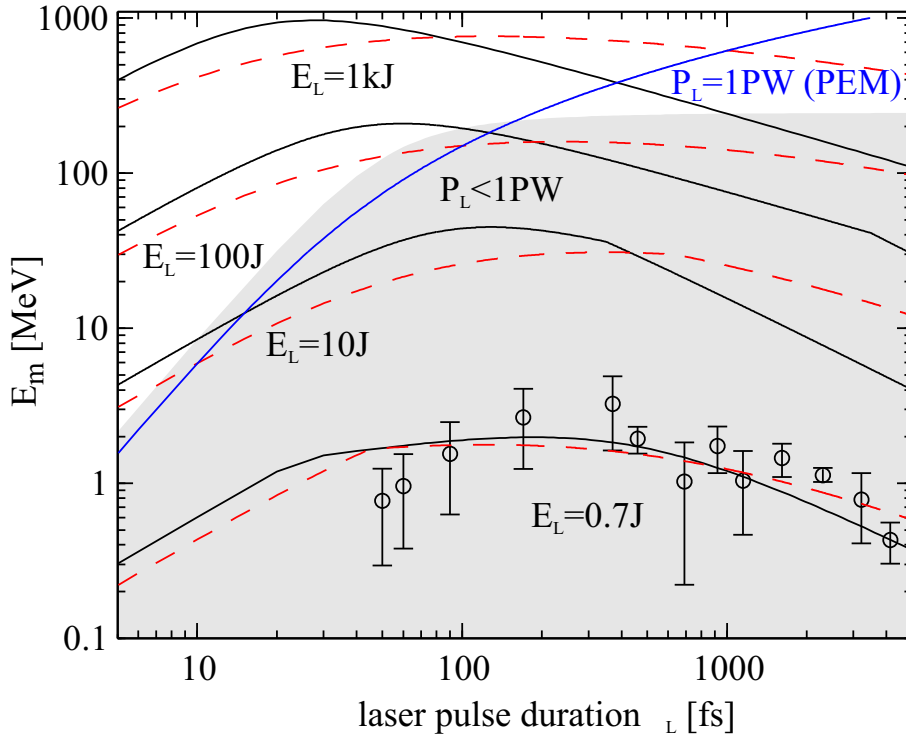


Figure 6.2: Dependence of maximum proton energies E_m on the laser pulse duration τ_L for four constant laser energies E_L . The circles represent the experimental data. The four curves for the different laser energies correspond to $r_L = 4 \mu\text{m}$, $d = 10 \mu\text{m}$, and $\theta = 10^\circ$ both for the analytical model (black solid lines) and PEM (red dashed lines). The grey shaded area denotes the region where the laser pulse power P_L is smaller than 1 PW and its boundary illustrates the saturation around 200 MeV obtained from the analytic model. In PEM there is no saturation which is seen from the $P_L = 1 \text{PW}$ curve (blue line).

It is worth to discuss the appearance of the optimal pulse duration on the basis of the analytical model in more detail. The left graph of Fig. 6.3 depicts the optimal laser pulse duration τ_L^{opt} for varying laser energy E_L . The non-monotonic behavior of τ_L^{opt} results from the explicit intensity dependence of the conversion efficiency ($\eta \propto I_L^{3/4}$ and $\eta = 0.5$ for $I_L > 3.1 \times 10^{19} \text{W/cm}^2$). It is important to note that the optimal laser pulse duration does not only depend on the energy of the laser pulse. In fact, when differentiating Eq. (3.17) with respect to τ_L and setting $dE_m/d\tau_L = 0$ it turns out that the maximum ion energy is optimized for constant values of

$$\frac{\tau_L^{\text{opt}}}{\tau_0} = \text{const.} \quad (6.1)$$

Recalling that $\tau_0 = B/(2E_{i,\infty}/m_i)^{1/2}$ where B and $E_{i,\infty}$ are defined in Eqs. (2.20) and (3.15) it is seen that the optimal pulse duration depends on many experimental

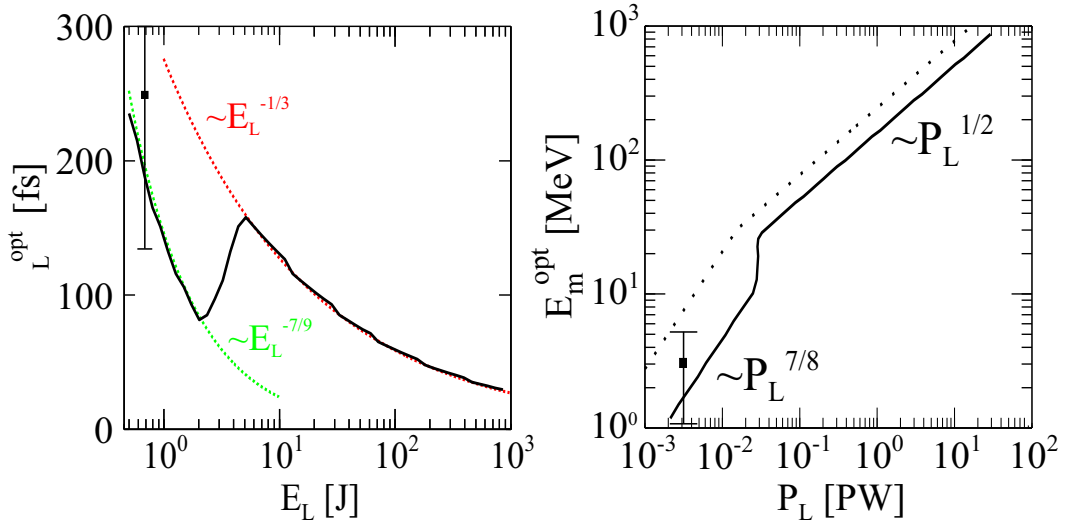


Figure 6.3: Dependence of the optimal pulse duration τ_L^{opt} on the laser energy E_L (left, black). The parameters are identical to those of Fig. 6.2. The scaling for the two regimes $\eta \propto I_L^{3/4}$ (green) and $\eta = \text{const}$ (red) are discussed in the text. The right graph shows the maximum energies E_m^{opt} (solid) and $E_{i,\infty}$ (dotted) for optimal laser powers $P_L = E_L/\tau_L^{\text{opt}}$. The data points depict the experimental results from the pulse duration scan (sec. 5.1, Fig. 6.2)

parameters in a rather complicated way:

$$\tau_L^{\text{opt}} \propto B^{\frac{16}{16-j}} \cdot \left(\frac{m_i}{q_i}\right)^{\frac{8}{16-j}} \cdot E_L^{-\frac{j}{16-j}} \cdot \begin{cases} 1, j = 4; & \text{for } \eta = \text{const.} \\ r_L^{2/3}, j = 7; & \text{for } \eta \propto I_L^{3/4} \end{cases} \quad (6.2)$$

The green and the red graph in Fig. 6.3 visualize the two regimes where $\eta \propto I_L^{3/4}$ and $\eta = \text{const}$, respectively. The solid line in the right graph of Fig. 6.3 illustrates the maximum proton energy E_m^{opt} that can be achieved under optimum conditions as a function of the laser pulse power $P_L = E_L/\tau_L^{\text{opt}}$. It shows the same dependence on the laser power as $E_{i,\infty}$ (dotted line, Eq. (3.15)), a scaling that is corroborated by recent PIC-simulations [75].

6.1.3 Heavy Ions in the analytical model

Fig. 6.4 shows the maximum energies per nucleon with respect to their charge-to-mass ratio of all ion species observed in the experiments with heated targets (Sec. 5.5). Different foil materials (W, Zr, and V) were used and all of them had remaining carbon and oxygen layers on their surfaces which could not be removed by the heating process. Not touching the non-trivial problem of describing the charge state population one could assume that all charge states q_i are generated

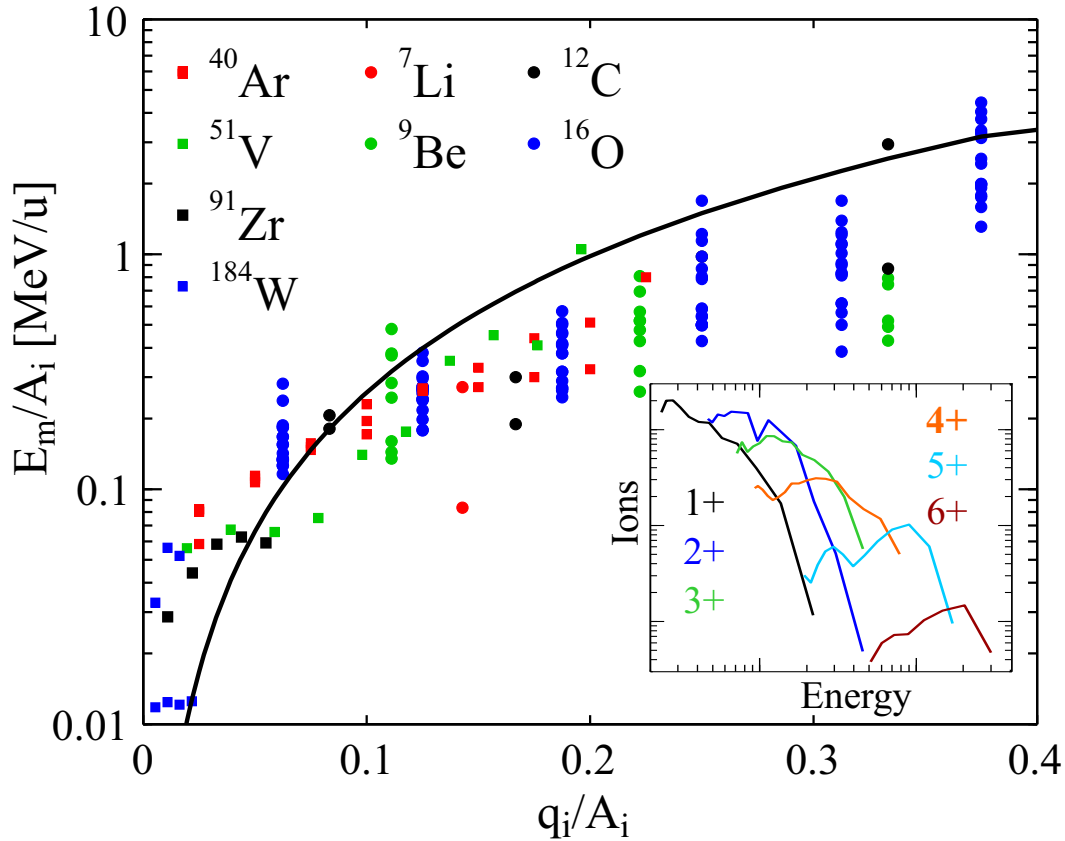


Figure 6.4: (Color) Scaled maximum ion energies vs. charge-to-mass ratios q_i/A_i . The data for fixed ratios result from different laser shots and thus give a measure of the reproducibility from shot to shot. The solid curve is obtained from Eq. (3.17). For illustration the inset shows charge state resolved energy spectra in case of oxygen.

close to the rear surface and are then accelerated in the same electric field. Fig. 6.4 shows the maximum ion energy as a function of charge state for a variety of ions. Since in the experiment all ions have been accelerated under identical experimental conditions (i.e., constant E_L , τ_L , r_L , d and θ), it can be readily seen from Eq. (3.17) that in this case the scaled ion energy E_m/A_i is a unique function of q_i/A_i where A_i is the ion nucleon number. The solid curve in Fig. 6.4 represents this function and shows a fair agreement with experimental data ranging from Li- to W-ions.

6.1.4 Limitations of the analytical model

In addition to the description of the ion energies one could hope to draw conclusions for the electrons, too. It was quoted that only a few electrons

$$N_{esc} = N_e \exp(-E_\infty/k_B T_e) \quad (6.3)$$

can escape the potential barrier E_∞ (Eq. (3.4)) built up by the surface charges. Since in all experiments $E_\infty/k_B T_e \gg 1$ only a small number of electrons can escape, i.e., nearly all hot electrons remain bound to the target giving rise to the phenomenon of recirculation as proposed by Mackinnon *et al.* [39]. In this picture the electrons reentering the target may be reflected at the front surface of the target caused by the same mechanism as described for the rear side. The electrons would then return to the rear surface after a third passage through the foil and contribute to the acceleration field additionally to the electrons passing the foil only once. This effect is neglected in the model so far.

It seems to be tempting to identify N_{esc} (Eq. (6.3)) with the number of electrons arriving at a detector, but it turns out that this number is several orders of magnitude smaller than number of the observed electrons ($\approx N_e/1000$). Nevertheless, due to the exponential dependence of N_{esc} on E_∞ a lowering of the barrier by just a factor of 2 would bring the number of escaping electrons in coincidence with those detected. On the other hand, the model is very simple and does not describe the dynamics during the formation of the surface charge. As pointed out earlier electrons travel to a distance of λ_D and back before they reenter the foil, thus setting up the equilibrium situation. In fact, during the phase where this situation builds up electrons with energies smaller than E_∞ can escape, and as a maximum estimate $N_{esc}^{max} = N_e(2\lambda_D/c\tau_L) \approx N_e/10$ electrons would reach the detector. This value is clearly too high but shows a possible way to extend the model taking into account the dynamics of the electrons in their self-induced field which is not a simple task where the three-dimensional, radially symmetric nature of the model needs to be taken into account and can probably be described in a numerical model only. Developing this code is beyond the scope of this work but seems to have the potential to describe not only electron measurements connected to the ion acceleration experiments but also the angular characteristics of the ion emission and their source sizes.

6.2 Interpretation of the scraper measurement

6.2.1 The radial field profile

In recent works field ionization was identified as the dominant ionization mechanism [36] providing the accelerated ions. A significant number of ions with a certain charge state q_i thus can be produced only in regions where the field exceeds the re-

spective threshold. Here only an order of magnitude estimate is necessary so that the model for field ionization by barrier suppression is sufficient. This predicts a threshold field [36]

$$F_{th} = \frac{I_p^2 \pi \epsilon_0}{q_i e} = 1.73 \cdot 10^8 \text{V/m} \cdot \frac{I_p^2}{q_i} \quad (6.4)$$

where I_p is the ionization potential for the respective ion in eV (the energy needed to produce, for example, C^{4+} from a C^{3+} ions). Note, that this assumption also implies a sequential ionization $q_i \rightarrow q_i + 1$, multiple ionization processes such as $q_i \rightarrow q_i + j$, $j > 1$ are neglected. Numerical values for I_p can be found, for example, in [76].

With these assumptions F_{th} depicts a lower boundary for the field in the region where the charge state q_i is created. On the other hand the appearance of a maximum ion charge state suggests that the field has never been larger than the threshold for the ionization to the charge state $q_i + 1$ thus giving an upper bound. Obviously this picture implies that no charge exchange occurs once the field ionization process has finished. Following this interpretation Fig. 5.5 was used to derive boundaries for the maximum electric field for different radial distances from the center of the ion emission (Fig. 6.5). The field strength in the center of the emission area was estimated using Eq. (2.28). The transversal extension is of the same order of magnitude as described by Romagnani *et al.* [34] using proton deflectometry. Unfortunately in the work cited no transversal field shape was deduced with which one could compare.

One could hope to explain the observed transverse field distribution within the analytical model. As mentioned before for $r > 0$ Eq. (3.2) which defines the potential distribution of the surface charge can not be integrated analytically. For the numerical integration it is convenient to normalize the radial coordinate r to the radius of the surface charge B , $\rho = r/B$, in the same way as $\xi = z/B$ was defined for the longitudinal coordinate. Eq. (3.2) then reads

$$\Phi(\xi, \rho) = \frac{E_\infty}{e} \cdot \frac{1}{2\pi} \int_0^{2\pi} \int_0^1 \frac{\rho' d\rho' d\phi}{\sqrt{\xi^2 + \rho^2 + \rho'^2 - 2\rho\rho'\cos\phi}} \quad (6.5)$$

with E_∞ defined by Eq. (3.4). Once this integral was solved the electric field can be calculated for different radii B of the surface charge via

$$F_r(r, z) = -\frac{1}{B} \cdot \frac{\partial\Phi(\xi, \rho)}{\partial\rho} \quad (6.6)$$

$$F_z(r, z) = -\frac{1}{B} \cdot \frac{\partial\Phi(\xi, \rho)}{\partial\xi}. \quad (6.7)$$

Fig. 6.6 shows the normalized values of the potential $e\Phi(\xi, \rho)/E_\infty$ (a), the radial field component $eB/E_\infty \cdot F_r(\xi, \rho)$ (b), and the longitudinal field component $eB/E_\infty \cdot$

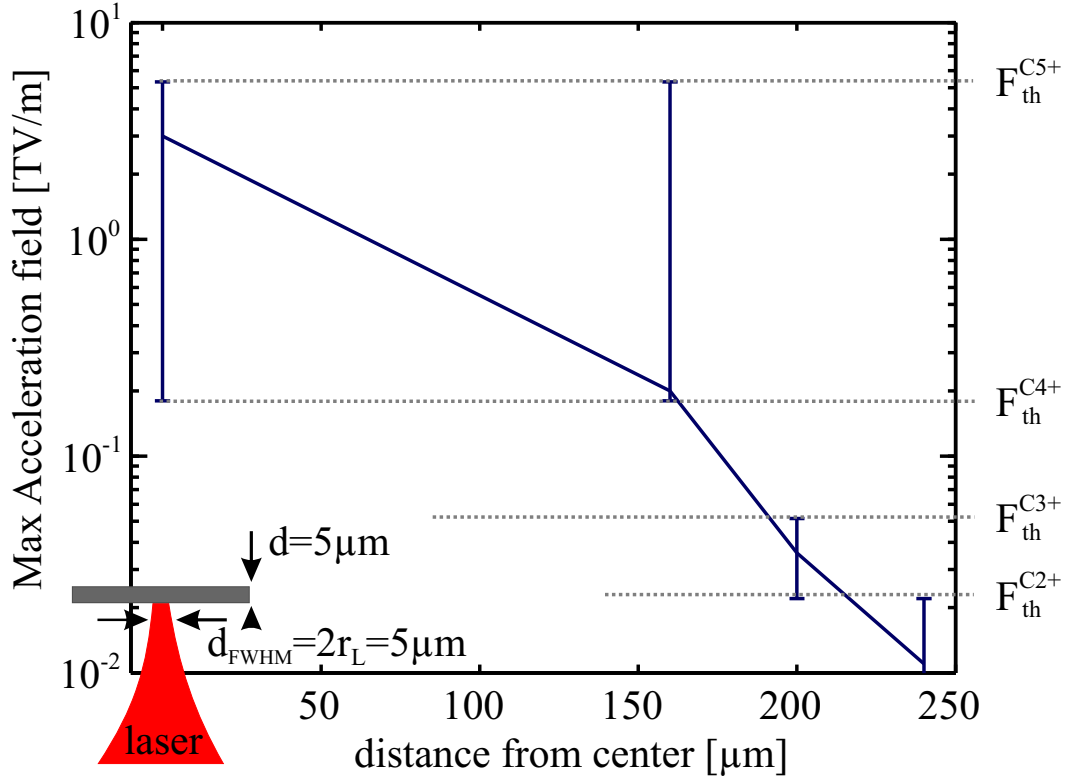


Figure 6.5: Radial profile of the maximum field which was present during the acceleration process. The limits marked by the error bars represent the threshold fields for sequential field ionization F_{th} (Eq. (6.4)).

$F_z(\xi, \rho)$ (c) obtained from the numerical evaluation of Eqs. (6.5) and (6.6). For the source size measurements described in Sec. 5.2 it was $r_L = 2.5 \mu\text{m}$, $d = 5 \mu\text{m}$ and $\theta = 10^\circ$ resulting in the surface charge radius (Eq. (2.20)) $B = 3.4 \mu\text{m}$. Thus, in the model the electric fields drop about 2 orders of magnitude within only $35 \mu\text{m}$ which does not agree with the estimation from Fig. 6.5 and is not surprising when keeping in mind the simplicity of the model. It is likely that the observed effect can be described by the extensions of the model discussed in Sec. 6.1.4.

6.2.2 The source sizes

Due to the small solid angle of the Thomson parabola spectrometer (10^{-4} msr) as compared to the opening angle of the emitted ion beam (≈ 25 msr), the knife-edge method can not be used for the complete characterization of the source. In recent experiments [27], it was shown that the proton beams emitted from the rear side of thin foils exhibit a small normalized emittance ($< 0.004\pi$ mm·mrad). Moreover, their angular divergence depends linearly on the radial distance to the laser focal

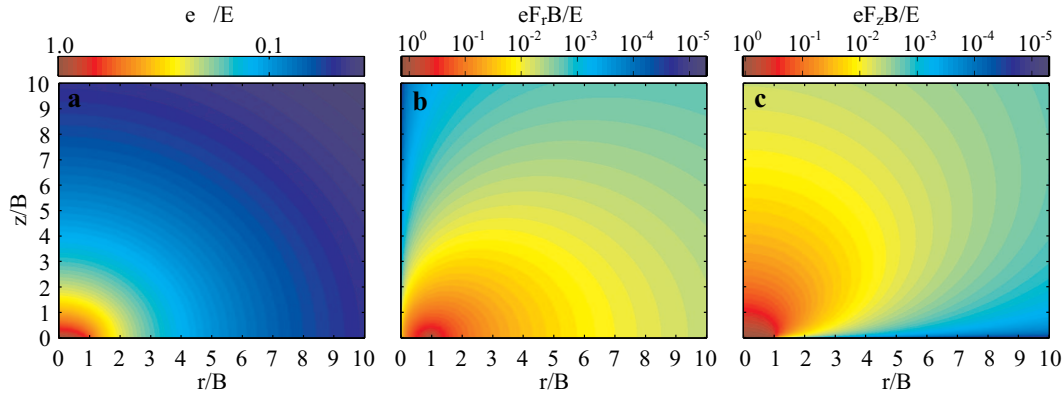


Figure 6.6: Numerical solution of Eq. (6.5) showing the potential Φ (a), the radial electrical field component F_r (b), and the longitudinal field component F_z (c).

spot for the considered proton energies. If these results apply to the present case, the ion signal should vanish as soon as the scraper passes the center of the emitting area. In fact this is what happens for the high-energy protons and C^{4+} -ions (Fig. 5.5a-b) while the low energetic protons and carbon ions are still detectable. They might have a larger emittance or emit more straight than the high energetic ions so that ions from the outer areas are able to hit the pinhole of the spectrometer.

To find a lower limit for the measured source sizes, it appears most feasible to assume that the ions come from a circular source and every point makes the same contribution to the spectrometer signal. For this case, the measured signal can be written as $S = N_0/2 \left[1 - 2/\pi \left(\arcsin x_n + x_n \sqrt{1 - x_n^2} \right) \right]$, where N_0 is the number of ions in a certain energy interval observed without using the scraper and $x_n = 2x_s/s$ is the scraper position x_s divided by the energy-dependent source size s , which is the fit parameter. Fig. 6.7 shows the calculated source sizes of protons and carbon ions as a function of their kinetic energy resulting from the above model assumptions. The denoted values represent a lower boundary for the source diameters except for the high-energy ions which are confined by the smallest detectable diameter of $80 \mu\text{m}$. Note that the source sizes exceed the dimensions of the experimental parameters by a factor of 100, i.e., up to $\approx 500 \mu\text{m}$ source diameter compared to $5 \mu\text{m}$ thick targets and $5 \mu\text{m}$ FWHM-diameter of the laser focal spot. The source sizes are of the same order as referred to by other groups (see, for example, refs. [26] and [27]).

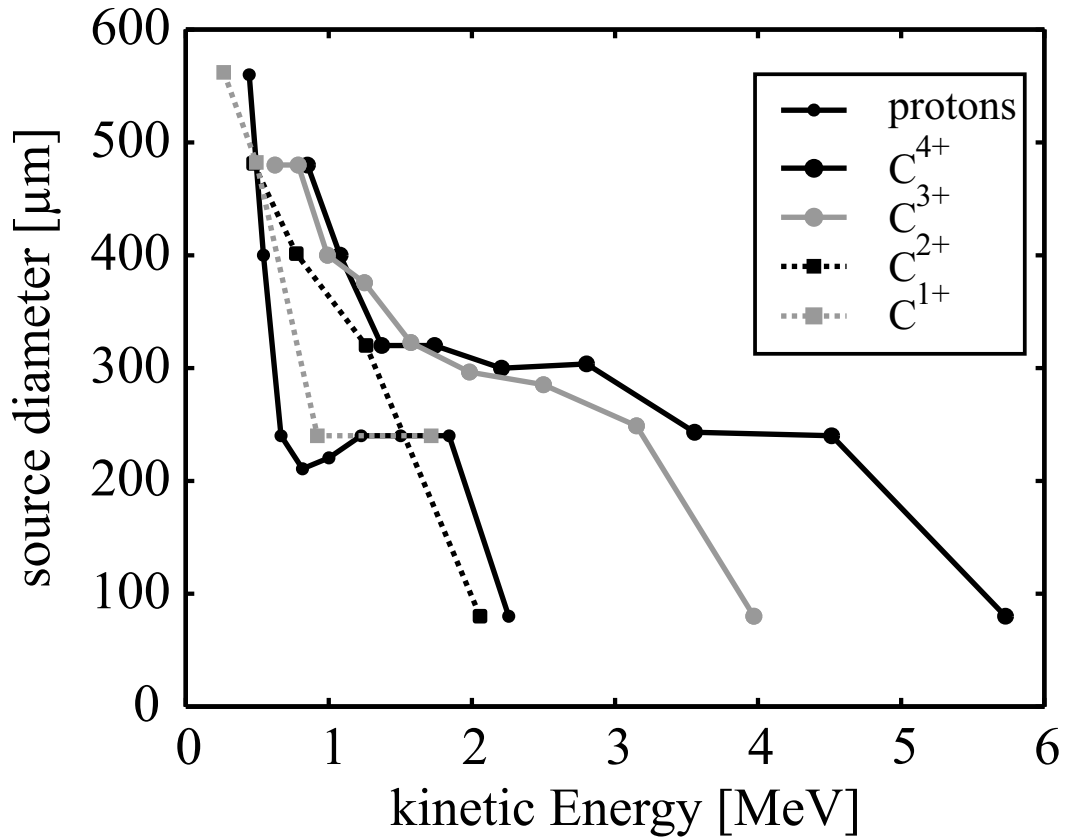


Figure 6.7: Proton and ion source sizes versus kinetic energy. The values represent lower limits for the source diameters.

6.3 Ion acceleration from buried layers

From the experiment it is possible to deduce how far the acceleration field penetrates the solid foil at the rear side. The carbon ions were most effectively accelerated. This agrees well with the picture, that the most energetic ions originate from the very front layers which was carbon, as proofed by the ERDA measurements. The nitrogen ions occurred with a factor of 10 lower ion numbers compared to the carbons. The lower energies suggest that nitrogen ions were accelerated in a lower field, i.e., a field which was suppressed by the precursory carbon ions. The similarity between the ion spectra of the shots with 3 nm and 50 nm layer depth suggests that the accelerating electric field reaches ions up to a depth of 50 nm or even more. This can be understood by the following consideration.

The positive surface charge Qe which is responsible for the rear side field outside the foil is completely shielded by mobile nearly free target-electrons within distances $\lambda_{Ds} = v_F/\omega_{ps}$, where v_F is the Fermi velocity and ω_{ps} the plasma frequency of the target material (*static* screening by target electrons [77]). The fast

electrons ($\approx c$) which turn around and reenter the foil are *dynamically* shielded over distances $\lambda_{Df} \approx c/\beta\omega_{ps}$, where $\beta \approx 0.1$ [78]. While for typical solid state targets λ_{Ds} is of the order of 0.1 nm the shielding distance for MeV hot electrons becomes $\lambda_{Df} \approx 40$ nm. Thus, also buried target ions with distances up to λ_{Df} from the rear side feel a negative driving charge and an accelerating field.

6.4 Mono-energetic ion beams

For the first time it was possible to observe mono-energetic C^{5+} -ion beams from laser irradiated thin palladium foils. This was achieved by reducing the thickness of the rear-side carbon layer by controlled heating. It could be shown experimentally that this is one necessity, because ions, specially the low energetic ones, can originate from layers as deep as 50 nm inside the solid. However, in section 5.2 it was shown, that the field at the rear surface transversally extends over several $100 \mu\text{m}$ and that low energetic ions also originated far from the axis. This is in contradiction with the proposed explanation in [4] where it was quoted that only a reduction in thickness of the source layer leads to a mono-energetic energy distribution of the accelerated ions. Esirkepov *et al.* [79] proposed a small dot as an ion source, which is constricted transversely and longitudinally to extensions much smaller than the extension of the electric field. This proposed scheme was successively applied in an experiment by Schwoerer *et al.* [40] where mono-energetic protons with 1 MeV energy were observed.

Up to now the found contradiction is not resolved. It seems likely that the scheme of Esirkepov *et al.* can be applied for the observed mono-energetic C^{5+} -ion beams, too. One could speculate that the thin carbon sheath which develops during the target heating is not homogeneously thick, i.e. carbon islands develop rather than a continuous monolayer sheath. Another possibility is that the ionization mechanism plays a role. One could think of a field, which transversely decreases as found in Sec. 5.2 and by Romagnani *et al.* [34]. The field in the center is large enough to produce C^{5+} by field ionization. However, it rapidly drops to lower values with increasing radial distance to the maximum, i.e., no C^{5+} -ions are produced. This could be interpreted as a transversally restricted source for C^{5+} -ions, giving the same picture as proposed by Esirkepov *et al.* [79]. In this case also lower carbon charge states should have been observed which is in contradiction with the experiment. However, those lower charge states could be emitted with a certain angle with respect to the target normal direction and thus not reach the detector pinhole.

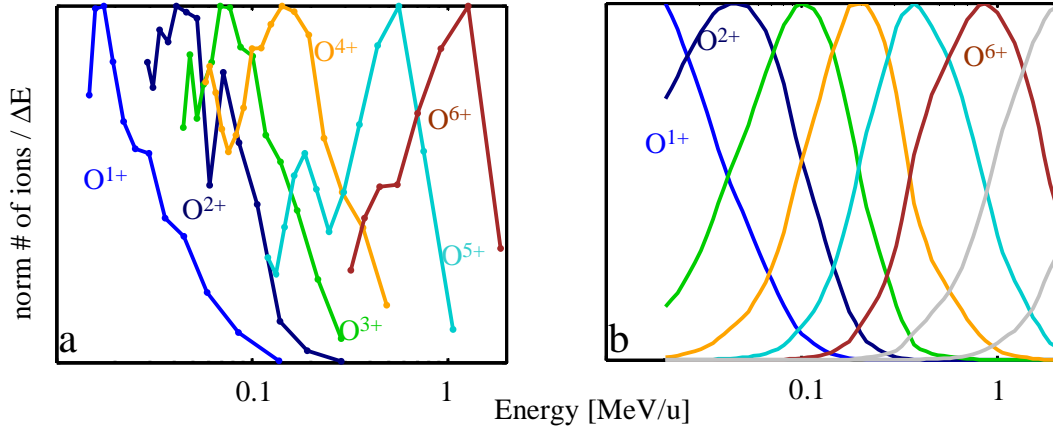


Figure 6.8: Oxygen charge state distributions from the laser plasma experiment described in Sec. 5.5 (a) and after a carbon stripper foil from ref. [80] (b). Each charge state spectrum was normalized to a maximum of one.

6.5 Charge state distributions of heavy ions

This section is attributed to heavy ion charge state distribution described in section 5.5. The energy distributions of the observed charge states of oxygen and argon showed distinct maxima and did not follow the usual exponential shape. In a certain way each charge state could be called mono-energetic. Fig. 6.8a shows the same oxygen energy distribution as in Fig. 5.9a, but each charge state spectrum was normalized to a maximum of one. The obtained charge state distribution reminds on a equilibrium charge state distribution as one would expect from a ion beam with a continuous energy distribution which has passed a stripping medium. Fig. 6.8b shows such a distribution for oxygen ions which have passed a carbon stripper foil [80]. It is unlikely that the observed charge state distribution is a direct effect of the accelerating field. Although lower charge states would be expected to gain less energy in a constant field, the absence of low energy ions with the respective charge state can hardly be explained. Thus, the similarity between both charge state distributions suggests the existence of a medium in the laser-plasma experiment which acts like a stripper medium to the oxygen ions. Similar considerations are also true for the argon ions. In the following subsections, possible stripper candidates will be discussed.

6.5.1 The influence of the residual gas

The discussed experiments are performed under poor vacuum conditions. The residual gas pressure was of the order of 10^{-4} mbar ($N \sim 2.7 \cdot 10^{12}$ particles/cm³). In a solid medium ($N \sim 2.7 \cdot 10^{22}$ particles/cm³), the equilibrium charge state is reached after 10 nm of propagation [81]. This rough approximation would lead to an equilibrium length of 100 m for the residual gas pressure in the vacuum chamber, much larger than the minimum mean free path $L_{mfp} \approx (10^{-15} 2.7 \cdot 10^{12})^{-1} \text{cm} = 3.7 \text{ m}$ for electron exchange in gases [82]. The distance to the detector is usually one meter. Thus, it is unlikely that the residual gas has an influence on the charge distribution measured in the detector. However, the target heating could degrade the vacuum due to evaporating material, which was not controlled during the experiment.

The cross section for electron exchange is strongly dependent on the projectile energy. For the relevant energy range these cross sections were measured by MacDonald *et al.* [82] for oxygen ions in nitrogen. These values can be used to solve the set of differential equations, which describe the electron exchange (Eq. A.1). Fig. 6.9 shows the result for three different nitrogen pressures, i.e., (a) 10^{-4} mbar, (b) 10^{-3} mbar, and (c) 10^{-2} mbar. The calculations were started with the total oxygen energy distribution assuming a charge state of six (see inset of Fig. 5.9a) following the assumption that the field at the target rear-side is high enough to field-ionize oxygen to the helium-like charge state. It is obvious, that, unless the target chamber pressure exceeds 10^{-2} mbar, electron exchange with the residual gas can be ruled out as a factor which determines the charge distributions. Nevertheless one has to keep in mind, that eventually the pressure can be much higher close to the target because of the evaporating material. A locally enhanced pressure, i.e., 1 bar for a distance of $10 \mu\text{m}$ or a solid medium with a thickness of 10 nm would lead to a comparable charge distribution as depicted in Fig. 6.9d, which is close to the measured one.

6.5.2 The target rear side

If not the residual gas is responsible for the observed charge state distributions another remaining candidate is the expanding plasma cloud at the rear surface of the irradiated targets. In more detail, the electrons which exit the target are decelerated and turn around at the hot electron Debye-length as discussed in chapter 3. When re-entering the target they will have regained their initial energy.

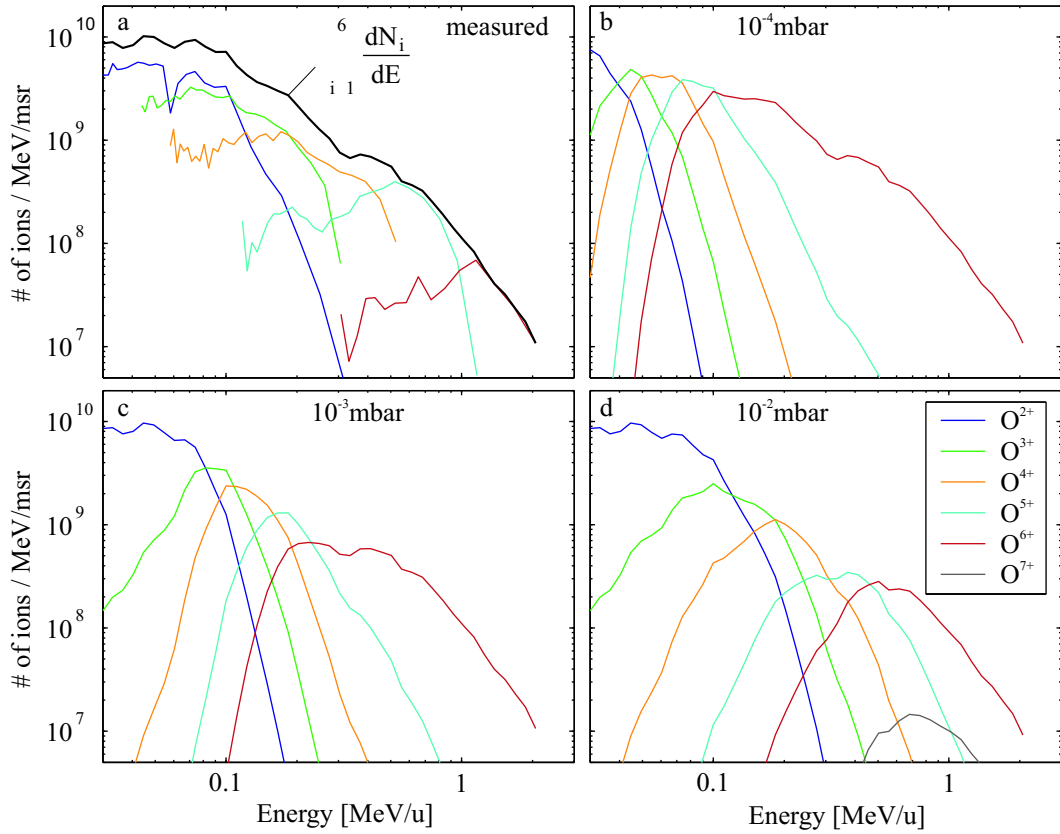


Figure 6.9: Oxygen charge state distributions as measured (a) and as they would appear after 1 m propagation in nitrogen with a residual gas pressure of (b) 10^{-4} mbar, (c) 10^{-3} mbar, and (d) 10^{-2} mbar. The charge state distributions (b-d) are obtained by solving the set of differential equations for electron exchange (A.1) with cross sections from [82].

The returning electrons carry currents of the order of 1 MA. These high currents may heat the target and evaporate the rear surface resulting in a gas cloud which acts like a stripper material on the accelerated ions.

However, the up to now unknown stripper medium can be characterized by its mean equilibrium charge state and the corresponding width as described in the Appendix. These energy dependent quantities were treated as unknown fit parameters which were adapted to reproduce the observed oxygen charge state spectra best. Fig. 6.10 shows the resulting mean charge states (a) and the charge state distribution widths (b). The solid curve represent the experimental data for oxygen ions passing a carbon stripper foil [80]. The dashed curves result from semi-empirical formulas given in [83] for the mean charge states and [84] for the charge state distribution widths.

From the considerations above the presence of an unknown stripper material

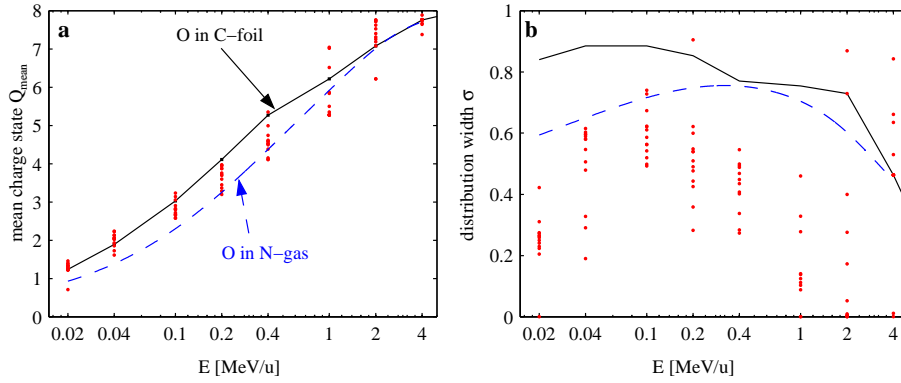


Figure 6.10: Mean charge states (a) and charge state distribution widths (b) for oxygen ions. The solid curves depicts the values for oxygen ions passing a carbon foil [80]. The dashed curves are the results of an empirical formula given by Schiwietz *et al.* [83] (a) and Sayer [84] (b).

can be deduced. The calculated mean charge states (Fig. 6.10a) could correspond to both a gaseous or solid stripper. On the other hand, the calculated charge state distribution widths (Fig. 6.10b) are closer to the width predicted for oxygen passing a nitrogen gas (dashed curve) suggesting that a gaseous stripper medium is responsible for the observed oxygen mean charge state distributions.

As mentioned earlier a huge number of electrons ($N_e \approx 10^{13}$) with a mean energy of several MeV penetrate the target and are even forced to recirculate. Assuming a mean energy loss of $\Delta E/\Delta x \approx 20 \text{ keV}/\mu\text{m}$ in a solid target with electron density $q_s n_s \approx 10^{23}/\text{cm}^3$, the target electrons in a volume $A \cdot \delta x$ are heated to a temperature

$$k_B T_{e,t} \approx \frac{N_e \Delta E}{q_s n_s \cdot A \cdot \Delta x}. \quad (6.8)$$

Not touching the difficult problem of the energy transfer from the electronic system to the lattice via electron-phonon coupling it is easily seen that the tungsten target can be heated above the boiling temperature in a circular area with radius $r_b \approx 80 \mu\text{m}$. This order of magnitude estimation shows that the target may be evaporated by the hot electrons which, by the way, is also consistent with the fact that the target has a hole of several $100 \mu\text{m}$ diameter after the laser shot. Although the evaporation may happen within several ps due to the electron-phonon coupling it may produce the gaseous stripper medium mentioned above. It is unlikely that the fast ions which are generated within the laser pulse duration (several 100 fs) interact with this stripper. On the other hand, the charge states of the low energetic ions which can originate from 50 nm deep buried layers (Sec. 5.3) may be already influenced.

Chapter 7

Summary and Perspectives

7.1 Results of the thesis

The presented work focussed on ion acceleration from the rear side of high intensity laser irradiated foils, often referred to as target normal sheath acceleration (TNSA). Experimental and theoretical investigations improved the understanding of the underlying processes.

An analytical model was derived which described the experimentally observed maximum ion energies. The applicability of this model to a wide range of experimental data was shown. It describes the dependence of the ion maximum energy on target thickness, laser pulse energy, intensity and duration, and the charge and mass of the accelerated ions. The model also predicts the energy of mono-energetic ions recently observed for the first time.

It could be shown that the acceleration field extends transversely over distances which are 100 times larger than the focal spot size. Not only the low energetic protons, but also low charge states of heavier ions originate from the outer part of the acceleration zone. Also longitudinally the field penetrates the solid foil much deeper ($\approx 100x$) than expected from static screening. By restricting the ion source layer to small thicknesses and transversal extensions all ions see comparable electric field strength resulting in mono energetic ion energy distributions.

Mono-energetic bunches with 5×10^7 C^{5+} -ions at an energy of 3 MeV/u and 17% energy spread were observed. In this experiment palladium foils heated to temperatures of 1200 K develop a thin carbon source layer with thicknesses below 0.5 nanometers. This restriction of the ion source seemed to be sufficient for mono

energetic ion production.

Equilibrium charge state distributions of oxygen were observed in experiments with heated targets. It was shown that this could not be caused by the residual gas pressure in the vacuum chamber. Mean charge states and charge state distribution widths were calculated from the measured spectra. The origin of the observed equilibrium charge state distributions could not fully be clarified and is subject of further investigation.

7.2 Future laser development

After the invention of the laser the power was increased mainly by decreasing the laser pulse duration. At the end of the 70's stagnation set in which could be overcome by the invention of the chirped pulse amplification (CPA) technique by Strickland and Mourou [16]. After the first realization the laser pulse power could be increased by 6 orders of magnitude within one decade. The Exa- and Zetta-Watt regime seemed to come into reach (Fig. 7.1, [18]). But since the first PW-laser was built in the Lawrence Livermore Laboratory a new stagnation phase has started (Fig. 7.1, red curve). Thus, the CPA technique followed the common trace of development for any technical machine. For a long time it provided for a strong increase in laser power and in principle it could still. However, the efforts in terms of the size of the laser components [18] which comes along with a low repetition rate of the laser due to the long cooling times of the amplifier media would be tremendous. Currently a PW-CPA-laser system is under development at the Friedrich-Schiller-University in Jena, Germany, which is planned to operate with a comparably high repetition rate of 0.1 Hz [88]. However, regarding the approach of even higher laser powers calls for a new technique.

The most hopeful candidate for high-repetition rate (kHz) high power (> 1 PW) laser systems is the optical parametric chirped pulse amplification (OPCPA) technique [85]. This technique is currently under development at the Max-Planck-institute for quantum optics, Garching, where the PW-regime with ultrashort (5 fs) laser pulses will be entered within the PetaWatt-Field-Synthesizer (PFS) project during the next years [89]. The PFS is planned to be used as a front end for the 200 PW laser of the Extreme-Light-Infrastructure (ELI) project [90] (blue dotted curve in Fig. 7.1).

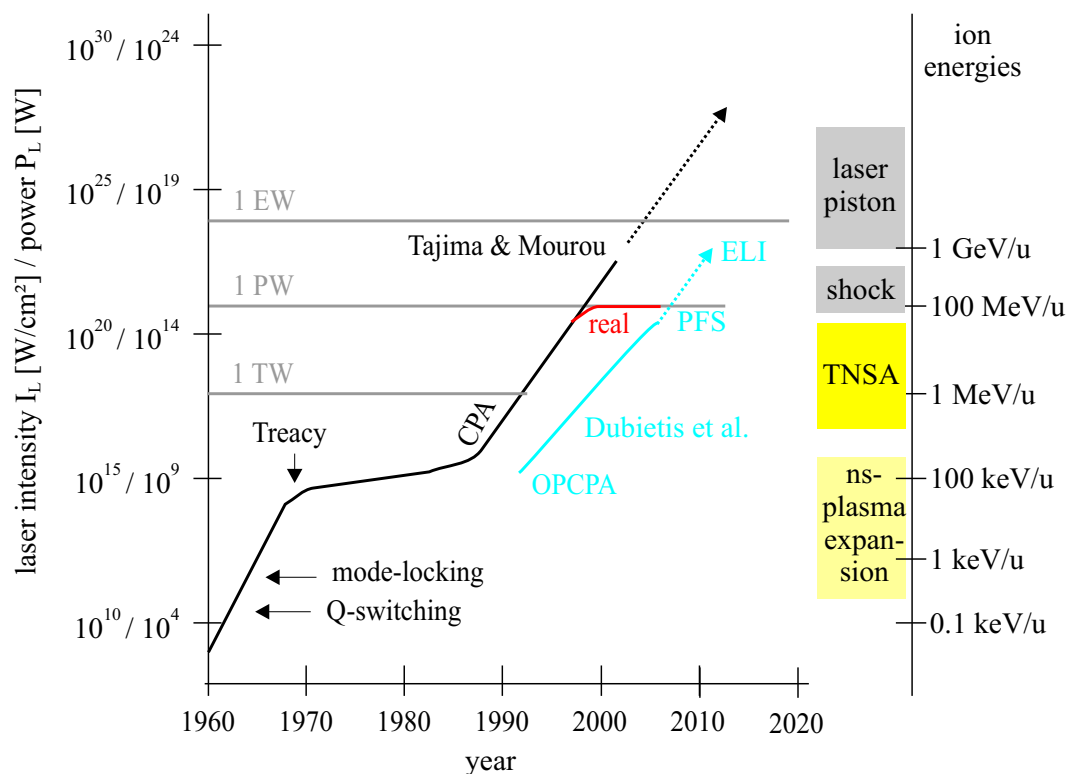


Figure 7.1: History and future of high intensity/power laser pulses. The solid black curve is taken from Tajima and Mourou [18] and depicts the development of the laser intensity and power resp. since the invention of the laser. This trend needed to be corrected (red line) since the 1PW threshold was not overcome since the first realization at the Lawrence Livermore Laboratory, USA. Conventional chirped pulse amplification (CPA) might be replaced by optical parametric CPA (OPCPA) soon (blue line, taken from Dubietis *et al.* [85]). The dotted extension depicts future plans, for example the PFS laser at MPQ and the 200 PW laser of the Extreme Light Infrastructure (ELI) project. The right column shows the evolution of the ion energies observed in laser plasma experiments with the respective intensities. For laser powers exceeding 1PW the ion acceleration is expected to be dominated by shock acceleration [86] which will meet the laser piston acceleration regime for even higher intensities [87].

7.3 Perspectives of laser-ion acceleration

The right axis in Fig. 7.1 shows the ion energies obtained in laser plasma experiments with the respective laser pulse powers. Currently the TNSA-regime which was discussed in the presented work offers maximum ion energies up to 200 MeV/u for 1PW lasers. It could be shown that for a PW-laser these energy can be obtained with the optimal laser pulse duration of the order of 100 fs. For TNSA it is not preferable to increase the power by shortening the laser pulses. However, when further increasing the laser power and changing the target properties new

acceleration schemes will dominate which will be illuminated in the following.

7.3.1 Double layer targets

For most applications high quality ion beams are essential, i.e., they should be mono-energetic. It could be shown that in principle this can be achieved by reducing the source volume in a way that all ions experience the same field during the acceleration. Thus, the transversal confinement of the source layer to sizes of the order of the laser focal spot is needed. Moreover, also the longitudinal confinement is important. Here it is not sufficient to make the source layer thin enough. As described in the analytical model the hot electrons generate a surface charge on the target rear surface whose field forces the electrons to turn around. The ions from the surface are accelerated in these fields while the target itself does not expand, thus, the rear surface remains in its original position. This may be true only if the charge-to-mass ratio of the target material is much less than the one for the accelerated ions. In this case the ions can detach from the target substrate. Moreover, if the ion number in the detached bunch is small enough, i.e., if the initial ion layer is thin enough, a mono-energetic bunch is formed [79]. Large ion numbers would necessarily lead to Coulomb interactions between the ions and result in a broadening of the spectrum. Note, that this picture is assumed in the analytical model since no expansion of the target is described so that the rear surface remains at its initial position $z = 0$ and, in principle, only the one ion which gains the maximum ion energy is treated.

7.3.2 The influence of the target size

As illustrated in Fig. 2.2 in experiments with wide (≈ 1 mm) targets the electrons can transversely spread over large areas. This is the main reason why recirculation may be neglected in the model derived in chapter 3 and the acceleration can be considered to be over after the laser pulse duration τ_L . Especially for short pulses this cancellation avoids ions to gain the maximum possible energy $E_{i,\infty}$ (Eq. (3.15)) which depends on the square root of the laser power P_L only. When the target is restricted to small transversal sizes the picture considerably changes as will be discussed in the following.

For simplicity a spherical target with diameter d will be considered under laser irradiation (Fig. 7.2). The electrons may again propagate through the target

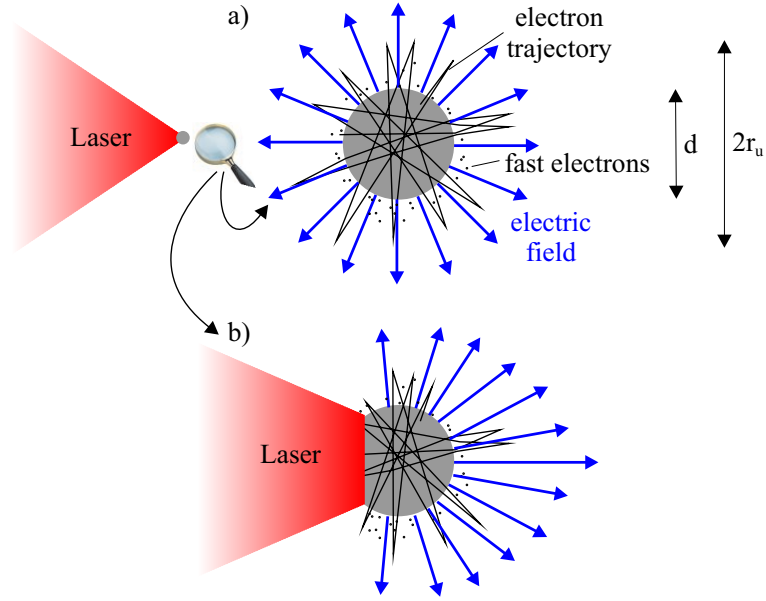


Figure 7.2: Scheme of laser interaction with a spherical target with diameter d . Electrons are heated due to the laser and are forced to recirculate around the target by their self-induced fields thereby spreading over a sphere with average radius r_u (a). In reality the symmetry will be broken at least as long as the laser pulse irradiates the target (b).

where they are dynamically shielded. When they exit into the vacuum the electrons induce a charge at the surface of the sphere so that an electric field evolves. Considering immobile target ions, i.e., a heavy target material, the target will not expand and after the laser pulse has passed an equilibrium will have formed where Q_K electrons are permanently outside the target. It is assumed that this happens very fast, i.e., the laser is sufficiently short (< 30 fs). The electrons quickly spread around the sphere so that its potential Φ_K is assumed to be spherically symmetric and may be expressed as

$$e\Phi_K(r) = \frac{E_\infty^K}{\rho} \quad (7.1)$$

where $\rho = 2r/d$ is the radial coordinate normalized to the radius of the sphere $d/2$ and

$$E_\infty^K = \frac{Q_K e^2}{2\pi\epsilon_0 d} \quad (7.2)$$

denotes the energy an electron needs to escape the potential. The electrons have an exponential spectrum (Eq. (3.1)) with mean energy $k_B T_e$. Electrons exhibiting this energy will turn around at a radial distance $r_u = \rho_u \cdot d/2$ with

$$\rho_u = \frac{1}{1 - k_B T_e / E_\infty^K} \quad (7.3)$$

where

$$\lambda_D^K = d/2(\rho_u - 1) \quad (7.4)$$

may be identified with the hot electron Debye-length for a spherical target. Assuming that on average each electron with maximum velocity v_e oscillates around the sphere up to the distance $r_u = \rho_u d/2$ (Fig. 7.2) in one oscillation period it will be outside the target for a time

$$t_{out} = \frac{2\pi}{\omega_p} = \frac{2\pi\lambda_D^K}{v_e} \quad (7.5)$$

whereas it spends the time

$$t_{in} = \frac{2d}{v_e} \quad (7.6)$$

inside the target not contributing to the field. Thus, from the N_e produced electrons (Eq. (2.21)) only $Q_K = N_e t_{out}/t_{in}$ electrons are permanently outside the target which therefore appears with the same charge. Substituting with Eqs. (7.2)-(7.6) one derives

$$Q_K = \frac{d}{4r_c} \left(1 + \sqrt{1 + \frac{4\pi r_c}{d} N_e} \right) \quad (7.7)$$

with the distance of closest approach $r_c = e^2/(4\pi\epsilon_0 k_b T_e)$ which is of the order of 1 fm for MeV-electrons. For usual laser parameters ($E_L > 1$ J) and target diameters ($d \approx 10 \mu\text{m}$) Eq. (7.7) can be approximated by

$$Q_K \approx \sqrt{\frac{\pi d}{4r_c} N_e} = \sqrt{\eta E_L \frac{\pi^2 \epsilon_0 d}{e^2}} \quad (7.8)$$

where Eq. (2.21) was used. Substituting Q_K in Eq. (7.2) gives the relation

$$E_\infty^K \approx \sqrt{\frac{\eta E_L}{d} \cdot \frac{e^2}{4\epsilon_0}}. \quad (7.9)$$

As already mentioned, E_∞^K denotes the minimum energy an electron needs to get free. Obviously, in reality it takes about the laser pulse duration until the field is set up and also because of its light pressure the laser may deform the field from being spherical symmetric. Nevertheless, this expression (7.9) may be used for some order of magnitude estimates.

Considering an ion with charge q_i at the surface of the laser irradiated sphere. Under the condition that the main target does not essentially expand, i.e., the charge-to-mass ratio q_s/m_s of the target ions is much smaller than the ions charge-to-mass ratio q_i/m_i , the ion can gain the energy

$$E_{i,\infty}^K \approx q_i \sqrt{\frac{\eta E_L}{d} \cdot \frac{e^2}{4\epsilon_0}} = 169 \text{ MeV} \cdot q_i \sqrt{\frac{\eta E_L [\text{J}]}{d [\mu\text{m}]}}. \quad (7.10)$$

If the initial ion layer is thin enough one even would expect the ion bunch to be mono-energetic as discussed in Sec. 7.3.1. Comparing Eq. (7.10) with a recent

publication by Ter-Avetisyan *et al.* [91] where 1 MeV protons were obtained from $d = 20 \mu\text{m}$ water droplets irradiated with 35 fs-laser pulses $E_L = 0.75 \text{ J}$ focussed to an intensity of $\approx 10^{19} \text{ W/cm}^2$ shows that Eq. (7.10) overestimates the maximum ion energy with $E_{i,\infty}^K \approx 10 \text{ MeV}$. This could be due to neglecting the temporal evolution of the field during the laser irradiation where ions would already start to accelerate before the maximum field is set up, thus resulting in a smaller final energy. Also the fact that water as a target material is not heavy enough to sustain its spherical shape but starts to expand which also would lower the field. However, for an order of magnitude estimate the simple spherically symmetric model may be squeezed a bit more.

From Eq. (7.10) one could hope to increase the ion energy by reducing the target diameter. On the other hand the number of electrons outside the target (Q_K , Eq. (7.8)) can not exceed the number of electrons

$$Q_t = q_s n_s \cdot \frac{\pi}{6} d^3 \quad (7.11)$$

which are actually contained in the target with ion density n_s and mean charge q_s . Here a transition is expected where all electrons are pushed out of the spherical target expressed by $Q_t = Q_K$. Using Eqs. (7.8) and (7.11) the absorbed laser energy for this transition reads

$$\eta E_L^t = \frac{e^2}{36\epsilon_0} q_s^2 n_s^2 d^5 \approx 0.8 \cdot d^5 \frac{\text{J}}{\mu\text{m}^5} \quad (7.12)$$

where the typical target electron density $q_s n_s \approx 10^{23}/\text{cm}^3$ was used and d is the diameter of the target in μm . Note, that for a sphere of $q_s = 16$ -fold ionized gold ions the electron density $q_s n_s = 10^{24}/\text{cm}^3$ is even a factor of ten higher than assumed in Eq. (7.12) resulting in a laser transition energy E_L enhanced by a factor of 100.

The maximum ion energy for the case where all electrons are pushed out of the sphere is obtained by replacing ηE_L in Eq. (7.10) by ηE_L^t (Eq. (7.12)):

$$E_{i,\infty}^K = q_i q_s n_s d^2 \frac{e^2}{12\epsilon_0} \approx q_i d^2 \cdot 150 \frac{\text{MeV}}{\mu\text{m}^2} \quad (7.13)$$

where again $q_s n_s = 10^{23}/\text{cm}^3$ was used and d is the target diameter in μm . Note, that this equation (7.13) would suggest that large target diameter are preferable for higher ion energies. This is not true because the absorbed laser energy which is needed to push all electrons out of the target (Eq. (7.12)) is proportional to d^5 .

According to Eq. (7.10) it is possible to achieve 150 MeV protons from a spherical target with $1 \mu\text{m}$ diameter and 1 J of absorbed laser energy. The target could

consist of a gold sphere with a thin (some monolayers) carbon or hydrogen layer which then would be accelerated in a mono-energetic bunch due to the repulsion of the charged target (Sec. 7.3.1).

As mentioned, for $E_L > E_L^t$ (Eq. (7.12)) all electrons are pushed out of the target which also leads to a field inside the target. In this case the electrons are also pushed forward by the laser pressure so one can imagine that the whole target may be accelerated in laser direction. This effect was predicted by Wei *et al.* [92] for PW-laser pulses and small targets with rest masses of the order of the absorbed laser pulse energy.

7.3.3 The transition to the laser-piston regime

The ion acceleration was understood in the framework of the electric field of the surface charge built up by Q electrons which are permanently outside the foil. The surface charge has radii of the order of $10\ \mu\text{m}$ and is shielded by the huge amount of electrons in the wide target foil ($\approx 1 - 2\ \text{mm}$). One could imagine that this picture breaks down when the target is transversely restricted or the Q electrons are produced faster than the response of the target electrons. Both of these modifications would change the physical picture, i.e., the target can not stay neutral inside. This will happen when the number of electrons Q pushed out of the target by the laser pulse (Eq. (3.16)) equals the number of electrons

$$Q_t = q_s n_s \pi B^2 d (\approx 10^{14}) \quad (7.14)$$

provided by the target with electron density $q_s n_s \approx 10^{23}/\text{cm}^3$ within the radius B and foil thickness d . The condition for the transition to the new regime, where all electrons are pushed out of the foil then reads

$$\eta I_L^{pd} = q_s^2 n_s^2 d^2 \frac{e^2 c}{4\epsilon_0} \approx 2.2 \cdot 10^{23} \text{ W/cm}^2 \quad (7.15)$$

where it was assumed that $B \approx r_L$ which is true for thin targets ($d \approx 1\ \mu\text{m}$). For such high intensities the conversion efficiency η of laser energy into electron energy is expected to be at least 0.5. From $I_L^{pd} = 1/2 \cdot \epsilon_0 c F_L^{pd}$ one derives

$$F_L^{pd} = n_s d \frac{e}{\sqrt{2\epsilon_0}} \approx 1.3 \cdot 10^{15} \text{ V/m} \quad (7.16)$$

which is the charge separation field when all electrons of the foil are displaced by the target thickness d . Thus, I_L^{pd} may be identified with the threshold intensity for the transition to the pressure dominated or laser-piston regime as discussed by Esirkepov *et al.* [87].

In the work cited it was shown that the huge charge separation field can accelerate ions close to the velocity of light within one cycle of the laser pulse (≈ 3 fs). A small part from the foil is teared off and starts to fly with velocities close to c . The rest of the laser pulse is then reflected from the accelerated plasma bunch which acts as a relativistically moving mirror. Assuming a reflectivity of 1 it can be seen from simple energy conservation considerations that the energy of the bunch (mirror)

$$E_b = \left(1 - \frac{1}{4\gamma_b}\right) E_L. \quad (7.17)$$

is proportional to the laser pulse energy E_L once the foil moves relativistically ($\gamma_b > 2$). At this stage the plasma bunch is accelerated due to the light pressure of the laser pulse. As discussed by Esirkepov *et al.* ion energies of up to 100 GeV/u could be achieved with present-day technologies.

7.4 Application of laser accelerated ion beams

Laser accelerated ion beams are considered for a wide range of applications such as fast ignition for inertial confinement fusion [30], fast-ion beam injection to conventional accelerators [93], proton imaging [28] and maybe the most interesting although challenging field of ion therapy [94, 95]. Ion beams in radiotherapy and oncology provides several advantages. Unlike electrons and gamma- or x-rays ions are stopped in the well defined Bragg peak and are not strongly scattered transversely. Thus, the energy of the ions can be directed very accurately to the tumor which should be destroyed without damaging the surrounding tissue. For that also ion beams with a high quality, i.e., small energy spread $\Delta E/E$ are essential. In ion cancer therapy $\Delta E/E$ must be at least of the order of 2% to prevent damage in the healthy tissue surrounding the tumor. In order to reach tumorous tissue in a depth of up to 15 cm depth proton energies of approximately 170 MeV or 270 MeV/u carbon beams are necessary. For the exposure of a tumor a dose of $10^6 - 10^8$ ions per second is appropriate. The relevant volume is divided into up to 50000 pixels which are sequentially irradiated with 3% accuracy in the number of ions per pixel. The MHz repetition rate in conventional accelerators ensures the smooth distribution of the dose.

Currently several hospitals start patient treatment on a daily basis where the ions with the required parameters are delivered by particle accelerators such as synchrotrons, cyclotrons, and linear accelerators [96].

The biggest advantage in using laser-based ion accelerators is seen in the achievable compactness of the system. Although the outstanding characteristics in terms of transversal and longitudinal emittance of laser accelerated ion beams [27] are encouraging, their main drawback arises from the very broad energy distribution which mainly results from the radial and longitudinal variation of the electric field. If the proton layer would be confined to a thin layer with a transversal extension of the order of the focal spot size all ions are accelerated in the same field which obviously results in a low energy spread as discussed by Esirkepov *et al.* [79]. The experimental evidence of this method was supplied by Schwörer *et al.* [40] where 1.2 MeV protons with an energy spread of $\Delta E/E = 25\%$ were observed from a laser irradiated titanium foil with a $20\ \mu\text{m}$ wide and $0.5\ \mu\text{m}$ thick proton rich dot on its rear side. For protons the essential energy range of 140 – 200 MeV will be achieved with PW-class lasers. Laser accelerated ion bunches can contain up to 10^8 particles per bunch so one could hope that a repetition rate of 1 Hz is sufficient. This is not true because it is necessary to distribute the ions smoothly over the tumor so a higher repetition rate and lower ion numbers per bunch are essential. The treatment of a tumorous volume consisting of 30000 pixels with 10 pulses per pixel and a repetition rate of 1 kHz requires 5 minutes and is acceptable. The dose accuracy of 10 % can only be improved to 1 % with a 10 kHz repetition rate and 10 times less ions per bunch.

Although in principle the dot targets described by Schwörer *et al.* [40] provide the possibility of creating mono-energetic ion beams most of the accelerating electric field remains unused. This might be overcome by using small heavy targets such as a gold sphere of μm or even sub- μm size which would act as a reservoir of electrons and provides the substrate which forces the laser accelerated electrons to recirculate on the scale of the size of the sphere. Thus, the acceleration field will take a mean value which is constant around the sphere since the electrons are confined in a three dimensional manner. In this scheme the duration of the acceleration is not restricted by the laser pulse duration anymore. Moreover, in order to build up the acceleration field very fast, i.e., before the first ions start to move, short laser pulses are even preferable (PFS). On the surface of the sphere one would deposit a thin layer of carbon or proton atoms which would be accelerated in the electric field. Due to their much larger charge-to-mass ratios as compared to the gold ions the ions from the layer would detach and form a mono-energetic ion bunch [79]. The number of ions per bunch may be selected by the thickness of the layer. Still, the ions would be accelerated mainly in target normal direction, i.e., isotropically in case of the sphere. However, once the proof of principle for this scheme is done one could think of micro-structuring the target in order to orient

the ion beam to a certain direction.

Apart from the proton imaging technique all other proposed applications of laser accelerated ion beams are still hypothetical. The understanding of the underlying processes proceeded considerably during the last years and led to good models which could be proofed to be reliable. Presently, the realization of the proposed applications seems to be a question of the further development in high-intensity laser technics.

Appendix A

Charge transfer

The charge states of ions change while passing through matter, i.e., the residual gas in the target chamber. The responsible electron transfer cross sections σ are strongly dependent on the energy of the projectile, and can reach values as high as 10^{-15} cm^2 [82]. The typical pressure in the interaction chamber is below 10^{-4} mbar corresponding to a particle density $n = 2.7 \cdot 10^{12} \text{ cm}^{-3}$, so that the mean free path length $l = (n \cdot \sigma)^{-1}$ for electron transfer exceeds 4 m. The ions usually travel around one meter from the target to the detector. This means electron transfer reactions may not be neglected under the considered vacuum conditions.

The charge state distribution of ions passing through a medium of density $n(x)$ is obtained by integrating the set of coupled differential equations

$$\frac{d}{dx} \frac{dN_i}{dE} = \sum_j n(x) \left(\sigma_{ji}(E) \frac{dN_j}{dE}(x, E) - \sigma_{ij}(E) \frac{dN_i}{dE}(x, E) \right) \quad (\text{A.1})$$

over the propagation distance, starting with the initial ion energy distribution $\left. \frac{dN_i}{dE} \right|_{x=0}$. The first term describes the population and the second term describes the depopulation of the i th charge state with the energy dependent electron transfer cross sections $\sigma_{ij}(E)$. This set of linear differential equations is valid as long as stopping processes can be neglected and no higher order transitions occur. If the travelling length of the projectile is much longer than the mean free path length l_{mfp} for electron transfer, the resulting charge state distribution corresponds to an equilibrium distribution. For this case, the population of the charge states is described by energy dependent mean charge states and charge state distribution widths, which were extensively measured. These values are tabulated for a variety of projectile ions and target materials [80] or can be calculated using semi-empirical formulas [83, 84]. Referring to equation A.1, this equilibrium scenario is expressed

by setting $\frac{1}{dx} \frac{dN_i}{dE}$ to zero, and the final charge state distribution does not longer depend on the initial charge state distribution. If the equilibrium conditions are not fulfilled, the set of linear differential equations (A.1) must be solved, which implies the knowledge of the electron transfer cross sections. For oxygen ions passing nitrogen or other gases, these values were measured by MacDonald *et al.* [82] for the relevant energy range.

Bibliography

- [1] * ¹ **J. Schreiber**, F. Bell, F. Grüner, U. Schramm, M. Geissler, M. Schnürer, S. Ter-Avetisyan, B.M. Hegelich, J. Cobble, E. Brambrink, J. Fuchs, P. Audebert and D. Habs, *An Analytical Model for Ion Acceleration by High-Intensity Laser Pulses*, Phys. Rev. Lett. **97**, 045005 (2006).
- [2] * **J. Schreiber**, S. Ter-Avetisyan, E. Risse, M.P. Kalachnikov, P.V. Nickles, W. Sandner, U. Schramm, D. Habs, J. Witte and M. Schnürer, *Pointing of laser-accelerated proton beams*, Phys. Plasmas **13**, 033111 (2006).
- [3] E. Brambrink, **J. Schreiber**, T. Schlegel, P. Audebert, J. Cobble, J. Fuchs, M. Hegelich and M. Roth, *Transverse Characteristics of Short-Pulse Laser-Produced Ion Beams: A Study of the Acceleration Dynamics*, Phys. Rev. Lett. **96**, 154801 (2006).
- [4] * B.M. Hegelich, B.J. Albright, J. Cobble, K. Flippo, S. Letzring, M. Paffett, H. Ruhl, **J. Schreiber**, R.K. Schulze and J.C. Fernández, *Laser acceleration of quasi-monoenergetic MeV ion beams*, Nature **439**, 441 (2006).
- [5] J. Fuchs, P. Antici, E. D’Humières, E. Lefebvre, M. Borghesi, E. Brambrink, C.A. Cecchetti, M. Kaluza, V. Malka, M. Manclossi, S. Meyroneinc, P. Mora, **J. Schreiber**, T. Toncian, H. Pépin and P. Audebert, *Laser-driven proton scaling laws and new paths towards energy increase*, Nature Phys. **2**, 48 (2006).
- [6] J.J. Honrubia, M. Kaluza, **J. Schreiber**, G.D. Tsakiris and J. Meyer ter Vehn, *Laser-driven fast-electron transport in preheated foil targets*, Phys. Plasmas **12**, 052708 (2005).
- [7] J.C. Fernández, B.M. Hegelich, J.A. Cobble, K.A. Flippo, S.A. Letzring, R.P. Johnson, D.C. Gautier, T. Shiamada, G.A. Kyrala, Y.Q. Wang, C.J. Wettenland and **J. Schreiber**, *Laser-ablation treatment of short-pulse laser targets*:

¹Publications marked with * are attached to this work

- Towards an experimental program on energetic-ion interactions with dense plasmas*, Laser & Part. Beams **23**, 267 (2005).
- [8] B.M. Hegelich, B. Albright, P. Audebert, A. Blazevic, E. Brambrink, J. Cobble, T. Cowan, J. Fuchs, J.C. Gauthier, C. Gautier, M. Geissel, D. Habs, R. Johnson, S. Karsch, A. Kemp, S. Letzring, M. Roth, U. Schramm, **J. Schreiber**, K.J. Witte and J.C. Fernández, *Spectral properties of laser-accelerated mid-Z MeV/u ion beams*, Phys. Plasmas **12**, 056314 (2005).
- [9] M. Roth, E. Brambrink, P. Audebert, A. Blazevic, R. Clarke, J. Cobble, T.E. Cowan, J. Fernández, J. Fuchs, M. Geissel, D. Habs, M. Hegelich, S. Karsch, K. Ledingham, D. Neely, H. Ruhl, T. Schlegel and **J. Schreiber**, *Laser accelerated ions and electron transport in ultra-intense laser matter interaction*, Laser & Part. Beams **23**, 95 (2005).
- [10] J. Fuchs, Y. Sentoku, S. Karsch, J. Cobble, P. Audebert, A. Kemp, A. Nikroo, P. Antici, E. Brambrink, A. Blazevic, E.M. Campbell, J.C. Fernández, J.-C. Gauthier, M. Geissel, M. Hegelich, H. Pépin, H. Popescu, N. Renard-LeGalloudec, M. Roth, **J. Schreiber**, R. Stephens and T.E. Cowan, *Comparison of Laser Ion Acceleration from the Front and Rear Surfaces of Thin Foils*, Phys. Rev. Lett. **94**, 045004 (2005).
- [11] * M. Kaluza, **J. Schreiber**, M.I.K. Santala, G.D. Tsakiris, K. Eidmann, J. Meyer ter Vehn and K.J. Witte, *Influence of the Laser Prepulse on Proton Acceleration in Thin-Foil Experiments*, Phys. Rev. Lett. **93**, 045003 (2004).
- [12] * **J. Schreiber**, M. Kaluza, F. Grüner, U. Schramm, B.M. Hegelich, J. Cobble, M. Geissler, E. Brambrink, J. Fuchs, P. Audebert, D. Habs and K. Witte, *Source-size measurements and charge distributions of ions accelerated from thin foils irradiated by high-intensity laser pulses*, Appl. Phys. B **79**, 1041 (2004).
- [13] T.H. Maiman, *Stimulated Optical Radiation in Ruby*, Nature **187**, 493 (1960).
- [14] S.J. Gitomer, R.D. Jones, F. Begay, A.W. Ehler, J.F. Kephart and R. Kristal, *Fast Ions and hot electrons in the laser-plasma interaction*, Phys. Fluids **29**, 2679 (1986).
- [15] J.E. Crow, P.L. Auer and J.E. Allen, *Plasma Expansion into Vacuum*, J. Plasma Phys. **14**, 65 (1975).
- [16] D. Strickland and G. Mourou, *Compression of amplified chirped optical pulses*, Optics Communications **56**, 219 (1985).

- [17] E.B. Treacy, *Optical pulse compression with diffraction gratings*, IEEE J. of Quantum Electronics **QE-5**, 454 (1969).
- [18] T. Tajima and G. Mourou, *Zettawatt-exawatt lasers and their applications in ultrastrong-field physics*, Phys. Rev. ST AB **5**, 031301 (2002).
- [19] G.A. Mourou, T. Tajima and S.V. Bulanov, *Optics in the relativistic regime*, Rev. Mod. Phys. **78**, 309 (2006).
- [20] A.P. Fews, P.A. Norreys, F.N. Beg, A.R. Bell, A.E. Dangor, C.N. Danson, P. Lee and S.J. Rose, *Plasma ion emission from high intensity picosecond laser pulse interaction with solid targets*, Phys. Rev. Lett. **73**, 1801 (1994).
- [21] A. Maksimchuk, S. Gu, K. Flippo, D. Umstadter and V.Yu. Bychenkov, *Forward Ion Acceleration in Thin Films Driven by a High-Intensity Laser*, Phys. Rev. Lett. **84**, 4108 (2000).
- [22] E.L. Clark, K. Krushelnick, J.R. Davies, M. Zepf, M. Tatarakis, F.N. Beg, A. Machacek, P.A. Norreys, M.I.K. Santala, I. Watts and A.E. Dangor, *Measurements of Energetic Proton Transport through Magnetized Plasma from Intense Laser Interactions with Solids*, Phys. Rev. Lett. **84**, 670 (2000).
- [23] R.A. Snavely, M.H. Key, S.P. Hatchett, T.E. Cowan, M. Roth, T.W. Phillips, M.A. Stoyer, E.A. Henry, T.C. Sangster, M.S. Singh, S.C. Wilks, A. MacKinnon, A. Offenberger, D.M. Pennington, K. Yasuike, A.B. Langdon, B.F. Lasinski, J. Johnson, M.D. Perry and E.M. Campbell, *Intense High-Energy Proton Beams from Petawatt-Laser Irradiation of Solids*, Phys. Rev. Lett. **85**, 2945 (2000).
- [24] S.P. Hatchett, C.G. Brown, T.E. Cowan, E.A. Henry, J.S. Johnson, M.H. Key, J.A. Koch, A.B. Langdon, B.F. Lasinski, R.W. Lee, A.J. Mackinnon, D.M. Pennington, M.D. Perry, T.W. Phillips, M. Roth, T.C. Sangster, M.S. Singh, R.A. Snavely, M.A. Stoyer, S.C. Wilks and K. Yasuike, *Electron, photon, and ion beams from the relativistic interaction of Petawatt laser pulses with solid targets*, Phys. Plasmas **7**, 2076 (2000).
- [25] A.J. Mackinnon, M. Borghesi, S. Hatchett, M.H. Key, P.K. Patel, H. Campbell, A. Schiavi, R. Snavely, S.C. Wilks and O. Willi, *Effect of Plasma Scale Length on Multi-MeV Proton Production by Intense Laser Pulses*, Phys. Rev. Lett. **86**, 1768 (2001).
- [26] M. Roth, M. Allen, P. Audebert, A. Blazevic, E. Brambrink, T.E. Cowan, J. Fuchs, J.-C. Gauthier, M. Geißel, M. Hegelich, S. Karsch, J. Meyer ter

- Vehn, H. Ruhl, T. Schlegel and R.B. Stephens, *The generation of high-quality, intense ion beams by ultra-intense lasers*, Plasma Phys. Control. Fusion **44**, B99 (2002).
- [27] T.E. Cowan, J. Fuchs, H. Ruhl, A. Kemp, P. Audebert, M. Roth, R. Stephens, I. Barton, A. Blazevic, E. Brambrink, J. Cobble, J. Feréndez, J.-C. Gauthier, M. Geissel, M. Hegelich, J. Kaae, S. Karsch, G.P. Le Sage, S. Letzring, M. Manclossi, S. Meyroneinc, A. Newkirk, H. Pépin and N. Renard-LeGalloudec, *Ultralow Emittance, Multi-MeV Proton Beams from a Laser Virtual-Cathode Plasma Accelerator*, Phys. Rev. Lett. **92**, 204801 (2004).
- [28] M. Borghesi, A.J. Mackinnon, D.H. Campbell, D.G. Hicks, S. Kar, P.K. Patel, D. Price, L. Romagnani, A. Schiavi and O. Willi, *Multi-MeV Proton Source Investigations in Ultraintense Laser-Foil Interactions*, Phys. Rev. Lett. **92**, 055003 (2004).
- [29] H. Haseroth and H. Hora, *Physical mechanism leading to high currents of highly charged ions in laser-driven ion sources*, Laser & particle beams **14**, 393 (1996).
- [30] M. Roth, T.E. Cowan, M.H. Key, S.P. Hatchett, C. Brown, W. Fountain, J. Johnson, D.M. Pennington, R.A. Snavely, S.C. Wilks, K. Yasuike, H. Ruhl, F. Pegoraro, S.V. Bulanov, E.M. Campbell, M.D. Perry and H. Powell, *Fast Ignition by Intense Laser-Accelerated Proton Beams*, Phys. Rev. Lett. **86**, 436 (2001).
- [31] V. Malka, *Practicability of protontherapy using compact laser systems*, Med. Phys. **31**, 1587 (2004).
- [32] S.V. Bulanov, H. Daido, T.Zh. Esirkepov, V.S. Khoroshkov, J. Koga, K. Nishihara, F. Pegoraro, T. Tajima and M. Yamagiwa, *Feasibility of using laser ion accelerators in proton therapy*, The Physics of Ionized Gases: 22nd Summer School and International Symposium on the Physics of Ionized Gases, ed. by L. Hadžievski, T. Grozdanov, and N. Bibic, AIP Conf. Proc. No. 740 (AIP, New York) 414 (2004).
- [33] M. Borghesi, S. Bulanov, D.H. Campbell, R.J. Clark, T.Zh. Esirkepov, M. Galimberti, L.A. Gizzi, A.J. MacKinnon, N.M. Naumova, F. Pegoraro, H. Ruhl, A. Schiavi and O. Willi, *Macroscopic Evidence of Soliton Formation in Multiterawatt Laser-Plasma Interaction*, Phys. Rev. Lett. **88**, 135002 (2002).

- [34] L. Romagnani, J. Fuchs, M. Borghesi, P. Antici, P. Audebert, F. Ceccherini, T. Cowan, T. Grismayer, S. Kar, A. Macchi, P. Mora, G. Pretzler, A. Schiavi, T. Toncian and O. Willi, *Dynamics of Electric Fields Driving the Laser Acceleration of Multi-MeV Protons*, Phys. Rev. Lett. **95**, 195001 (2005).
- [35] J. Fuchs, T.E. Cowan, P. Audebert, H. Ruhl, L. Gremillet, A. Kemp, M. Allen, A. Blazevic, J.-C. Gauthier, M. Geissel, M. Hegelich, S. Karsch, P. Parks, M. Roth, Y. Sentoku, R. Stephens and E.M. Campbell, *Spatial Uniformity of Laser-Accelerated Ultrahigh-Current MeV Electron Propagation in Metals and Insulators*, Phys. Rev. Lett. **91**, 255002 (2003).
- [36] M. Hegelich, Dissertation, LMU München, 2002.
- [37] M. Hegelich, S. Karsch, G. Pretzler, D. Habs, K. Witte, W. Guenther, M. Allen, A. Blazevic, J. Fuchs, J.-C. Gauthier, M. Geissel, P. Audebert, T.E. Cowan, and M. Roth, *MeV Ion Jets from Short-Pulse-Laser Interaction with Thin Foils*, Phys. Rev. Lett. **89**, 085002 (2002).
- [38] P. McKenna, K.W.D. Ledingham, J.M. Yang, L. Robson, T. McCanny, S. Shimizu, R.J. Clarke, D. Neely, K. Spohr, R. Chapman, R.P. Singhal, K. Krushelnick, M.S. Wei and P.A. Norreys, *Characterization of proton and heavier ion acceleration in ultrahigh-intensity laser interactions with heated target foils*, Phys. Rev. E **70**, 036405 (2004).
- [39] A.J. Mackinnon, Sentoku, P.K. Patel, D.W. Price, S. Hatchett, M.H. Key, C. Andersen, R. Snavely and R.R. Freeman, *Enhancement of Proton Acceleration by Hot-Electron Recirculation in Thin Foils Irradiated by Ultraintense Laser Pulses*, Phys. Rev. Lett. **88**, 215006 (2002).
- [40] H. Schwoerer, S. Pfoth, O. Jäckel, K.-U. Amthor, B. Liesfeld, W. Ziegler, R. Sauerbrey, K.W.D. Ledingham and T. Esirkepov, *Laser-plasma acceleration of quasi-monoenergetic protons from microstructured targets*, Nature **439**, 445 (2006).
- [41] A. Pukhov, *Three-dimensional simulations of ion acceleration from a foil irradiated by a short-pulse laser*, Phys. Rev. Lett. **86**, 3562 (2001).
- [42] S.C. Wilks, A.B. Langdon, T.E. Cowan, M. Roth, M. Singh, S. Hatchett, M.H. Key, D. Pennington, A. MacKinnon and R.A. Snavely, *Energetic proton generation in ultra-intense laser-solid interactions*, Phys. Plasmas **8**, 542 (2001).

- [43] D.S. Dorozhkina and V.E. Semenov, *Exact Solution of Vlasov Equations for Quasineutral Expansion of Plasma Bunch into Vacuum*, Phys. Rev. Lett. **81**, 2691 (1998).
- [44] V.F. Kovalev and V.Yu. Bychenkov, *Analytic Solutions to the Vlasov Equations for Expanding Plasmas*, Phys. Rev. Lett. **90**, 185004 (2003).
- [45] P. Mora, *Plasma expansion into vacuum*, Phys. Rev. Lett. **90**, 185002 (2003).
- [46] P. Mora and T.M. Antonsen, *Kinetic modeling of intense, short laser pulses propagating in tenuous plasmas*, Phys. Plasmas **4**, 217 (1997).
- [47] B. Quesnel and P. Mora, *Theory and simulation of the interaction of ultraintense laser pulses with electrons in vacuum*, Phys. Rev. E **58**, 3719 (1998).
- [48] S.C. Wilks, W.L. Kruer, M. Tabak and A.B. Langdon, *Absorption of Ultra-Intense Laser Pulses*, Phys. Rev. Lett. **69**, 1383 (1992).
- [49] T. Tajima and J.M. Dawson, *Laser Electron Accelerator*, Phys. Rev. Lett. **43**, 267 (1992).
- [50] S.P.D. Mangles, C.D. Murphy, Z. Najmudin, A.G.R. Thomas, J.L. Collier, A.E. Dangor, E.J. Divall, P.S. Foster, J.G. Gallacher, C.J. Hooker, D.A. Jaroszynski, A.J. Langley, W.B. Mori, P.A. Norreys, F.S. Tsung, R. Viskup, B.R. Walton and K. Krushelnick, *Monoenergetic beams of relativistic electrons from intense laserplasma interactions*, Nature **431**, 535 (2004).
- [51] C.G.R. Geddes, Cs. Toth, J. van Tilborg, E. Esarey, C.B. Schroeder, D. Bruhwiler, C. Nieter, J. Cary and W.P. Leemans, *High-quality electron beams from a laser wakefield accelerator using plasma-channel guiding*, Nature **431**, 538 (2004).
- [52] J. Faure, Y. Glinec, A. Pukhov, S. Kiselev, S. Gordienko, E. Lefebvre, J.-P. Rousseau, F. Burgy and V. Malka, *A laserplasma accelerator producing monoenergetic electron beams*, Nature **431**, 541 (2004).
- [53] F. Brunel, *Not-So-Resonant, Resonant Absorption*, Phys. Rev. Lett. **59**, 52 (1987).
- [54] A.V. Gurevich, L.V. Pariiska and L.P. Pitaevsk, *Self-similar motion of rarefied plasma*, Sov. Phys. JETP **22**, 449 (1966).
- [55] T. Ditmire, T. Donnelly, A.M. Rubenchik, R.W. Falcone and M.D. Perry, *Interaction of intense laser pulses with atomic clusters*, Phys. Rev. A **53**, 3379 (1996).

- [56] G.S. Sarkisov, G.S. Sarkisov, V.Yu. Bychenkov, V.N. Novikov, V.T. Tikhonchuk, P.N. Lebedev, A. Maksimchuk, S.-Y. Chen, R. Wagner, G. Mourou and D. Umstadter, *Self-focusing, channel formation, and high-energy ion generation in interaction of an intense short laser pulse with a He jet*, Phys. Rev. E **59**, 7042 (1999).
- [57] A.V. Kuznetsov, T.Zh. Esirkepov, F.F. Kamenets and S.V. Bulanov, *Efficiency of ion acceleration by a relativistically strong laser pulse in an underdense plasma*, Plasma Phys. Rep. **27**, 211 (2001).
- [58] K. Nemoto, A. Maksimchuk, S. Banerjee, K. Flippo, G. Mourou, D. Umstadter and V.Yu. Bychenkov, *Laser-triggered ion acceleration and table top isotope production*, Appl. Phys. Lett. **78**, 595 (2001).
- [59] Y. Sentoku, T.E. Cowan, A. Kemp and H. Ruhl, *High energy proton acceleration in interaction of short laser pulse with dense plasma target*, Phys. Plasmas **10**, 2009 (2003).
- [60] J. Yu, Z. Jiang, J.C. Kieffer and A. Krol, *Hard x-ray emission in high intensity femtosecond lasertarget interaction*, Phys. Plasmas **6**, 1318 (1999).
- [61] M.H. Key, M.D. Cable, T.E. Cowan, K.G. Estabrook, B.A. Hammel, S.P. Hatchett, E.A. Henry, D.E. Hinkel, J.D. Kilkenny, J.A. Koch, W.L. Kruer, A.B. Langdon, B.F. Lasinski, R.W. Lee, B.J. MacGowan, A. MacKinnon, J.D. Moody, M.J. Moran, A.A. Offenberger, D.M. Pennington, M.D. Perry, T.J. Phillips, T.C. Sangster, M.S. Singh, M.A. Stoyer, M. Tabak, G.L. Tietzbohl, M. Tskamoto, K. Wharton and S.C. Wilks, *Hot electron production and heating by hot electrons in fast ignitor research*, Phys. Plasmas **5**, 1966 (1998).
- [62] A. Kemp, R.E.W. Pfund and J. Meyer ter Vehn, *Modeling ultrafast laser-driven ionization dynamics with Monte Carlo collisional particle-in-cell simulations*, Phys. Plasmas **1**, 5648 (2004).
- [63] T. Esirkepov, M. Yamagiwa and T. Tajima, *Laser Ion-Acceleration Scaling Laws Seen in Multiparametric Particle-in-Cell Simulations*, Phys. Rev. Lett. **96**, 105001 (2006).
- [64] P. Gibbon, *Resistively enhanced proton acceleration via high-intensity laser interactions with cold foil targets*, Phys. Rev. E **72**, 026411 (2005).
- [65] S. Karsch, Dissertation, LMU München, 2002.
- [66] Bad Neuheimer Str. 19 D-64289 Darmstadt Germany CST EMStudio™, CST GmbH, , .

- [67] M. Kaluza, Dissertation, TU München, 2004.
- [68] W. Assmann, J.A. Davies, G. Dollinger, J.S. Forster, H. Huber, Th. Reichelt and R. Siegele, *ERDA with very heavy ion beams*, Nucl. Instr. Meth. B **118**, 242 (1996).
- [69] W. Assmann, H. Huber, Ch. Steinhausen, M. Dobler, H. Glückler and A. Weidinger, *Elastic recoil detection analysis with heavy ions*, Nucl. Instr. Meth. B **89**, 131 (1994).
- [70] W. Assmann, P. Hartung, H. Huber, P. Staat, H. Steffens and Ch. Steinhausen, *Setup for materials analysis with heavy ion beams at the Munich MP tandem*, Nucl. Instr. Meth. B **85**, 726 (1994).
- [71] M. Zepf, E.L. Clark, K. Krushelnick, F.N. Beg, C. Escoda, A.E. Dangor, M.I.K. Santala, M. Tatarakis, I.F. Watts, P. A. Norreys, R.J. Clarke, J.R. Davies, M.A. Sinclair, R.D. Edwards, T.J. Goldsack, I. Spencer and K.W.D. Ledingham, *Fast particle generation and energy transport in laser-solid interactions*, Phys. Plasmas **8**, 2323 (2001).
- [72] I. Spencer, K.W.D. Ledingham, P. McKenna, T. McCanny, R.P. Singhal, P.S. Foster, D. Neely, A.J. Langley, E.J. Divall, C.J. Hooker, R.J. Clarke, P.A. Norreys, E.L. Clark, K. Krushelnick and J.R. Davies, *Experimental study of proton emission from 60-fs, 200-mJ high-repetition-rate tabletop-laser pulses interacting with solid targets*, Phys. Rev. E **67**, 046402 (2003).
- [73] S. Fritzler, V. Malka, G. Grillon, J.P. Rousseau, F. Burgy, E. Lefebvre, E. d'Humières, P. McKenna and K.W.D. Ledingham, *Proton beams generated with high-intensity lasers: Applications to medical isotope production*, Appl. Phys. Lett. **83**, 3039 (2003).
- [74] Y. Murakami, Y. Kitagawa, Y. Sentoku, M. Mori, R. Kodama, K.A. Tanaka, K. Mima and T. Yamanaka, *Observation of proton rear emission and possible gigagauss scale magnetic fields from ultra-intense laser illuminated plastic target*, Phys. Plasmas **8**, 4138 (2001).
- [75] T. Esirkepov, M. Yamagiwa and T. Tajima, *Laser Ion-Acceleration Scaling Laws Seen in Multiparametric Particle-in-Cell Simulations*, Phys. Rev. Lett. **96**, 105001 (2006).
- [76] T.A. Carlson, C.W. Nestor, N. Wassermann and J.D. McDowell, *Calculated ionization potentials for multiply charged ions*, At. Data **2**, 63 (1970).

- [77] C. Kittel, *Einführung in die Festkörperphysik* (R. Oldenbourg Verlag, Oldenbourg, 1991).
- [78] W. Brandt, R. Laubert, M. Mourino and A. Schwarzschild, *Dynamic Screening of Projectile Charges in Solids Measured by Target X-ray Emission*, Phys. Rev. Lett. **30**, 358 (1973).
- [79] T.Zh. Esirkepov, S.V. Bulanov, K. Nishihara, T. Tajima, F. Pegoraro, V.S. Khoroshkov, K. Mima, H. Daido, Y. Kato, Y. Kitagawa, K. Nagai and S. Sakabe, *Proposed Double-Layer Target for the Generation of High-Quality Laser-Accelerated Ion Beams*, Phys. Rev. Lett. **89**, 175003 (2002).
- [80] K. Shima, N. Kuno and M. Yamanouchi, *Equilibrium charge fractions of ions of $Z = 4 - 92$ emerging from a carbon foil*, At. Data Nucl. Data Tables **51**, 174 (1992).
- [81] F. Grüner, F. Bell, W. Assmann and M. Schubert, *Integrated Approach to the Electronic Interaction of Swift Heavy Ions with Solids and Gases*, Phys. Rev. Lett. **93**, 213201 (2004).
- [82] J.R. Macdonald and F.W. Martin, *Experimental Electron-Transfer Cross Sections for Collisions of Oxygen Ions in Argon, Nitrogen, and Helium at Energies f 7-40 MeV*, Phys. Rev. A **4**, 1965 (1971).
- [83] G. Schiwietz and P.L. Grande, *Improved charge-state formulas*, Nucl. Instr. & Meth. B **175-177**, 125 (2001).
- [84] R.O. Sayer, *Semi-empirical formulas for heavy-ion stripping data*, Revue de Physique Appliquee 1543 (1977).
- [85] A. Dubietis, R. Butkus and A.P. Piskarskas, *Trends in chirped pulse optical parametric amplification*, IEEE JSTQE **12**, 163 (2006).
- [86] L.O. Silva, M. Marti, J.R. Davies and R.A. Fonseca, *Proton Shock Acceleration in Laser-Plasma Interactions*, Phys. Rev. Lett. **92**, 015002 (2004).
- [87] T. Esirkepov, M. Borghesi, S.V. Bulanov, G. Mourou and T. Tajima, *Highly Efficient Relativistic-Ion Generation in the Laser-Piston Regime*, Phys. Rev. Lett. **92**, 175003 (2004).
- [88] [http : //www.ultra – optics.de/ultraphotonics/polaris_laser.html](http://www.ultra-optics.de/ultraphotonics/polaris_laser.html), .
- [89] [http : //www.attoworld.de/research/PFS_1.html](http://www.attoworld.de/research/PFS_1.html), .
- [90] private communications with D. Habs, *Fundamental physics at ELI*, (2006).

- [91] S. Ter-Avetisyan, M. Schnürer, S. Busch, E. Risse, P.V. Nickles and W. Sandner, *Spectral Dips in Ion Emission Emerging from Ultrashort Laser-Driven Plasmas*, Phys. Rev. Lett. **93**, 155006 (2004).
- [92] Wei Yu, H. Xu, F. He, M.Y. Yu, S. Ishiguro, J. Zhang and A.Y. Wong, *Direct acceleration of solid-density plasma bunch by ultraintense laser*, Phys. Rev. E **72**, 046401 (2005).
- [93] K. Krushelnick, E.L. Clark, R. Allott, F.N. Beg, C.N. Danson, A. Machacek and V. Malka, Z. Najmudin, D. Neely, P.A. Norreys, M.R. Salvati, M.I.K. Santala, M. Tatarakis, I. Watts, M. Zepf and A.E. Dangor, *Ultrahigh-intensity laser-produced plasmas as a compact heavy ion injection source*, IEEE Trans. Plasma Sci. **28**, 1184 (2000).
- [94] S.V. Bulanov and V.S. Khoroshkov, *Feasibility of Using Laser Ion Accelerators in Proton Therapy*, Plasma Phys. Rep. **28**, 453 (2002).
- [95] E. Fourkal, T. Tajima, M. Ding and C.M. Ma, *PIC simulation of laser proton acceleration for radiotherapy*, Med. Phys. **29**, 2788 (2002).
- [96] W.H. Scharf, *Biomedical Particle accelerators* (AIP, Woodbury, NY, 1994).

Analytical Model for Ion Acceleration by High-Intensity Laser Pulses

J. Schreiber,^{1,2,*} F. Bell,¹ F. Grüner,¹ U. Schramm,¹ M. Geissler,² M. Schnürer,³ S. Ter-Avetisyan,³ B. M. Hegelich,⁴
J. Cobble,⁴ E. Brambrink,⁵ J. Fuchs,⁵ P. Audebert,⁵ and D. Habs¹

¹*Department für Physik, Ludwig-Maximilians-Universität München, Garching, Germany*

²*Max-Planck-Institut für Quantenoptik, Garching, Germany*

³*Max-Born-Institut, Berlin, Germany*

⁴*Los Alamos National Laboratory, Los Alamos, New Mexico 87545, USA*

⁵*Laboratoire pour l'Utilisation des Lasers Intenses, UMR 7605, CNRS-CEA-École Polytechnique-Université Paris VI, Palaiseau, France*

(Received 2 May 2006; published 28 July 2006)

We present a general expression for the maximum ion energy observed in experiments with thin foils irradiated by high-intensity laser pulses. The analytical model is based on a radially confined surface charge set up by laser accelerated electrons on the target rear side. The only input parameters are the properties of the laser pulse and the target thickness. The predicted maximum ion energy and the optimal laser pulse duration are supported by dedicated experiments for a broad range of different ions.

DOI: [10.1103/PhysRevLett.97.045005](https://doi.org/10.1103/PhysRevLett.97.045005)

PACS numbers: 52.38.Kd, 41.75.Jv, 52.59.-f

Ion acceleration from high-intensity laser irradiated thin foils has attracted high attention during the past decade. The emitted ion and, in particular, proton pulses contain large particle numbers between 10^{10} and 10^{13} with energies in the MeV [1,2] and multi-MeV range [3–6] and are tightly confined in time (\sim ps) and space (source radius a few μ m). These outstanding characteristics triggered speculations about a wide range of applications in nuclear and medical physics.

The dependence of the ion spectra on the intensity [7,8] and target thickness was investigated experimentally [2,4,9]. Theoretical models are presently based on particle-in-cell simulations (PIC) [10,11] and plasma expansion models (PEM) [12,13], the physical picture of the process being the following. First, electrons are accelerated by the impinging relativistic laser pulse and penetrate the target driven by the Lorentz force. Leaving the target at the rear side, they set up a huge electric field which, in essence, is pointed normal to the target rear surface. Most electrons are forced to turn around and build up a quasistationary electron layer. By this field surface atoms are field ionized and accelerated. This process is called target normal sheath acceleration [10]. In most experiments, a thin layer (\sim nm) of hydrocarbons, water, or oxides contaminates the target surfaces so that ions with the highest charge-to-mass ratio are accelerated predominantly.

In this work, we present a simple analytical model based solely on a radially confined surface charge set up by laser accelerated electrons on the target rear side. The model explains the maximum ion energies observed in a variety of existing experiments as well as in dedicated studies where either the laser pulse duration or the charge-to-mass ratio of the ions was varied.

We assume that N_e electrons are accelerated by the laser and confined in an electron bunch of length $L = c\tau_L$, where τ_L is the laser pulse duration. At the rear side of

the foil, the electrons are transversely spread over a circular area with radius

$$B = r_L + d \tan \theta, \quad (1)$$

where r_L denotes the radius of the laser spot, d the thickness of the target, and θ the half-angle of the electrons traveling through the target. We further imply an exponential electron energy distribution

$$\frac{dN}{dE} = \frac{N_e}{k_B T_e} \exp\left[-\frac{E}{k_B T_e}\right]. \quad (2)$$

When electrons cross the solid-vacuum boundary, they induce a positive surface charge Qe on the conducting rear surface, leading to a surface charge density $Qe/(\pi B^2)$ located at $z = 0$, where z is the electron propagation axis. Solving the Poisson equation for such a charge density distribution, the potential on the z axis is given by

$$-e\Phi(\xi) = E_\infty s(\xi), \quad (3)$$

with $\xi = z/B$ and $s(\xi) = 1 + \xi - (1 + \xi^2)^{1/2}$. Only a few electrons with energies exceeding $E_\infty = Qe^2/(2\pi\epsilon_0 B)$ can escape the rear surface potential, whereas the low energetic electrons reenter the foil. The point $\hat{\xi} = \hat{z}/B$ where electrons with the mean energy $k_B T_e$ turn around is defined by $E_\infty s(\hat{\xi}) \approx E_\infty \hat{\xi} = k_B T_e$, for $\hat{\xi} \ll 1$. This approximation is valid for all experiments to be discussed. Using the definition for E_∞ and the electron density $n_{Q0} = Q/(\pi B^2 \hat{z})$ directly at the surface, one derives

$$\hat{z} = (2\epsilon_0 k_B T_e / n_{Q0} e^2)^{1/2} \equiv \lambda_D, \quad (4)$$

where λ_D is called the hot electron Debye length.

The electron density distribution which is in equilibrium with the surface charge potential Φ then reads

$$n_Q(\xi) = n_{Q0} \exp[-s(\xi)/\xi_D] [1 - \xi/(1 + \xi^2)^{1/2}], \quad (5)$$

where $\xi_D = \lambda_D/B$. Electrons propagate over distance λ_D and back before they reenter the foil. This leads to an equilibrium situation where $Q = 2N_e\lambda_D/L$ electrons are permanently outside the foil, which, in turn, induce Q positive charges in order to maintain charge neutrality also on a scale of λ_D .

From Eq. (3) together with $F = -d\Phi/dz$, we obtain

$$F(\xi) = \frac{k_B T_e}{e\lambda_D} [1 - \xi/(1 + \xi^2)^{1/2}] \quad (6)$$

for the electric field F in the vacuum region outside the foil. Directly at the surface ($\xi = 0$), the electric field agrees with the well-known result $F_0 = k_B T_e/(e\lambda_D)$ from PEM [12,13]. Yet, in contrast to PEM, the potential [Eq. (3)] stays finite for $\xi \rightarrow \infty$ in our model.

In a second step, the potential equation (3) is used to calculate the energy $E_i(\xi)$ an ion with charge $q_i e$ gains between $\xi = 0$ and ξ

$$E_i(\xi) = -q_i e \Phi(\xi) = E_{i,\infty} s(\xi), \quad (7)$$

where $E_{i,\infty} = q_i k_B T_e B/\lambda_D$ defines the energy an ion with charge $q_i e$ could theoretically gain by completely running down the potential well. Here we describe only the most energetic ions which are emitted from the center of the emission zone where the field is highest. Ions starting from outer zones or from deeper surface layers ($z < 0$) will gain less energy and are not treated. The ion energy $E_i(\xi)$ of Eq. (7) results solely from the repulsion due to surface charges Qe ; i.e., the influence of the hot electrons is neglected. This assumption is justified by the following simple picture based on the very different longitudinal spatial distributions of both charge contributions. The positive charge distribution (surface charges) is much more localized than the electron cloud n_Q above the rear surface. The electron center of charge is approximately at a distance λ_D above the surface, and its longitudinal width is of the same order. Thus, the forces of the electrons on an ion at some distance from the surface compensate each other to some degree.

Using the fact that the laser energy $E_L = P_L \tau_L$ is converted with an efficiency η into hot electron energy, i.e., $N_e k_B T_e = \eta E_L$, we derive

$$E_{i,\infty} = q_i 2mc^2 (\eta P_L/P_R)^{1/2}, \quad (8)$$

where $P_R = mc^3/r_e = 8.71$ GW is the relativistic power unit (r_e is the classical electron radius). $E_{i,\infty}$ denotes the maximum possible energy an ion could gain for a certain laser power P_L providing an infinitely long acceleration. For radiation of the order of $1 \mu\text{m}$ wavelength, the efficiency can be approximated by $\eta = 1.2 \times 10^{-15} \cdot I_L^{3/4}$, with I_L in W/cm^2 [14,15] up to a maximum value of $\eta = 0.5$. This maximum conversion efficiency is reached for a laser intensity $I_L = P_L/(\pi r_L^2) = 3.1 \times 10^{19} \text{ W}/\text{cm}^2$, as indicated by Hatchett *et al.* [5] and successfully used by Fuchs *et al.* [16]. Note that the maximum possible ion

energy depends on the square root of the absorbed laser pulse power only [17] and that Eq. (8) shows no explicit dependence on the hot electron temperature T_e .

For experimentally observable maximum ion energies E_m , we need to include the time dependence of the accelerating process, i.e., the stopping of the acceleration after the electron pulse has passed. This is expressed by integrating the equation of motion $d\xi/dt = v(\xi)/B$ with $v(\xi) = (2E_i(\xi)/m_i)^{1/2}$ [Eq. (7)] and m_i as the ion mass; one has

$$\frac{\tau_L}{\tau_0} = X \left(1 + \frac{1}{2} \frac{1}{1-X^2} \right) + \frac{1}{4} \ln \frac{1+X}{1-X}, \quad (9)$$

where $\tau_0 = B/v(\infty)$ and $X = (E_m/E_{i,\infty})^{1/2}$. This Eq. (9) is the main result of our analysis and will be compared with experimental values. The data shown in Fig. 1 are divided into three groups with comparative laser pulse parameters in terms of energy and pulse duration. For the electron propagation angle θ [Eq. (1)], a value of 10° was estimated following Ref. [9] for the 1 J-laser group (ASTRA, ATLAS, MBI, LOA, JANUSP), of 25° as used in Ref. [16] and confirmed by source-size measurements [18] for the 10 J-laser group (GEKKO, LULI, TRIDENT), and of 45° for the 100 J-laser group (NOVAPW, RALVULCAN, RALPW) as indicated by angular resolved x-ray measurements [19]. A precise determination of the source size B seems to be difficult, and

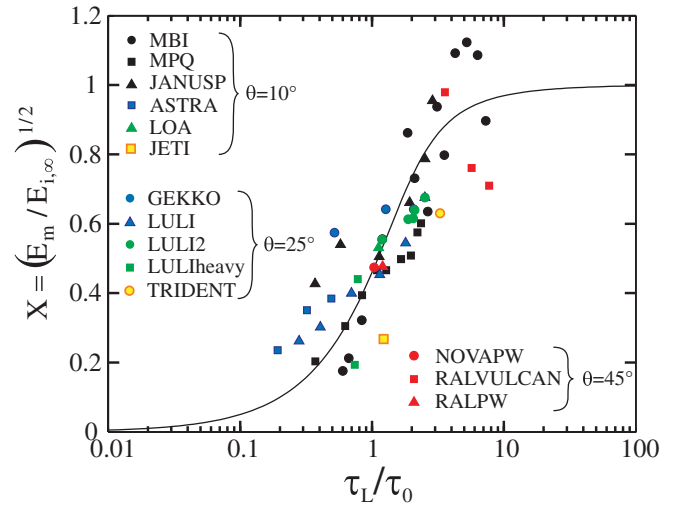


FIG. 1 (color). Comparison of experimental results with theory (solid line). The symbols denote the experimentally obtained maximum ion energies from different laser systems split in three groups with respect to the laser pulse energy: ~ 1 J (MBI, data presented in Fig. 2, MPQ [9], JANUSP [6], ASTRA [24], LOA [25], JETI [26]); ~ 10 J (GEKKO [27], LULI and LULI2 [16], LULIheavy [21], TRIDENT [28]); and ≥ 100 J (RALVULCAN [19], NOVAPW [4]). A single value of θ is assigned to each group. All data refer to protons, except Ref. [21], where also C^{4+} and F^{7+} ions were accelerated, and Ref. [28], where monoenergetic C^{5+} ions were observed.

uncertainty even of a factor of 2 might be realistic. Since B enters the time τ_0 only, such an uncertainty would be reflected in a horizontal displacement of data points in Fig. 1 by the same amount and thus lies within the general scatter of the experimental data. Regarding the range of parameters, the comparison presented in Fig. 1 shows a remarkably good agreement with our theory and thus supports its generality.

Regarding the power dependence of Eq. (8), the final ion energy $E_{i,\infty}$ could be increased for laser systems with constant pulse energy E_L by shortening the pulse duration τ_L . However, short laser pulse duration means a reduction of the acceleration time so that massive ions cannot reach the final energy any more. That this effect is of practical relevance is demonstrated in Fig. 2, where E_m is given as a function of pulse duration for four fixed laser energies E_L (solid lines). It is evident that the highest ion energies E_m^{opt} are obtained for an optimum value τ_L^{opt} . In addition, Fig. 2 reveals that for ion acceleration it is not favorable to build a petawatt laser with pulse duration smaller than about 100 fs for the chosen set of parameters. On the other hand, keeping the laser power P_L constant while increasing E_L and τ_L does not result in an increase of the maximum ion energy once the optimal pulse duration τ_L^{opt} is exceeded. This saturation effect ($E_m = E_{i,\infty}$ for $\tau_L \rightarrow \infty$ visible in the slope of the shaded area in Fig. 1) was also observed in recent PIC simulations [20]. In order to test our approach, an experiment at the 10 Hz-Ti:Sa-laser system of the Max-Born-Institut, Berlin, was performed. The laser energy E_L was 0.7 J within a focal spot of 8 μm (FWHM). Both parameters were kept constant while the laser pulse

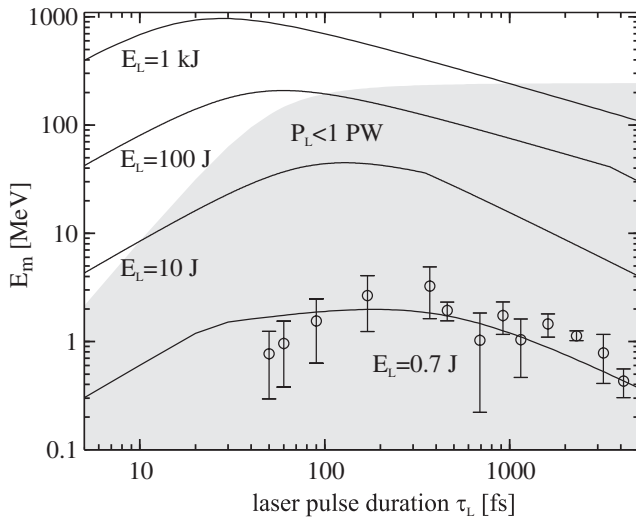


FIG. 2. Dependence of maximum proton energies E_m on the laser pulse duration τ_L for four constant laser energies E_L . The circles represent the experimental data. All four curves (solid lines) correspond to $r_L = 4 \mu\text{m}$, $d = 10 \mu\text{m}$, and $\theta = 10^\circ$. The gray shaded area denotes the region where the laser pulse power P_L is smaller than 1 PW.

duration τ_L was changed between 50 fs and 5 ps. Clearly, the experimental data points in Fig. 2 reveal the existence of an optimal pulse duration τ_L^{opt} of about 250 fs, well in agreement with the prediction of our model.

The left graph in Fig. 3 depicts the optimal laser pulse duration τ_L^{opt} for varying laser energy E_L . The nonmonotonic behavior of τ_L^{opt} results from the explicit intensity dependence of the conversion efficiency. An intensity independent η would result in a strictly decreasing function. The solid line in the right graph in Fig. 3 illustrates the maximum proton energy E_m^{opt} that can be achieved under optimum conditions as a function of the laser pulse power $P_L = E_L/\tau_L^{\text{opt}}$. It shows the same dependence on the laser power as $E_{i,\infty}$ [dotted line, Eq. (8)], a scaling that is corroborated by recent PIC simulations [20].

In a minority of laser ion acceleration experiments, the contaminating hydrogen layer was removed from the target surfaces [21,22], thus allowing for the observation of the acceleration of heavier ions. This immediately implies the question of how the acceleration process depends on the ion charge $q_i e$. Experimentally, this issue has been investigated by Schreiber *et al.* [22]. Not touching the nontrivial problem of describing the charge state population, we assume that all charge states q_i are generated close to the rear surface and are then accelerated in the same electric field. Figure 4 shows the maximum ion energy as a function of charge state for a variety of ions. Since in the experiment cited [22] all ions have been accelerated under identical experimental conditions (i.e., constant E_L , τ_L , r_L , d , and θ), it can be readily seen from Eq. (9) that in this case the scaled ion energy E_m/A_i is a unique function of q_i/A_i , where A_i is the ion nucleon number. The solid curve in Fig. 4 represents this function and shows a fair agreement with experimental data ranging from Li to W ions.

It seems to be indicated to compare our result of Eq. (9) with that of PEM [13,16]

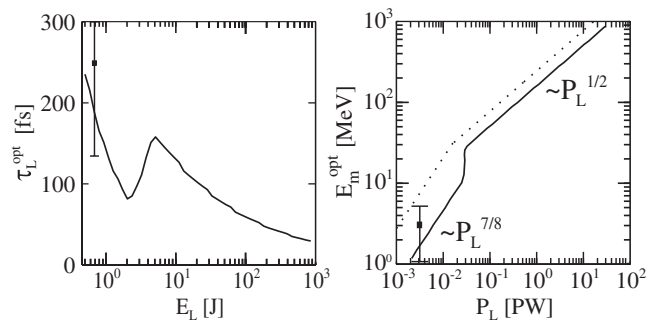


FIG. 3. Dependence of the optimal pulse duration τ_L^{opt} on the laser energy E_L (left). The parameters are identical to those in Fig. 2. The right graph shows the maximum energies E_m^{opt} (solid line) and $E_{i,\infty}$ (dotted line) for optimal laser powers $P_L = E_L/\tau_L^{\text{opt}}$. The data points depict the experimental results derived from Fig. 2.

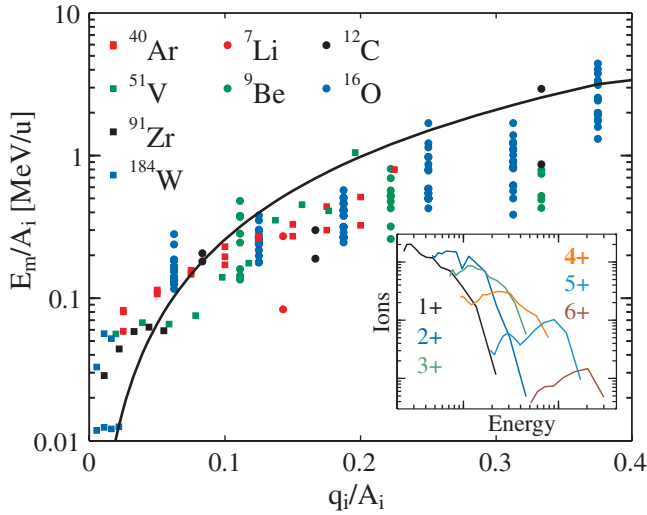


FIG. 4 (color). Scaled maximum ion energies vs charge-to-mass ratios q_i/A_i . The data for fixed ratios result from different laser shots and thus give a measure of the reproducibility from shot to shot. The solid curve is obtained from Eq. (9). For illustration, the inset shows charge state resolved energy spectra in the case of oxygen.

$$E_m^{\text{PEM}} = 2q_i k_B T_e [\ln(\tau + \sqrt{\tau^2 + 1})]^2, \quad (10)$$

where $\tau = 0.43\omega_{pi}\tau_L$. The ion plasma frequency is given by $\omega_{pi} = (n_{i0}(q_i e)^2/\epsilon_0 m_i)^{1/2}$, where n_{i0} is the plasma ion density before expansion. A natural choice of n_{i0} is the atom solid state density of typically $10^{23}/\text{cm}^3$. Combined with an expression for the hot electron temperature T_e given by Wilks *et al.* [23], the obtained maximum ion energies would differ from experimental data by about an order of magnitude. Attempts to circumvent this problem have been made by Kaluza *et al.* [9] and Fuchs *et al.* [16]. However, in our model, no detailed description of the plasma is needed and the relevant characteristic constant is the ballistic time $\tau_0 = B/v(\infty)$, which is independent of the ion density. This seems to be an advantage in cases where ions from surface contaminants are considered. We also note that the maximum ion energy of Eq. (10) diverges logarithmically for large pulse durations τ_L , in contrast to the saturation effect discussed above.

In conclusion, our model describes in good agreement the maximum ion energies observed nowadays in high-

intensity laser experiments with foil targets, including those where different charge-to-mass ratios are present. We have found that the highest intensity is not necessarily suitable for reaching maximum ion energies.

This work was supported by DFG under Contract No. TR18.

*Electronic address: joerg.schreiber@mpq.mpg.de

- [1] A. P. Fews *et al.*, Phys. Rev. Lett. **73**, 1801 (1994).
- [2] A. Maksimchuk, S. Gu, K. Flippo, D. Umstadter, and V. Y. Bychenkov, Phys. Rev. Lett. **84**, 4108 (2000).
- [3] E. L. Clark *et al.*, Phys. Rev. Lett. **84**, 670 (2000).
- [4] R. A. Snavely *et al.*, Phys. Rev. Lett. **85**, 2945 (2000).
- [5] S. P. Hatchett *et al.*, Phys. Plasmas **7**, 2076 (2000).
- [6] A. J. Mackinnon *et al.*, Phys. Rev. Lett. **88**, 215006 (2002).
- [7] F. N. Beg *et al.*, Phys. Plasmas **4**, 447 (1997).
- [8] E. L. Clark *et al.*, Phys. Rev. Lett. **85**, 1654 (2000).
- [9] M. Kaluza *et al.*, Phys. Rev. Lett. **93**, 045003 (2004).
- [10] S. C. Wilks *et al.*, Phys. Plasmas **8**, 542 (2001).
- [11] A. Pukhov, Phys. Rev. Lett. **86**, 3562 (2001).
- [12] J. E. Crow, P. L. Auer, and J. E. Allen, J. Plasma Phys. **14**, 65 (1975).
- [13] P. Mora, Phys. Rev. Lett. **90**, 185002 (2003); Phys. Rev. E **72**, 056401 (2005).
- [14] J. Yu *et al.*, Phys. Plasmas **6**, 1318 (1999).
- [15] M. H. Key *et al.*, Phys. Plasmas **5**, 1966 (1998).
- [16] J. Fuchs *et al.*, Nature Phys. **2**, 48 (2006).
- [17] S. V. Bulanov *et al.*, in *The Physics of Ionized Gases: 22nd Summer School and International Symposium on the Physics of Ionized Gases*, edited by L. Hadžievski, T. Grozdanov, and N. Bibic, AIP Conf. Proc. No. 740 (AIP, New York, 2004), p. 414.
- [18] J. Fuchs *et al.*, Phys. Rev. Lett. **91**, 255002 (2003).
- [19] M. Zepf *et al.*, Phys. Plasmas **8**, 2323 (2001).
- [20] T. Esirkepov, M. Yamagiwa, and T. Tajima, Phys. Rev. Lett. **96**, 105001 (2006).
- [21] M. Hegelich *et al.*, Phys. Rev. Lett. **89**, 085002 (2002).
- [22] J. Schreiber *et al.*, Appl. Phys. B **79**, 1041 (2004).
- [23] S. C. Wilks, W. L. Kruer, M. Tabak, and A. B. Langdon, Phys. Rev. Lett. **69**, 1383 (1992).
- [24] I. Spencer *et al.*, Phys. Rev. E **67**, 046402 (2003).
- [25] S. Fritzler *et al.*, Appl. Phys. Lett. **83**, 3039 (2003).
- [26] H. Schwoerer *et al.*, Nature (London) **439**, 445 (2006).
- [27] Y. Murakami *et al.*, Phys. Plasmas **8**, 4138 (2001).
- [28] B. M. Hegelich *et al.*, Nature (London) **439**, 441 (2006).
- [29] P. McKenna *et al.*, Phys. Rev. E **70**, 036405 (2004).

Pointing of laser-accelerated proton beams

J. Schreiber

*MPI für Quantenoptik, Hans-Kopfermann-Str. 1, D 85748 Garching, Germany
and LMU Muenchen, Am Coulombwall 1, D 85748, Garching, Germany*

S. Ter-Avetisyan, E. Risse, M. P. Kalachnikov, and P. V. Nickles

Max Born Institut, Max Born Strasse 2a, D 12489 Berlin, Germany

W. Sandner

*Max Born Institut, Max Born Strasse 2a, D 12489 Berlin, Germany
and TU Berlin, Straße des 17. Juni 135, D 10623 Berlin, Germany*

U. Schramm and D. Habs

LMU Muenchen, Am Coulombwall 1, D 85748, Garching, Germany

J. Witte

MPI für Quantenoptik, Hans-Kopfermann-Str. 1, D 85748 Garching, Germany

M. Schnürer

Max Born Institut, Max Born Strasse 2a, D 12489 Berlin, Germany

(Received 10 October 2005; accepted 10 February 2006; published online 31 March 2006)

Small fluctuations in the acceleration sheath change the pointing of a proton beam accelerated from the rear side of a laser irradiated thin aluminum foil. The proton acceleration was produced with 40 fs pulses of a Ti:sapphire laser at an intensity of approximately 10^{19} W/cm². This observation has been made with a high spatial resolution Thomson spectrometer. The proton beam pointing has appeared stable in the energy range between the high energy cutoff (3 MeV) and 50% of this value. Deviations of the beam position at lower energies changes in a range of 0–3 mrad. The recorded pictures show wiggled and continuous proton traces which imply a release of the proton beam from the acceleration zone with a velocity chirp. © 2006 American Institute of Physics.

[DOI: [10.1063/1.2181978](https://doi.org/10.1063/1.2181978)]

I. INTRODUCTION

The development of short pulse proton radiography needs such beam characteristics as the energy spectrum, beam emittance, pulse duration, and the peak and average particle fluxes. High intensity laser produced proton beams cover kinetic energies between several and tens of mega-electron volts when laser peak powers between some tens of TeraWatt (TW) and PetaWatt (PW) are used (see, e.g., Refs. 1–11). Protons with these energies have already been used in the first proof-of-principle experiments to trace strong electric and magnetic fields in laser produced dense plasmas as given in Ref. 12. Quantitative knowledge of these fields is an essential prerequisite for a better understanding of energy transport and energy conversion triggered by laser fields of relativistic strength. Release of the energetic ions from the targets at very intense laser irradiation is a consequence of these processes. Recently Cowan *et al.*¹³ and Borghesi *et al.*¹⁴ reported very low emittance values of $\sim 10^{-3}$ and $\sim 10^{-1}$ mm mrad, respectively, for laser accelerated proton beams. This beam feature is superior for radiographic image generation.

In this work we analyze the beam pointing and the divergence of a beamlet of protons emitted from thin aluminum foils. The results presented demonstrate for the first time a high angular resolution of proton trajectories in dependence on the proton energy. The latter allows

conclusions regarding not only the angular and spatial emission of the source but also the history of its temporal evolution.

II. EXPERIMENT

The experiments have been carried out with a 40 fs Ti:sapphire laser.¹⁵ The laser pulses with energy of up to 700 mJ were focused with an $f/2.5$ off-axis parabolic mirror to intensities approximately 2×10^{19} W/cm². The latter was estimated from the energy content in a focal area with a diameter approximately 10 μ m. Imaging of the focal spot with a microscope objective at micrometer resolution and a 12 bit dynamic range for the intensity resulted in a Gaussian-like smooth distribution. Aluminum foils with a thickness of 10–13 μ m were used in the experiment. The measurements of the ion emission spectrum were carried out with an absolutely calibrated Thomson parabola spectrometer. Typically, a magnetic field of approximately 0.27 T and electric fields of 2–6 kV/cm have been applied. The ions were detected by a multichannel plate (MCP) detector with a diameter of 40 mm coupled to a phosphor screen imaged on a cooled chip of a charge-coupled device (CCD) camera. The single particle response of the whole detection and registration system was calibrated. Details of this experimental layout are described in Ref. 16.

The Thomson spectrometer was used in previous studies (see, e.g., Refs. 9, 11, and 16) in an 1:1 imaging mode. An

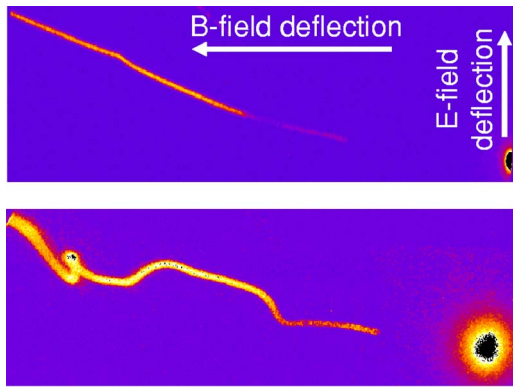


FIG. 1. (Color online) (a) Photograph of an energy dispersed proton trace which is detected with a multichannel plate and phosphorous screen imaging device and a pinhole Thomson spectrometer, the imaging ratio is 1:1 (b) Detected proton trace with a magnified imaging ratio of 1:15, target and laser parameter (see the text).

entrance aperture of $200\ \mu\text{m}$ in diameter was located at a distance of 30 cm from the investigated ion source. The imaging plane of the ion traces was placed behind the aperture at a distance of 30 cm. Laser irradiated tiny water droplets (as used in Refs. 9 and 16) gave perfect parabolic traces from all registered ions. This indicates that the geometry of the deflecting B and E fields of the spectrometer produces no artefacts on the ion trajectories. However, in the experiments with plane target foils some kinks or small bumps have appeared in the ion traces when strong ion (dominantly proton) emission occurred. This effect was also observed if the cutoff energy of the protons was in a range between 2 and 4 MeV under our laser irradiation conditions. The energy of the detected protons ranged between the cutoff energy and approximately 10% of this value. If such deviations were caused by changes in the angular distribution of the proton emission it could limit the spatial resolution in an imaging experiment. Therefore, it is important to measure the scale of that effect and to explain its origin.

III. IMAGING THOMSON SPECTROMETER

In order to study the phenomenon in detail we set up a Thomson spectrometer in a 1:15 imaging mode, i.e., a $30\ \mu\text{m}$ pinhole was positioned at a distance of 5 cm from the source and the detector screen was located 75 cm behind the pinhole. The electric and magnetic fields acted 14 cm in front of the detector screen. With a 1 cm separation between the electric field plates we could observe an area of the target rear side with an extension of $\pm 400\ \mu\text{m}$ relative to the target center with a resolution of $32\ \mu\text{m}$. This resolution depends on the pinhole size, the magnification, the channel resolution of the MCP, and the imaging of the MCP screen on the CCD camera. Two examples of the recorded proton emission with the two different magnification modes are depicted in Fig. 1. The distortion of the parabolic character of the trace recorded at low magnification becomes clearly visible at high magnification. Such a wiggled trace is reproducible. The explicit shape of the trace varies from shot to shot whereas similarities between consecutive shots are clearly seen. Trace bending is observed in different directions. The high energy part

of the emission between the cutoff and approximately 50% of this value shows no deviations from the expected trace.

The observed effect is a feature of the emitted proton beam and it is not caused by a possible injection of additional charged particles into the spectrometer. In principle, such a massive injection of charged particles could change instantaneously the potential on the deflecting plates of the spectrometer. Charge injection has been ruled out by either putting an additional aperture at a 4 kV potential in front of the spectrometer entrance or switching a grounded short circuit to the electrical field plates. If trace deviations occur they are not influenced by these spectrometer modifications. Also we can rule out that the pinhole itself causes the effect because it is observable with quite different pinhole setups. We can conclude that we are measuring a property of proton beam emission from extended planar foil targets. The deviations were not observed with small isolated droplet targets (see, e.g., Refs. 9, 11, and 16) at comparable densities of the emitted ions.

IV. DATA ANALYSIS PROCEDURE

Before we analyze the traces in detail it is worth having a look at the measures we detected. Our apparatus is a combination of a pinhole camera and a spectrometer. If ions from all points of the source pass the pinhole, e.g., they are emitted uniformly, the source extension can be imaged with the pinhole camera. However here, the source emits a beam with a certain opening angle and a small emittance¹³. Several investigations^{11,13} reported the opening angles of the proton beams between 10° and 20° , whereas the extension of the area from which the beams were emitted was between 100 and $500\ \mu\text{m}$ (as given in Refs. 13 and 17). Cowan *et al.*¹³ demonstrated small normalized emittances ε (transversal temperatures) of a proton beam accelerated from laser irradiated foils ($\varepsilon < 0.001\ \text{mm mrad}$). The fact that we detected nonblurred, although wiggled, parabola traces conforms to such a beam characteristic. In our setup the beam illuminates the pinhole and we detect a trace with a certain spread. This spread is a measure of the divergency of a small beamlet where the pinhole acts as the aperture of this small beam. We call it for simplicity the divergence of the beamlet. The position of the trace at the detector is determined by the emission direction at the target surface. The “pointing” is the mean angular direction of the beam at a specific energy, which passed through the pinhole. This emission direction (two angle coordinates) is given by the pinhole position and by the source position. Further the energy of the ions determines the beam deflection inside the spectrometer. The two angle coordinates we call target emission coordinates. They can be given directly in units of an angle or can be calculated as a deviation in x and y directions from a fixed point at the target plane. Emission from a fixed point at target produces an ideal undisturbed Thomson parabola trace. The ideal parabola trace starts from a so called “zero” point at the detector plane. This zero point is a projection of the target point by high energy photons and neutrals which cause a point like blob at the detector. Concerning the coordinate denotation in Fig. 2 we can write the Thomson trace formula:

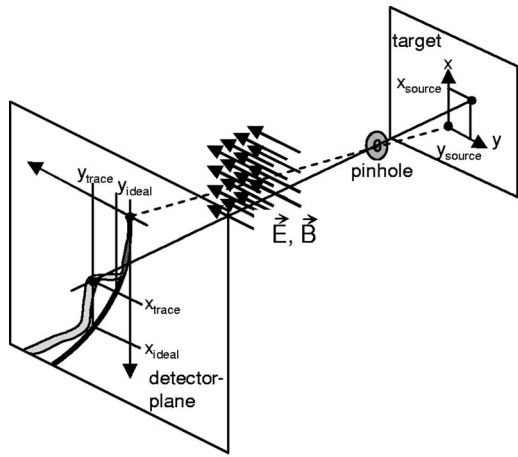


FIG. 2. Scheme of the geometry in the measurement: The source coordinates of the target are imaged to the detector plane via a pinhole and are dispersed due to their energy in the spectrometer (not depicted for simplicity) along a trace (gray shaded area) which will be compared to the ideal parabolic trace (parabolic line). The ideal trace is calculated from a source without directional emission fluctuation.

$$y_{\text{trace}} - y_{t0}(x_{\text{source}}, y_{\text{source}}) = m(x_{\text{trace}}(E) - x_{t0}(x_{\text{source}}, y_{\text{source}}))^2, \quad (1)$$

where m is a spectrometer calibration factor and $(x_{\text{source}}, y_{\text{source}})$, $(x_{\text{trace}}, y_{\text{trace}})$ are the source and trace coordinates, respectively. The coordinates of the zero point at the detector plane are (x_{t0}, y_{t0}) . This formula describes a parabola for ions with different energies E only if the source position $(x_{\text{source}}, y_{\text{source}})$ remains constant for all ions (ideal trace) Otherwise, as visible in the experiment, distortions may occur.

In our measurements we determine two coordinates of each registered signal (or pixel) at the detector plane within the trace. These two coordinates carry the information about the ion trajectory—its direction and energy. However, we are interested in the emission characterization with three parameters and we have to, in order to achieve it, assume that there is an useful interconnection. It should allow to determine the parameters within some uncertainty range. We think that the following approximation Ansatz is possible because we always detected a clear and sharp trace which does not show some strange or irregular blurring.

Our present Ansatz for ions with different starting points $(x_{\text{source}}, y_{\text{source}})$ and “wiggly” traces:

$$y_{\text{trace}} - y_{t0}(x_{\text{source}}, y_{\text{source}}) - m(x_{\text{trace}}(E) - x_{t0}(x_{\text{source}}, y_{\text{source}}))^2 = 0 \quad (2)$$

is approximated by

$$y_{\text{trace}} - y_{t0} - m(x_{\text{trace}}(E) - x_{t0})^2 + \{\partial y(x_{\text{source}}, y_{\text{source}}) + \partial x(x_{\text{source}}, y_{\text{source}})\} = 0. \quad (3)$$

The condition we use for the data analysis is that the major deflection from the zero point is governed by the velocity (energy) of the protons and the distortion (bending, wiggling) from the ideal parabolic trace is influenced by two energy dependent target emission coordinates. In order to get

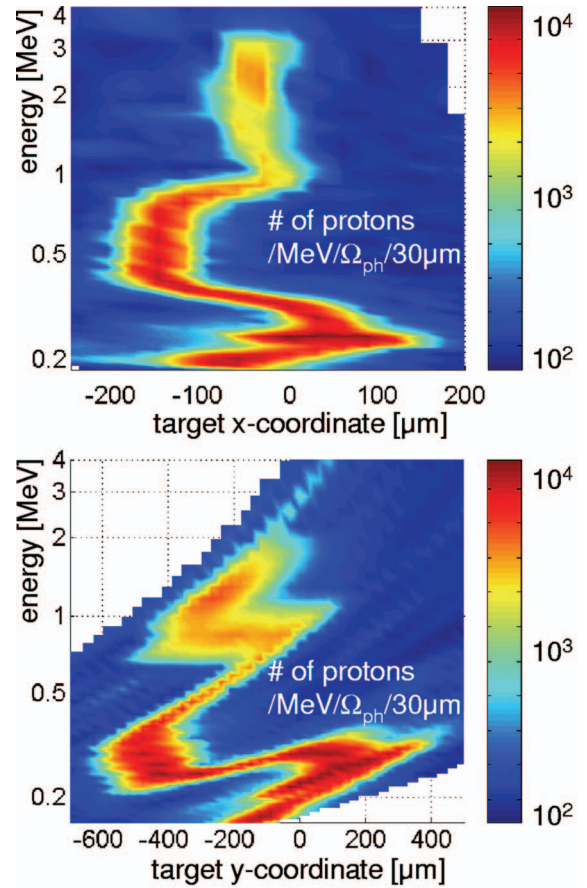


FIG. 3. (Color) Result of the analysis of the recorded proton emission shown in Fig. 1(b). The source emission coordinates x_{source} and y_{source} are plotted as a function of proton energy.

the target emission coordinates for the protons within a certain energy range we applied the following procedure: The coordinates are schematically depicted in Fig. 2. The ideal trace is known from the geometry of the detection system. We assign the x coordinate of a signal x_{trace} to the ion velocity undergoing deflection in the B -field. The y -coordinate y_{trace} is compared to the y value (y_{ideal}) of the ideal trace at this energy. The difference is assigned to the target emission coordinate in y (y_{source}) direction. We can reverse this sequence and start taking the y coordinate of a signal y_{trace} which we assign to the ion velocity undergoing the deflection in the E field. The x coordinate x_{trace} is compared to the x value (x_{ideal}) of the ideal trace at this energy. The difference is assigned to the target emission coordinate in x (x_{source}). Doing so and arranging the data we can assign a range of target emission coordinates in x and y directions to a certain range of velocities (or energies) of the proton beam. The calculation is based on a self developed ray tracing programme.

V. DISCUSSION AND CONCLUSIONS

Figure 3 shows the result of this calculation when the trace in Fig. 1(b) is analyzed. The changes of the target emission coordinates show changes in the beam pointing. From the change of the width of the trace we can infer that the divergence of the beamlet decreases with increasing proton

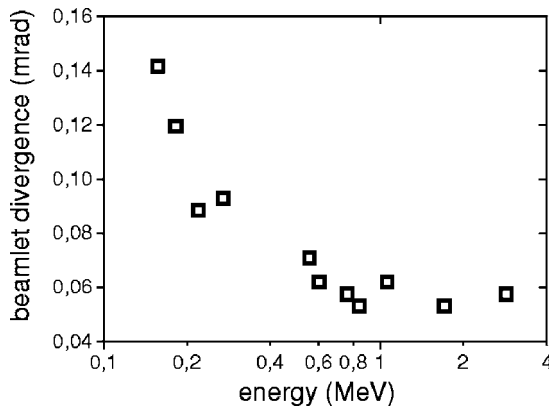


FIG. 4. Divergence of the beamlet calculated from the trace width of the recorded proton beam shown in Fig. 1(b) in dependence of the energy.

energy. The variation of the beam pointing (Fig. 3) and the divergence values of the beamlet are low as one can infer from the numbers in Fig. 4 which have been calculated for the distance of the source to the detector and trace spreading. These values are well suited for imaging experiments. A beam analysis across the whole beam would require an array of pinholes—the so-called pepperpot—which enables determination of the beam emittance. If we multiply the numbers in Fig. 4 by the distance between the pinhole and the detector we can roughly determine the lower limit of the beam emittance under our experimental conditions. These values are $(2\text{--}3) \cdot 10^{-3}$ mm mrad for 2–3 MeV proton energy and approximately 10^{-2} mm mrad for 0.2–0.3 MeV proton energy.

Some visible differences in the target emission coordinates we can partly ascribe to the temporal change of the intensity distribution in the laser beam. The laser intensity and energy determine the pulse of hot electrons propagating through the target and building up the acceleration sheath at the rear side of the target. The focal intensity distribution is spatially symmetrical and no hot spots at a micrometer scale have been observed. The highest intensity at the beam axis is responsible for the peak of a bell-shaped acceleration sheath (as described in Ref. 13). The protons with the highest energies originate in this zone and propagate without significant (noticeable) deviations. Regions of lower intensity are more extended. Irradiation of the target at an incidence angle of 45° causes the illumination to be stretched in y direction and the corresponding coordinate covers a more extended range as visible in Fig. 3. As more as the acceleration sheath expands and the acceleration field strength decreases the emitted lower energetic protons form a beam with higher divergence. This is seen from the width of the registered trace at lower energies.

The more rapid changes of the target emission coordinates as a function of the energy are not simply accessible. These changes of the target emission coordinates or the beam pointing are probably connected with fast changes within the acceleration sheath. These field changes could be affected by changes during the hot electron transport or the circulation of electrons in the acceleration zone. Also microstructure effects of the target can influence the evolving proton beam in a significant way as it was demonstrated in Ref. 13. The

whole scenario needs a very complex modeling. Nevertheless, our recorded traces imply a distinct emission of the protons. The traces, even if bending is strong, are interconnected concerning the energies and are not blurred. This suggests that the protons concerning their velocity (or the energy) are strictly emitted as function of time. The fastest are emitted first. The beam leaves the acceleration sheath with a velocity chirp. Otherwise, the changes of the beam pointing should affect a much larger range of energies. Such a velocity chirp is an important characteristic because it sheds light on the temporal development of the acceleration scenario. A velocity chirp of the accelerated protons was mentioned in respect to theoretical investigations by Cowan *et al.*¹³ A detailed knowledge of the temporal evolution of the acceleration process may help to develop further scenarios for the creation of laser accelerated ion pulses with a strong peak in the energy spectrum.

In summary, we measured variations of the pointing of laser accelerated proton beams. They have become visible for the first time by applying a Thomson spectrometer which detects ions from a source with a high spatial resolution. Thus, small fluctuations of the target emission coordinates could be detected as a function of proton energy. The observed changes in beam pointing are in the order of 0–3 mrad if the proton energy falls below 50% of the cutoff energy. The beam characteristics produced with ultrashort laser pulses—especially the high pointing stability and the low emittance values for protons with energies above 50% of the cutoff value—show that the proton beams of megaelectron volt energy are superior for imaging applications.

ACKNOWLEDGMENTS

The authors thank Karol Janulewicz for stimulating discussions.

This work was partially supported by DFG-Project SFB-Transregio TR 18.

¹E. L. Clark, K. Krushelnick, M. Zepf, F. N. Beg, M. Tatarakis, A. Machacek, M. I. K. Santala, I. Watts, P. A. Norreys, and A. E. Dangor, *Phys. Rev. Lett.* **85**, 1654 (2000).

²A. Maksimchuk, S. Gu, K. Flippo, D. Umstadter, V. Yu., and Bychenkov, *Phys. Rev. Lett.* **84**, 4108 (2000).

³S. P. Hatchett, C. G. Brown, T. E. Cowan, E. A. Henry, J. S. Johnson, M. H. Key, J. A. Koch, A. B. Langdon, B. F. Lasinski, R. W. Lee, A. J. Mackinnon, D. M. Pennington, M. D. Perry, T. W. Phillips, M. Roth, T. C. Sangster, M. S. Singh, R. A. Snavely, M. A. Stoyer, S. C. Wilks, and K. Yasuike, *Phys. Plasmas* **7**, 2076 (2000).

⁴S. C. Wilks, A. B. Langdon, T. E. Cowan, M. Roth, M. Singh, S. Hatchett, M. H. Key, D. Pennington, A. MacKinnon, and R. A. Snavely, *Phys. Plasmas* **8**, 542 (2001).

⁵M. Hegelich, S. Karsch, G. Pretzler, D. Habs, K. Witte, W. Guenther, M. Allen, A. Blazevic, J. Fuchs, J. C. Gauthier, M. Geissel, P. Audebert, T. Cowan, and M. Roth, *Phys. Rev. Lett.* **89**, 085002 (2002).

⁶A. J. Mackinnon, Y. Sentoku, P. K. Patel, D. W. Price, S. Hatchett, M. H. Key, C. Andersen, R. Snavely, and R. R. Freeman, *Phys. Rev. Lett.* **88**, 215006 (2002).

⁷I. Spencer, K. W. D. Ledingham, P. McKenna, T. McCanny, R. P. Singhal, P. S. Foster, D. Neely, A. J. Langley, E. J. Divall, C. J. Hooker, R. J. Clarke, P. A. Norreys, E. L. Clark, K. Krushelnick, and J. R. Davies, *Phys. Rev. E* **67**, 046402 (2003).

⁸M. Allen, Y. Sentoku, P. Audebert, A. Blazevic, T. Cowan, J. Fuchs, J. C. Gauthier, M. Geissel, M. Hegelich, S. Karsch, E. Morse, P. K. Patel, and M. Roth, *Phys. Plasmas* **10**, 3283 (2003).

⁹S. Busch, M. Schnürer, M. Kalashnikov, H. Schönagel, H. Stiel, P. V.

- Nickles, W. Sandner, S. Ter-Avetisyan, V. Karpov, and U. Vogt, *Appl. Phys. Lett.* **82**, 3354 (2003).
- ¹⁰M. Kaluza, J. Schreiber, M. I. K. Santala, G. D. Tsakiris, K. Eidmann, J. Meyer-ter-Vehn, and K. Witte, *Phys. Rev. Lett.* **93**, 045003 (2004).
- ¹¹S. Ter-Avetisyan, M. Schnürer, S. Busch, E. Risse, P. V. Nickles, and W. Sandner, *Phys. Rev. Lett.* **93**, 155006 (2004).
- ¹²M. Borghesi, S. Bulanov, D. H. Campbell, R. J. Clarke, T. Zh. Esirkepov, M. Galimberti, L. A. Gizzi, A. J. MacKinnon, N. M. Naumova, F. Pegoraro, H. Ruhl, A. Schiavi, and O. Willi, *Phys. Rev. Lett.* **88**, 135002 (2001).
- ¹³T. E. Cowan, J. Fuchs, H. Ruhl, A. Kemp, P. Audebert, M. Roth, R. Stephens, I. Barton, A. Blazevic, E. Brambrink, J. Cobble, J. Fernández, J.-C. Gauthier, M. Geissel, M. Hegelich, J. Kaae, S. Karsch, G. P. Le Sage, S. Letzring, M. Manclossi, S. Meyroneinc, A. Newkirk, H. Pépin, and N. Renard-Legallaudec, *Phys. Rev. Lett.* **92**, 204801 (2004).
- ¹⁴M. Borghesi, A. J. MacKinnon, D. H. Campbell, D. G. Hicks, S. Kar, P. K. Patel, D. Price, L. Romagnani, A. Schiavi, and O. Willi, *Phys. Rev. Lett.* **92**, 055003 (2004).
- ¹⁵M. P. Kalachnikov, V. Karpov, H. Schonagel, and W. Sandner, *Laser Phys.* **12**, 368 (2002).
- ¹⁶S. Ter-Avetisyan, M. Schnürer, and P. V. Nickles, *J. Phys. D* **28**, 863 (2005).
- ¹⁷J. Schreiber, M. Kaluza, B. M. Hegelich, U. Schramm, F. Gruner, M. Geissler, E. Brambrink, J. Fuchs, P. Audebert, D. Habs, and K. Witte, *Appl. Phys. B: Lasers Opt.* **79**, 1041 (2004).

Laser acceleration of quasi-monoenergetic MeV ion beams

B. M. Hegelich¹, B. J. Albright¹, J. Cobble¹, K. Flippo¹, S. Letzring¹, M. Paffett¹, H. Ruhl², J. Schreiber^{3,4}, R. K. Schulze¹ & J. C. Fernández¹

Acceleration of particles by intense laser–plasma interactions represents a rapidly evolving field of interest, as highlighted by the recent demonstration^{1–4} of laser-driven relativistic beams of monoenergetic electrons. Ultrahigh-intensity lasers can produce accelerating fields of 10 TV m^{-1} ($1 \text{ TV} = 10^{12} \text{ V}$), surpassing those in conventional accelerators by six orders of magnitude. Laser-driven ions with energies of several MeV per nucleon have also been produced^{5–9}. Such ion beams exhibit unprecedented characteristics—short pulse lengths, high currents and low transverse emittance¹⁰—but their exponential energy spectra have almost 100% energy spread. This large energy spread, which is a consequence of the experimental conditions used to date, remains the biggest impediment to the wider use of this technology. Here we report the production of quasi-monoenergetic laser-driven C^{5+} ions with a vastly reduced energy spread of 17%. The ions have a mean energy of 3 MeV per nucleon (full-width at half-maximum $\sim 0.5 \text{ MeV}$ per nucleon) and a longitudinal emittance of less than $2 \times 10^{-6} \text{ eV s}$ for pulse durations shorter than 1 ps. Such laser-driven, high-current, quasi-monoenergetic ion sources may enable significant advances in the development of compact MeV ion accelerators¹¹, new diagnostics^{12,13}, medical physics¹⁴, inertial confinement fusion and fast ignition^{15–17}.

An ultrahigh-intensity laser ($I\lambda^2 > 10^{18} \text{ W cm}^{-2} \mu\text{m}^{-2}$, where I is intensity and λ is wavelength) incident on a target accelerates a large number of electrons to multi-MeV energies^{18,19}. These electrons traverse typical thin foil targets and set up a very strong electrostatic field exceeding 1 TV m^{-1} . This field ionizes the rear surface and accelerates ions to energies of many MeV. This process is known as target normal sheath acceleration (TNSA)⁵. Experiments have demonstrated acceleration of protons to more than 60 MeV (ref. 8), fluorine ions to above 100 MeV (ref. 6) and high- Z palladium ions up to 225 MeV (ref. 20), that is, more than 2 MeV per nucleon. These ion beams have a much lower transverse temperature and a much shorter duration and a much higher current than those from conventional accelerators. These unique characteristics make them ideal candidates for a number of experiments not feasible otherwise.

Owing to their short pulse length and high energy content, the ion beams can heat macroscopic amounts of matter to more than $10^6 \text{ }^\circ\text{C}$ before the matter can expand²¹, thereby creating conditions of high temperature and density only found in the interior of stars. Conversely they can also be used as a probe to investigate ion transport and stopping in a hot, dense plasma before it has time to disassemble. Conventional accelerators are hard pressed to deliver enough particles in the available $\sim\text{ps}$ time window to make high-quality measurements feasible. These are but two examples where the high current and short pulse duration are the key to an otherwise impossible experiment. More examples can be found in nuclear

physics, fusion research and other areas—examples are the synthesis of neutron rich nuclei or the measurement of fusion cross-sections in supernova-like hot, dense plasma conditions. The much higher beam current and the much lower emittance of the laser-driven ion beams make them a promising candidate for advanced accelerator concepts.

Today, a standard linear accelerator that matches the MeV/ u energy level (with u being the atomic mass unit) of these laser-driven ions is $\sim 100 \text{ m}$ long. In contrast, the laser fits in a large room and accelerates the ions to MeV/ u over just $10 \mu\text{m}$. The low duty-cycle in present experiments is a limitation that is likely to be mitigated by the next generation of high-power lasers, currently under development. However, the major difficulty with all the TNSA and other laser-driven ion-acceleration mechanisms^{9,22} has been the resulting maxwellian energy distribution, with a typical 100% energy spread^{16,8,9}. All the above-mentioned applications would benefit greatly from a narrower energy distribution, centred about a specific value.

We report here a laser-driven quasi-monoenergetic ion beam, a

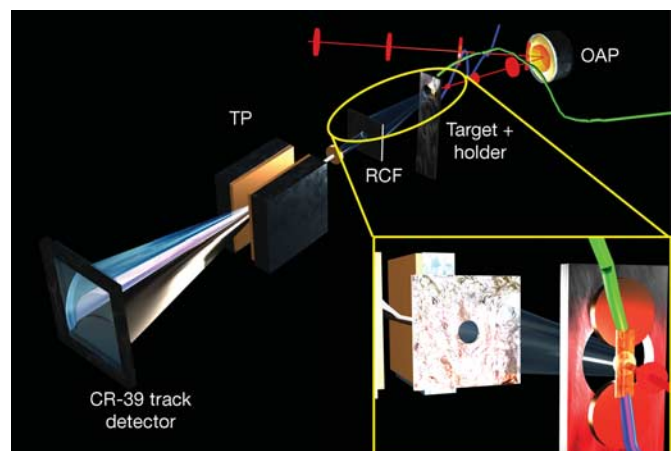


Figure 1 | Experimental set-up. A short, high-intensity laser pulse is focused on a thin metal foil target by an off-axis parabolic mirror (OAP). The red line shows the laser beam axis, and the red disks represent the laser pulse travelling along that axis and getting focused down by the OAP. Two wires (green and blue) are attached to the target, pass a current through it and heat it to $\sim 1,100 \text{ K}$ to remove contaminants. Ions are accelerated at the target rear surface and are detected by a stack of radiochromic film (RCF) and a Thomson parabola (TP) spectrometer using CR-39 track detectors. The inset shows an enlarged frontside view of the target, with the target and the green and blue wires being in the lower right corner and the RCF and TP detectors in the upper left.

¹Los Alamos National Laboratory, Los Alamos, New Mexico 87545, USA. ²University of Nevada, Reno, Nevada 89557, USA. ³Ludwig-Maximilians-Universitaet Muenchen, ⁴Max-Planck-Institut für Quantenoptik, Garching 85748, Germany.

C^{5+} beam created in the interaction of a 20 TW/0.8 ps laser pulse with a solid target. A simple schematic illustrating the process can be found in Supplementary Information (sections SI_1 and SI_2). The experiments were performed at the LANL Trident laser facility. The experimental set-up is shown in Fig. 1 (for details see Methods), and a time-integrated photograph of an actual laser shot is shown in Supplementary Information section SI_3. The monoenergetic signature is the direct result of a fundamentally different target composition employed in these experiments. In TNSA, the ions with the highest charge-to-mass ratio dominate the acceleration, gaining the most energy. Given typical vacuum conditions of $\sim 10^{-6}$ mbar, surface target contaminants containing protons are always present. These protons have the largest charge-to-mass ratio by at least a factor of 2. Controlled treatment of foil targets before irradiation with the ultrahigh-intensity laser reduces adsorbed and absorbed proton contaminants to an unobservable level, allowing higher-Z ions to be the dominant species⁶. Using the right treatment parameters and target materials, a thin source layer of just a few monolayers can be formed by catalytic processes.

Specifically, we have demonstrated the acceleration of C^{5+} and C^{6+} from an ultrathin layer of graphitic carbon, formed from catalytic decomposition of adsorbed hydrocarbon impurities on a 20 μm palladium foil. Unlike the low-energy lasers which are used for electron acceleration²⁻⁴, which have a high repetition rate and allow the taking of many shots to obtain good statistics, ion acceleration requires higher energy lasers which are single shot in nature. The number of shots is extremely limited and fluctuations in the laser parameters further complicate obtaining good statistics. However, five shots exhibiting monoenergetic carbon ions have been observed in two separate campaigns months apart, and another ten shots showing indication of monoenergetic ions are still being analysed. Figure 2 shows the measured C^{5+} spectrum (black curve) with the lowest ratio $\Delta E/E$ of $\sim 17\%$, where E is the mean energy of the C^{5+} ions and ΔE is their energy spread. It also shows the corresponding highest substrate charge state Pd^{22+} (blue). Having the highest

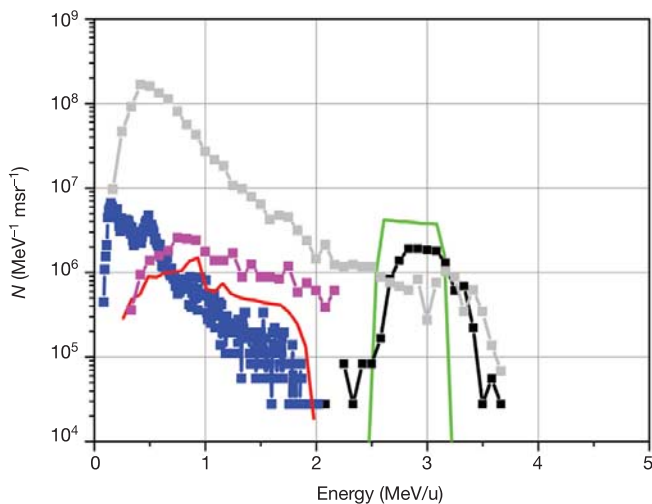


Figure 2 | Monoenergetic carbon ions from a 20 μm palladium substrate. The curves show ion number (N) over energy per nucleon (MeV/u). The black curve shows the spectra of the measured C^{5+} ions, the blue curve shows the dominant substrate charge state Pd^{22+} . The green and the red curves are simulations obtained using the 1D-hybrid-code BILBO, showing the simulated C^{5+} and Pd^{21+} spectra, respectively. The grey curve shows the dominant C^{4+} signal from a heated W target, and the magenta trace shows the C^{5+} signal from a cold Pd target. In these last two cases, the targets have a thick layer of carbon contaminants and do not form a monolayer source. The resulting carbon signals are therefore exponential and show lower numbers in the high-energy range. The errors are: $dN \leq 1\%$ statistical accuracy, and $dE \leq 2\%$ for C and $dE \leq 4.5\%$ for Pd.

charge-to-mass ratio of 0.42, the C^{5+} is dominantly accelerated. Owing to the extremely small spatial extent of the carbon layer and its localization at the rear surface, all of the carbon ions are accelerated at once at the peak of the accelerating field, leading to the monoenergetic ion pulse. After all carbon ions are accelerated, the field is still very strong and only moderately screened by the carbon, therefore the next highest charge-to-mass ratio ion—that is, Pd^{22+} with a charge-to-mass ratio of 0.2—is now dominantly accelerated and gains a large fraction of the energy before the field decays and lower Pd charge states are created and accelerated.

For the purpose of this Letter we limit our discussion to the two dominant charge states, which together contain $\sim 20\%$ of the total integrated ion energy and have a bearing on the results reported here. The leading short bunch of C^{5+} ions shows a monoenergetic energy distribution with a mean energy of $E \approx 36$ MeV, that is, 3 MeV per nucleon and a full-width at half-maximum of 0.5 MeV per nucleon. We infer that the accelerated C^{5+} ion bunch has a longitudinal emittance of $\epsilon_1 < 2 \times 10^{-6} \pi$ eV s, improving on conventional high-current accelerators by orders of magnitude. Also, in contrast to the Pd and to any previous measurements, no lower C charge states are present. Closer analysis reveals important differences in the acceleration mechanism for the Pd substrate ions and the C ions from the source surface layer. Whereas the substrate ions have a typical exponential spectrum, the C ions are monoenergetic.

The small energy spread of the observed carbon ions can be understood from consideration of quasi-neutral ($n_e = Z_{\text{Pd}} n_{\text{Pd}}$), adiabatic expansion in one dimension (1D) of a palladium substrate coated by a very thin film of carbon. (Here n_e is the electron density, n_{Pd} the palladium density and Z_{Pd} the mean palladium charge state.) The electric field obeys $eE \approx -m_e n_e^{-1} \partial_x \int dv v^2 (f_e - Z_{\text{Pd}} f_{\text{Pd}})$, with f_e and f_{Pd} the distribution functions of electrons and palladium ions, e the elementary charge, m_e the electron mass and v velocity. Such a plasma column will expand with sound speed c_s to characteristic size $L^2(t) = L_0^2 (1 + t^2 c_s^2 / L_0^2)$. The ion and electron temperatures will therefore decrease by a factor $L_0/L(t)$, which leads to an electric field $eE \approx x c_s^2 m_{\text{Pd}} Z_{\text{Pd}}^{-2} L^{-2}$, where m_{Pd} is the atomic mass of palladium. This field leads to an acceleration $d^2 x_C / dt^2 = r x_C c_s^2 L^{-2}$ of the carbon ions, with x_C being the spatial coordinate of the carbon ions. The dynamics of the layer are characterized by r , the ratio of charge-to-mass ratios of C to Pd ions: for $r \gg 1$, the carbon layer detaches from the substrate at early time and propagates ahead of it as a directed bunch. For $r < 1$, the substrate overtakes the C layer and flow instabilities may arise. With an average Pd charge state $Z_{\text{eff,Pd}} \approx 7$, one obtains $r = 6.3$, predicting a clean separation of

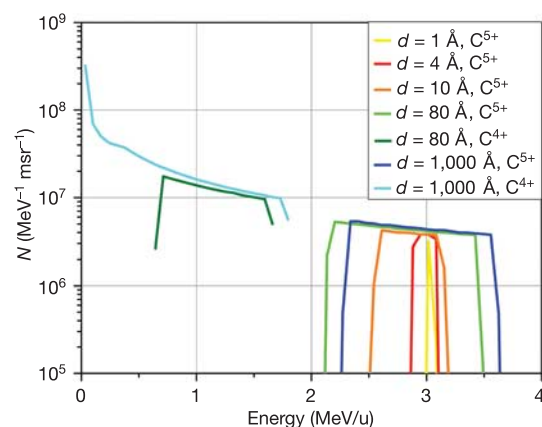


Figure 3 | Changing the thickness of the carbon source layer leads to a change in the energy spectrum in the BILBO simulations. Decreasing the layer thickness (d) causes the spectrum to become more monoenergetic. Increasing the layer thickness leads to a broader distribution and ultimately the appearance of lower charge states and a Maxwellian spectrum.

the carbon ions from the substrate. Esirkepov *et al.*²³ have also examined the problem of monoenergetic ion acceleration, but their model relies explicitly upon finite transverse extent of the target and is not applicable to the TNSA scenario we find in our experiments.

In order to improve our understanding and our predictive capability, we developed a numerical model that simulates the ionization and acceleration physics. Full *ab initio* simulations with the required dynamics and sufficiently low noise levels to faithfully capture the ionization kinetics are not feasible, so we have focused on a reduced model that takes into account the essential physics. This 1D-hybrid model BILBO (backside ion lagrangian blow-off) uses a relativistic Boltzmann fluid model of the electrons and represents ions as kinetic simulation particles. This model has been explicitly designed to implement TNSA⁵ in a heterogeneous mixture of ionization species and ion types. In our simulations, a thin layer of carbon (1–1,000 Å) with areal density $\rho = 5 \times 10^{-10}$ – 5×10^{-7} g cm⁻² is placed on the surface of a palladium foil of solid density $\rho = 12.16$ g cm³ and a thickness of 20 μm. Using parameters matched to the experiment (see Methods), we are able to reproduce the experimental results.

Figure 2 shows the energy spectra of the C⁵⁺ (green) and Pd²¹⁺ (red) components obtained in the simulation. The energy per nucleon of the C⁵⁺ ions agrees well with the measured energies and the total number of ions accelerated, albeit with a somewhat smaller energy spread. The energy spectrum and peak ionization state of Pd between 50 and 200 MeV are likewise in good agreement with the data. From this simulation we can also infer a source layer thickness of ~10 Å (that is, a few monolayers), which is in good agreement with published measurements—for example, using Auger spectroscopy^{24,25}. In our parametric simulation study, increasing the number of initial carbon layers while keeping the density fixed leads to two effects, shown in Fig. 3. The mean energy of the C⁵⁺ beam decreases and the energy spread increases with increased layer thickness. This trend continues until adequate space charge exists in the carbon layer to shield the ionizing electric field experienced by the carbon ions at the back of the layer. These more deeply buried carbon ions only attain ionization state C⁴⁺ and they separate from the layer of C⁵⁺ ions; for the parameters considered in this study, this occurs for areal charge densities exceeding $\sim 2 \times 10^{-8}$ g cm⁻², corresponding to a layer thickness of ~80 Å and above. Lower carbon ionization states appear with increasing layer thickness, and the ion energies eventually approach a maxwellian distribution. This behaviour is also seen in the experiment (Fig. 2). The grey curve shows the C⁴⁺ spectrum from a laser shot of comparable energy but from a tungsten target, which is not a catalyst for the required surface chemistry, and therefore does not form a thin source layer.

Measurements using transmission electron microscopy (see Supplementary Information section SI_4) reveal that upon heating, the target actually forms a 400-Å-thick tungsten carbide (W₂C) layer. This surface layer is not thin enough, and as a consequence the C spectrum is maxwellian and all lower charge states are present, as observed in earlier experiments⁶. Comparison of the two spectra shows that the direct production of monoenergetic ions by thin source layers is more effective than just slicing the equivalent energy range out of the maxwellian spectrum. Specifically, the number of ions in the corresponding energy range from 2.5 to 3.5 MeV per nucleon is a factor of 2 lower than in the monoenergetic case. Comparison with a cold Pd target shot at similar laser conditions also shows a maxwellian distribution of considerable lower energy (magenta curve, Fig. 2), because (1) the protons drain energy; and (2) the localized source layer is not formed. Our model predicts that the energy spread in the carbon beam may be minimized by localizing the initial carbon layer spatially, that is, by minimizing the source layer thickness, a process which should also result in higher mean energy of the light ion beam. This hypothesis will be tested in future experiments.

Our experimental results, simulation and analytic modelling have

established the basis for laser-driven acceleration of monoenergetic ion beams using specifically designed and treated targets. Moreover, catalytic metal substrates such as Pd offer the chance of having a target that configures itself *in situ* if subjected to the right conditions. Such a target would solve major technical obstacles for a host of possible applications, making future laser-based accelerators much more feasible. We recently confirmed these results by repeating the experiments in another campaign at the Trident facility, using a substantially equivalent experimental set-up, where we reproduced the qualitative findings reported here. Although the errors in the analysis for any specific shot are small, the reproducibility of our C⁵⁺ results from shot to shot is only ~50%, possibly owing to the degree of control and diagnosis of key input parameters achievable in our present experimental set-up. Large, high-energy, single-shot glass lasers have typical shot-to-shot power fluctuations of ~25%, and the focal spot conditions drift over time. Varying preplasma conditions and possible self-focusing add further to the variability of the results.

The resulting unique beam characteristics, including short pulse duration, high current and small transverse and longitudinal emittances, represent a strong incentive to pursue further research and applications, such as advanced accelerator concepts¹¹, laboratory astrophysics, isochoric heating²¹, fusion science¹⁵ and medical physics¹⁴. The achieved particle energy is already in the right energy range for fusion applications like fast ignition, whereas particle number and conversion efficiency have to be substantially increased. For medical applications like tumour therapy the situation is the opposite: here, the particle numbers are sufficient but the particle energy has to be increased substantially. Considering the fast paced progress in ultrahigh intensity laser technology in recent years, it is reasonable to anticipate progress on all these issues and the deployment of a laser-driven, quasi-monoenergetic ion accelerator in the not so distant future. Progress made in diode-pumped glass laser systems, especially, should enable far higher repetition rates of 0.1–1 Hz (ref. 26). At these repetition rates, several applications in accelerator physics, medical physics, material science and neutron physics become feasible.

METHODS

Laser system and diagnostics. The experiments were performed at the short pulse arm of the Trident Nd:glass laser facility at Los Alamos National Laboratory. The Trident C-beam delivers up to 30 TW in a 20 J, ~600 fs pulse at 1.054 μm wavelength, using chirped pulse amplification²⁷. The typical pulse contrast is $\sim 10^{-6}$ at 2 ns before the peak of the pulse. As illustrated in Fig. 1, an off-axis parabolic mirror is used to focus the laser pulse onto a thin foil target at 22.5° with respect to the target normal. Typical focal spot sizes are ~10 μm radius, resulting in intensities on target of $\sim 10^{19}$ W cm⁻². A stack of Gafcom radiochromic film (RCF) is placed behind the target to record the ion beam profile. A hole in the middle of this film stack provides a line of sight for a Thomson parabola (TP) ion spectrometer²⁸ attached to the outer chamber wall. The Thomson parabola deflects the ions by means of parallel electric and magnetic fields, so that the projection of their path in the detector is defined by parabolic traces. Ions with different charge-to-mass ratios are deflected onto different traces, while their positions on a given trace are determined by their energies. A CR-39 solid state nuclear track detector records the ions, typically ~300,000 per shot, and is read out by a specialized automated analysis system²⁹. With properly chosen parameters, the counting error is below 0.01%. The error in ion numbers per energy bin (dN) is dominated by Poisson statistics, and is below ≤1% owing to the large number of counts per shot. For example, for the C⁵⁺ trace in Fig. 2, dN ≈ 0.3%. The solid angles of the TPs are 3.4×10^{-5} milliradians (msr), and the opening angles of the ion beams are 24–100 msr depending on charge state and energy. The TPs are absolutely calibrated for energy and the energy error is dominated by the pinhole size (100 μm). It is given as $dE \sim E^{3/2}$, yielding an upper boundary for an energy error of less than 1 MeV for ~45 MeV carbon, that is, less than 2% and decreasing with energy.

Target treatment and chemistry. The foil target is heated to $T_1 \approx 1,100$ K by two attached wires that pass a current through the foil. Palladium at room temperature is a hydrogen-getter, that is, H can be found throughout the bulk of the material as well as on the surfaces. The heating process desorbs the hydrogen contaminants (adsorbed and absorbed in the foil), thus enabling the efficient acceleration of heavier ions. In the experiment presented here, the special

catalytic surface chemistry of palladium causes a few carbon monolayers of hydrocarbon contaminants to remain on the surface of the palladium substrate and form a well defined source layer for the monoenergetic carbon beam. Given the ambient vacuum of $\sim 10^{-6}$ mbar, the surface is contaminated with various C_xH_y compounds. When the Pd is heated, the Pd surface undergoes multiple phase changes^{24,25} and the loosely bound H is driven out of the bulk and off the surfaces. At 600 K the target is completely dehydrogenized. The carbon, however, remains on the surface in various different configurations. When heating the target further, to temperatures $T > 1,100$ K, the various carbon compounds undergo a phase change, forming a well-defined, very thin graphite layer at the monolayer scale on the Pd surface. If heated up further, to above 1,300 K, this layer will be removed and a clean Pd surface remains. In the experiment, we did not reach this last state, but remained in the graphite regime, thereby preparing a thin source layer perfect for creating monoenergetic ions.

BILBO hybrid code. In BILBO, ion formation and acceleration is accomplished by the electric fields of a virtual cathode of hot electrons at the back surface of the target. Assuming separation of the electron and ion timescales, self-consistent electric fields are obtained by solving the time-stationary relativistic Vlasov–Maxwell equations for each electron component. These fields accelerate the ions and ionize them to higher charge states, where ionization is implemented in BILBO by means of a threshold ionization model³⁰. The boundary conditions require the electric field to vanish within the target and far from the target surface. In addition, the electron densities and temperatures of the hot and cold components are specified within the target as internal boundary conditions. The hot electron density and temperature are functions of the laser energy deposition model, and their dynamics include adiabatic expansion and the loss of energy to ionization and ion acceleration. The cold electron temperature increases from ohmic heating and collisions with the hot electron component. In the simulations, the laser spot diameter was assumed to be 30 μm ; 50% absorption of the incident laser into hot electrons was assumed ($T_h \approx 2.5$ MeV), with the hot electrons' density assumed to be equal to the critical density ($n_e = 1.01 \times 10^{21}$). The cold electrons had $n_c = 6.8 \times 10^{22} \text{ cm}^{-3}$ and initial cold electron temperature $T_c = 10$ eV. The density and temperature profiles of the hot electron component were assumed to evolve in time with gaussian shape during the pulse rise and have a full-width at half-maximum of 700 fs. The simulation used 5×10^4 simulation ions of each species, had a time step of 2 fs, and employed 6×10^5 simulation cells over a domain of size 100 μm .

Received 17 August; accepted 3 November 2005.

- Katsouleas, T. Accelerator physics: Electrons hang ten on laser wake. *Nature* **431**, 515–516 (2004).
- Faure, J. *et al.* A laser–plasma accelerator producing monoenergetic electron beams. *Nature* **431**, 541–544 (2004).
- Mangles, S. *et al.* Monoenergetic beams of relativistic electrons from intense laser–plasma interactions. *Nature* **431**, 535–538 (2004).
- Geddes, C. *et al.* High-quality electron beams from a laser wakefield accelerator using plasma-channel guiding. *Nature* **431**, 538–541 (2004).
- Hatchett, S. *et al.* Electron, photon, and ion beams from the relativistic interaction of Petawatt laser pulses with solid targets. *Phys. Plasmas* **5**, 2076–2082 (2000).
- Hegelich, M. *et al.* MeV ion jets from short-pulse-laser interaction with thin foils. *Phys. Rev. Lett.* **89**, 085002 (2002).
- Roth, M. *et al.* Energetic ions generated by laser pulses: A detailed study on target properties. *Phys. Rev. Spec. Topic Accelerators Beams* **5**, 061002 (2002).
- Snavely, R. *et al.* Intense high-energy proton beams from petawatt-laser irradiation of solids. *Phys. Rev. Lett.* **85**, 2945–2948 (2000).
- Maksimchuk, A., Gu, S., Flippo, K., Umstadter, D. & Bychenkov, V. Yu. Forward ion acceleration in thin films driven by a high-intensity laser. *Phys. Rev. Lett.* **84**, 4108–4111 (2000).
- Cowan, T. *et al.* Ultralow emittance, multi-MeV proton beams from a laser virtual-cathode plasma accelerator. *Phys. Rev. Lett.* **92**, 204801 (2004).
- Habs, D., Pretzler, G., Pukhov, A. & Meyer-ter-Vehn, J. Laser acceleration of electrons and ions and intense secondary particle generation. *Prog. Part. Nucl. Phys.* **46**, 375–377 (2001).
- Cobble, J. A., Johnson, R. P., Cowan, T. E., Renard-Le Galloudec, N. & Allen, M. High resolution laser-driven proton radiography. *J. Appl. Phys.* **92**, 1775–1779 (2002).
- Borghesi, M. *et al.* Proton imaging: a diagnostic for inertial confinement fusion/fast ignitor studies. *Plasma Phys. Control Fusion* **43**, A267–A276 (2001).
- Ledingham, K. *et al.* High power laser production of short-lived isotopes for positron emission tomography. *J. Phys. D* **37**, 2341–2345 (2004).
- Kodama, R. *et al.* Fast heating of ultrahigh-density plasma as a step towards laser fusion ignition. *Nature* **412**, 798–802 (2001).
- Roth, M. *et al.* Fast ignition by intense laser-accelerated proton beams. *Phys. Rev. Lett.* **86**, 436–439 (2001).
- Temporal, M., Honrubia, J. J. & Atzeni, S. Numerical study of fast ignition of ablatively imploded deuterium–tritium fusion capsules by ultra-intense proton beams. *Phys. Plasmas* **9**, 3098–3107 (2002).
- Wilks, S. *et al.* Energetic proton generation in ultra-intense laser–solid interactions. *Phys. Plasmas* **8**, 542–549 (2001).
- Atzeni, S. & Meyer-ter-Vehn, J. *The Physics of Inertial Confinement Fusion* (Oxford Univ. Press, Oxford, 2004).
- Hegelich, M. *et al.* Spectral properties of laser-accelerated mid-Z MeV/u ion beams. *Phys. Plasmas* **12**, 056314 (2005).
- Patel, P. *et al.* Isochoric heating of solid-density matter with an ultrafast proton beam. *Phys. Rev. Lett.* **91**, 125004 (2003).
- Gitomer, S. J. *et al.* Fast ions and hot electrons in the laser–plasma interaction. *Phys. Fluids* **29**, 2679–2688 (1986).
- Esirkepov, T. Zh. *et al.* Proposed double-layer target for the generation of high-quality laser-accelerated ion beams. *Phys. Rev. Lett.* **89**, 175003 (2002).
- Hamilton, J. C. & Blakeley, J. M. Carbon segregation to single crystal surfaces of Pt, Pd and Co. *Surf. Sci.* **91**, 199–217 (1980).
- Ramsier, R. D., Lee, K.-W. & Yates, J. T. Jr A sensitive method for measuring adsorbed carbon on palladium surfaces: Titration by NO. *J. Vac. Sci. Technol.* **13**, 188–194 (1995).
- Hein, J. *et al.* Diode-pumped chirped pulse amplification to the joule level. *Appl. Phys. B* **79**, 419–422 (2004).
- Mourou, G. A. & Umstadter, D. Extreme light. *Sci. Am.* **286**, 80–86 (2002).
- Thomson, J. J. Rays of positive electricity. *Phil. Mag.* **21**, 225–249 (1911).
- Rusch, G., Winkel, E., Noll, A. & Heinrich, W. The Siegen automatic measuring system for track detectors: New developments. *Nucl. Tracks Radiat. Meas.* **19**, 261–265 (1991).
- Augst, S., Meyerhofer, D. D., Strickland, D. & Chint, S. L. Laser ionization of noble gases by Coulomb-barrier suppression. *J. Opt. Soc. Am. B* **8**, 858–867 (1991).

Supplementary Information is linked to the online version of the paper at www.nature.com/nature.

Acknowledgements We acknowledge the expert support of the Trident laser team, especially R. Johnson, T. Ortiz and R. Gonzales, and the target fabrication support from LANL group MST-7, particularly R. Perea. This work was supported by the LANL Laboratory Directed Research & Development (LDRD) programme. One of the authors (H.R.) was supported by DOE/NNSA-UNR and another (J.S.) by DFG and BMBF.

Author Contributions B.M.H. conceived the experiment, B.M.H., J.C., S.L. and J.C.F. executed the experiment, B.M.H., J.S., K.F. and J.C.F. analysed the data, H.R., B.J.A. and B.M.H. did the theory, M.P. and R.K.S. helped with the material science part and palladium surface chemistry, and B.M.H., B.J.A. and J.C.F. wrote the paper.

Author Information Reprints and permissions information is available at npg.nature.com/reprintsandpermissions. The authors declare no competing financial interests. Correspondence and requests for materials should be addressed to B.M.H. (hegelich@lanl.gov).

Influence of the Laser Prepulse on Proton Acceleration in Thin-Foil Experiments

M. Kaluza, J. Schreiber, M. I. K. Santala, G. D. Tsakiris, K. Eidmann, J. Meyer-ter-Vehn, and K. J. Witte

Max-Planck-Institut für Quantenoptik, Hans-Kopfermann-Straße 1, D-85748 Garching, Germany

(Received 8 December 2003; published 20 July 2004)

We investigate the influence of the laser prepulse due to amplified spontaneous emission on the acceleration of protons in thin-foil experiments. We show that changing the prepulse duration has a profound effect on the maximum proton energy. We find an optimal value for the target thickness, which strongly depends on the prepulse duration. At this optimal thickness, the rear side acceleration process leads to the highest proton energies, while this mechanism is rendered ineffective for thinner targets due to a prepulse-induced plasma formation at the rear side. In this case, the protons are primarily accelerated by the front side mechanism leading to lower cutoff energies.

DOI: 10.1103/PhysRevLett.93.045003

PACS numbers: 52.38.Kd, 29.30.Ep, 41.75.Jv

Proton and ion acceleration using high-intensity lasers is a field of rapidly growing interest. For possible applications of proton beams produced in laser-solid interactions like the imaging of electromagnetic fields in overdense plasmas [1] and the envisaged usage of proton beams in the fast-ignitor scenario [2], the generation of beams with controllable parameters such as energy spectrum, brightness, and spatial profile is crucial. Hence, for the reliable generation of proton beams, the physics underlying the acceleration processes has to be well understood. After the first proof-of-principle experiments [3–6], systematic studies were carried out to examine the influence of target material and thickness [7–9]. To establish the influence of the main laser parameters such as intensity, pulse energy, and duration over a wide range, results from different laser systems have to be compared, since usually each system covers a small parameter range only. Besides these parameters, strength and duration of the prepulse due to amplified spontaneous emission (ASE) play an important role, too [7], but until now a detailed investigation has not yet been carried out.

In most experiments, protons with energies exceeding 1 MeV have been observed. They originate from water and hydrocarbon molecules adsorbed at the target surfaces due to the unavoidable presence of water and pump oil vapor in the target chamber. The origin of the most energetic protons is still debated. There are at least two acceleration scenarios able to explain the occurrence of MeV protons. (i) They may come from the *front* surface of the target, i.e., the side irradiated by the laser pulse [3,4,10] or (ii) from the *rear* surface [5,11,12]. Recent results indicate that both mechanisms act simultaneously [13,14], in accordance with the predictions of multidimensional particle-in-cell (PIC) codes [15,16].

In this Letter, we report on experiments performed to investigate the effect both of the ASE prepulse duration and the target thickness on the acceleration of protons. The proton cutoff energy depends very sensitively on the combination of these two parameters. For a fixed prepulse duration, the highest proton energies are obtained at an

optimal target thickness, which in turn is determined by the ASE prepulse duration. The results can be consistently interpreted if one assumes that above this thickness, the fastest protons are accelerated at the target rear side, while for thinner targets this mechanism is rendered ineffective and only the front side acceleration is active, resulting in lower proton cutoff energies. Furthermore, our results allow a comparison of the experimental results obtained with different laser systems.

The experiments were carried out with the ATLAS laser system at the Max-Planck-Institut für Quantenoptik. It consists of a MIRA oscillator delivering 100-fs pulses of 790-nm wavelength. The pulses are stretched to 160 ps followed by a regenerative amplifier (RA), two multipass amplifiers, and a grating compressor. The output pulses have a duration of $\tau_L = 150$ fs (FWHM) with an on-target energy, E_L , between 600 and 850 mJ. The *p*-polarized beam is focused under 30° incident angle by a $f/2.5$ off-axis parabolic mirror onto Al foils of 0.75 to 86- μm thickness. About 60% of the pulse energy is contained in a spot of $r_f \approx 2.5$ μm radius, resulting in an averaged intensity, I_L , slightly above 10^{19} W/cm² within this spot. The high-intensity part of the pulse is preceded by a 6-ns long low-intensity pedestal due to ASE mainly generated in the RA. The prepulse duration can be controlled by means of an ultrafast Pockels cell located after the RA with a top-hat-like temporal gate of 6-ns duration. The rise time of the leading edge is 300 ps and the gate jitter is 150 ps. By changing the position of the gate relative to the main pulse, the pedestal is either fully or partially transmitted or almost fully suppressed to a minimum prepulse duration of (500 ± 150) ps. The intensity ratio between main and prepulse is better than 2×10^7 and the increase of the intensity above the pedestal level, as measured by a third-order autocorrelator [17], starts 11 ps before the peak intensity.

Two different proton detectors were used. Pieces of CR 39 were placed 82 mm behind the target to record the spatial profile of the proton beam. Covering a half-opening angle of $\sim 20^\circ$, they were wrapped with a 12- μm

Al foil to filter out heavier ions and protons with energies below 900 keV. Through a small hole around the target normal direction, ions could pass to be detected by a Thomson parabola. In such a spectrometer, ions with different charge-to-mass ratios are dispersed by parallel electric and magnetic fields onto distinct parabola tracks in the plane of the detector (CR 39). After etching the CR 39, the ion pits were counted under a computer-controlled microscope, revealing the exact energy spectra.

We have performed several series of measurements, varying the ASE duration, τ_{ASE} , the laser intensity, I_L , and the target thickness. Figure 1 shows the measured proton cutoff energies versus the target thickness for $I_L = 1.0 \times 10^{19} \text{ W/cm}^2$ and ASE durations of 0.5, 0.7, and 2.5 ns, respectively. For each duration we find that with increasing target thickness the cutoff energy first increases and then drops again. The highest proton energies are achieved at an optimal target thickness. When the prepulse duration is changed, this optimal value changes correspondingly, as it is shown in the inset. For thicker targets, the prepulse duration appears to have no effect on the proton cutoff energies, whereas for thinner targets and longer τ_{ASE} the cutoff energies are reduced.

To check the influence of the laser intensity, we have performed shots with constant prepulse duration of 2.5 ns but slightly different laser intensities by changing the laser energy (Fig. 2). While the proton cutoff energies strongly depend on I_L , the optimal thickness appears to depend on the prepulse duration only (cf. Fig. 1).

The proton spectra around the optimal target thickness measured with an intensity of $1.3 \times 10^{19} \text{ W/cm}^2$ and a prepulse duration of 2.5 ns are plotted in Fig. 3. In addition to the rather cold proton component dominating the spectrum of the 2- μm foil with a Boltzmann-like tem-

perature of $250 \pm 30 \text{ keV}$, a population with a significantly higher temperature of $800 \pm 200 \text{ keV}$ and $4.0 \pm 0.6 \text{ MeV}$ appears in the 5 and 8.5- μm foil spectra, respectively. The temperatures of the hottest proton component, given in the inset, exhibit a similar behavior as the cutoff energies, i.e., the proton temperature drastically decreases below the optimal target thickness.

The spatial profiles of the proton beam also change around the optimal thickness. Figures 4(a)–4(c) show the proton beam profiles obtained with targets 2, 5, and 8.5 μm thick. While the first profile is rather blurred, a collimated feature aligned along the target normal appears in Figs. 4(b) and 4(c), persisting for all thicker targets.

The significant changes in proton spectra and beam profiles described above can be interpreted as a transition between two regimes delimited by the optimal thickness: (i) Only the front side acceleration is active for targets thinner than the optimal thickness and (ii) protons are accelerated from both target surfaces for target thicknesses above the optimal value. In this second regime, the rear side acceleration leads to higher cutoff energies. This mechanism is suppressed in the first regime due to the formation of an ASE-induced density gradient at the rear side of the target.

On the target front side, the high-intensity part of the laser pulse interacts with a plasma created by the ASE prepulse. Electrons are expelled from high-intensity regions by the ponderomotive potential of the laser, $\varphi_p = m_e c^2 (\gamma_{\text{os}} - 1)$, until it is balanced by the electrostatic potential arising from the charge separation. Here, $\gamma_{\text{os}} = \sqrt{1 + I_L \lambda_L^2 / (1.37 \times 10^{18} \text{ W cm}^{-2} \mu\text{m}^2)}$ is the relativistic factor, m_e the rest mass of the plasma electrons. Sentoku *et al.* showed [18] that protons can initially gain kinetic energies approaching this potential, when the laser pulse

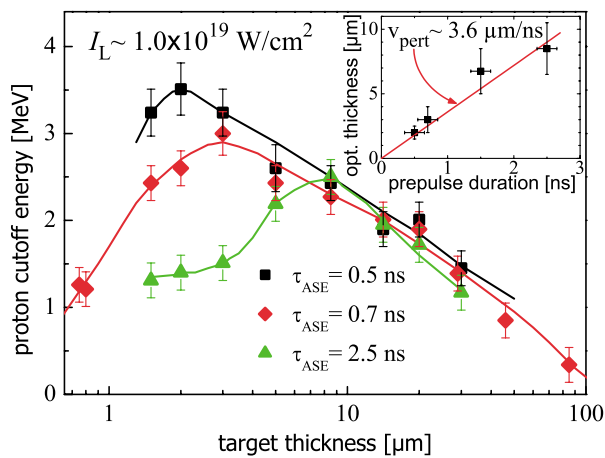


FIG. 1 (color). Proton cutoff energies for differently thick targets and prepulse durations, τ_{ASE} , of 0.5, 0.7, and 2.5 ns, respectively, at $I_L = 1.0 \times 10^{19} \text{ W/cm}^2$. For longer τ_{ASE} , the maximum proton energies are achieved with thicker foils. The inset gives the optimal thickness, depending on τ_{ASE} .

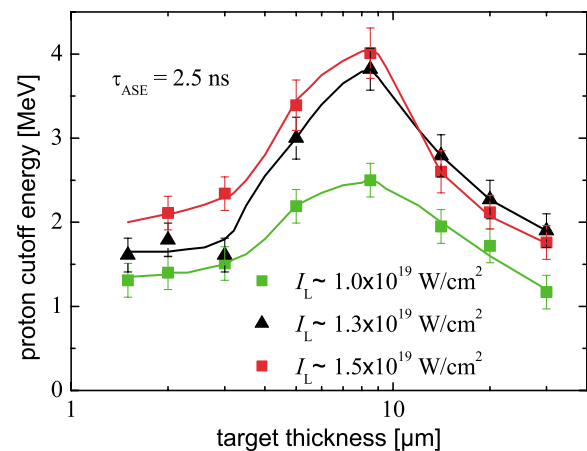


FIG. 2 (color). Proton cutoff energies for differently thick targets and different laser intensities for a prepulse duration of $\tau_{\text{ASE}} = 2.5 \text{ ns}$. The cutoff energies vary with the laser intensity, but the optimal target thickness depends on τ_{ASE} only (cf. Fig. 1).

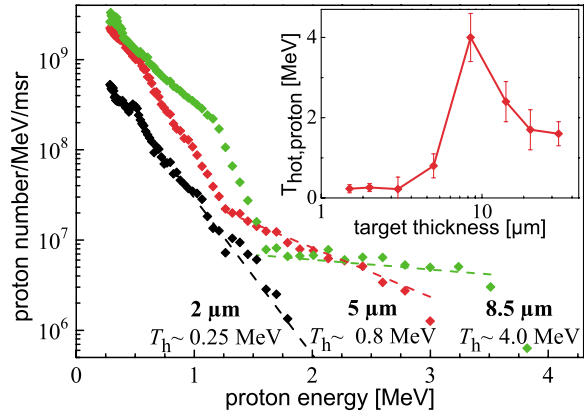


FIG. 3 (color). Proton spectra at $I_L = 1.3 \times 10^{19}$ W/cm² for $\tau_{\text{ASE}} = 2.5$ ns and 2, 5, and 8.5 μm thick foils. With increasing target thickness, a second hotter proton population with much higher cutoff energies appears. The inset gives the temperatures of the hot proton component for all measured thicknesses. A similar behavior is observed for all different τ_{ASE} .

is longer than the acceleration time $\tau_a = \lambda_L/c \times \sqrt{m_p/m_e \gamma_{\text{os}}}$, where m_p is the proton mass. For our conditions, we have $\tau_a = 70$ fs, which is shorter than our pulse duration, and φ_p varies between 0.72 and 0.92 MeV, depending on I_L . During the acceleration, a sharp proton front is formed, that expands afterwards due to an electrostatic repulsion within this front, additionally increasing the peak proton velocity by 50% [18], and thus resulting in cutoff energies of $1.5^2 \times \varphi_p \approx 1.6 \dots 2.1$ MeV for protons accelerated at the front side of the target.

The target normal sheath acceleration (TNSA) mechanism is responsible for proton acceleration from the target rear side [15]. At the front side, a fraction of $\eta \approx 25\%$ of the laser energy is converted into fast electrons having a mean energy of $k_B T_e \approx m_e c^2 (\gamma_{\text{os}} - 1)$ [19], resulting in a total number $N_e \approx \eta E_L / k_B T_e$ of hot electrons that propagate through the target. Arriving at the rear side, only a small fraction of the fastest electrons can escape, while the target charges up. Most of the electrons are held back

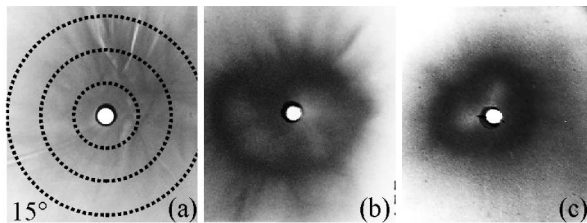


FIG. 4. Proton beam profiles for $\tau_{\text{ASE}} = 2.5$ ns recorded on CR 39 for 2, 5, and 8.5 μm thick targets, respectively. While in (a) the profile is blurred, we observe in (b) and (c) that the major part of the beam is well collimated along the target normal direction. This collimated feature appears only for targets at and above the optimal thickness. The circles in (a) give half-opening angles of 5°, 10°, and 15°, respectively.

by the arising electric field and form a sheath at the rear side with a Debye length of $\lambda_D = \sqrt{\epsilon_0 k_B T_e / n_e e^2}$. This field ionizes atoms at the rear surface and accelerates them in target normal direction. Mora described the acceleration process with 1D simulations [20]. Here, the target consists of preionized hydrogen. The electrons, having a mean energy of $k_B T_e$ during the laser pulse duration, are assumed to be in thermal equilibrium with the electrostatic potential Φ at the target rear side, i.e., $n_e = n_{e0} \times \exp(e\Phi/k_B T_e)$. On the other hand, Φ can be obtained from the Poisson equation $\epsilon_0 \partial^2 \Phi / \partial x^2 = e(n_e - n_p)$, taking into account the electron and proton densities. Initially, the proton density, n_p , is steplike with $n_p = n_{e0}$ in the target. By iteratively solving the equation of motion and the continuity equation for the protons, their new density in the next time step is obtained, leading to a new potential and electric field. As the field is always peaked at the proton front, the fastest protons are also located there. Mora also found an analytical expression for the evolution of the maximum proton energy, E_p , as a function of the interaction time, t_i , depending only on the electron temperature, T_e , and the initial electron density, n_{e0} :

$$E_p \approx 2k_B T_e \left\{ \ln \left[\frac{t_i \omega_{pp}}{\sqrt{2} e E} + \sqrt{1 + \left(\frac{t_i \omega_{pp}}{\sqrt{2} e E} \right)^2} \right] \right\}^2. \quad (1)$$

$\omega_{pp} = \sqrt{n_{e0} e^2 / \epsilon_0 m_p}$ is the proton plasma frequency, that depends on n_{e0} , and $e E = 2.71828 \dots$. We assume $t_i \approx \tau_L$, the same electron numbers and temperatures on both target surfaces, and a constant divergence of the electron beam propagating through the target. The hot electron density at the rear side, n_{e0} , is estimated as follows. Accelerated in the laser focus with an initial radius of $r_f = 2.5 \mu\text{m}$ and a half-opening angle of θ_{in} , the electron beam travels through an effective target thickness of $d_t^* = d_t / \cos 30^\circ$ and leaves it within an area of $\pi(r_f + d_t^* \tan \theta_{\text{in}})^2$. Assuming an electron bunch length of $c \tau_L$, the averaged electron density at the rear side is

$$n_{e0} \approx \frac{N_e}{c \tau_L \times \pi(r_f + d_t^* \tan \theta_{\text{in}})^2}. \quad (2)$$

The peak proton energies for differently thick targets calculated with Eqs. (1) and (2) are compared in Fig. 5 with the experimental results for $I_L = 1.3 \times 10^{19}$ W/cm² and $\tau_{\text{ASE}} = 2.5$ ns. The cutoff energies for targets optimally thick and thicker are well described by this model for an initial half-opening angle of $\theta_{\text{in}} = (8 \pm 2)^\circ$, which is comparable to the value found in [21]. For the same θ_{in} , this model describes also well the results from Fig. 1, when the reduced laser intensity is taken into account.

The cutoff energies for thinner targets cannot be explained by the TNSA mechanism assuming a steplike density gradient at the rear side. Because of the ASE prepulse, a plasma is formed at the target rear surface,

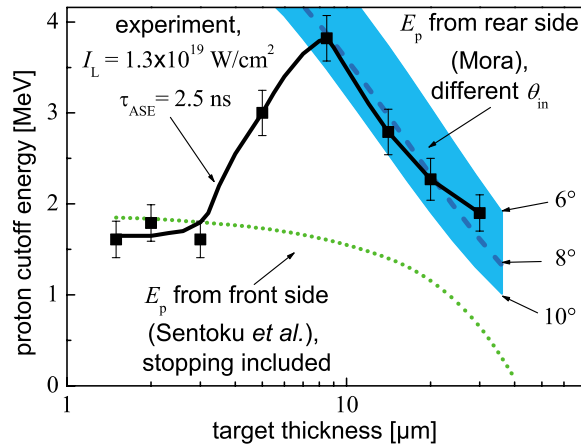


FIG. 5 (color). Comparison of experimental data for $\tau_{\text{ASE}} = 2.5$ ns and $I_L = 1.3 \times 10^{19}$ W/cm² with theoretical predictions. The dotted line gives the cutoff energy for front side accelerated protons including their stopping in the target, while the broad area gives the maximum rear side proton energies for a range of opening angles $\theta_{\text{in}} = (8 \pm 2)^\circ$ of the electron beam.

reducing the acceleration fields [12,19]. We investigated the evolution of this rear side density gradient using the 1D-hydro code MULTI-FS [22]. A simulation for the rear side proton acceleration as described above, that starts with the same rear side density gradient as predicted by MULTI-FS, gives much lower proton cutoff energies for the thinnest foils than those observed in the experiment. Therefore, the rear side acceleration process alone is not able to explain the measured proton energies for all foil thicknesses. On the other hand, protons accelerated at the target front side are not affected by a plasma at the rear side [12]. The maximum energy for front side protons predicted by Sentoku *et al.* [18] reproduces the experimental data much better. Their initial energy is determined by the laser intensity only. The comparison with this model including proton stopping in the target [23] is shown in Fig. 5, yielding a good agreement for the thinnest foils. The increase of the proton cutoff energy for thin targets due to electron recirculation in the target [8] could not be observed, because in our experiment the laser contrast ratio was 500 times lower.

The optimal target thickness is found to depend on the ASE duration only (cf. Figs. 1 and 2). This dependency can be approximated linearly with a slope of $v_{\text{pert}} \approx 3.6 \mu\text{m/ns}$ (cf. Fig. 1). MULTI-FS simulations show that (i) the prepulse launches a shock wave into the target and (ii), the bulk of the target is radiatively heated due to x rays generated in the focus of the prepulse on the target front side. Both effects can cause an expansion of the target. While the shock wave is weak for our prepulse conditions, the radiative heating is sufficiently strong to form a rear side density gradient for the thinnest foils. In contrast, due to the absorption of radiation in the bulk of the target, the formation of a rear side density gradient

sets in at later times for thicker targets. The onset of this plasma formation as observed in MULTI-FS simulations defines the optimal thickness for proton acceleration. The simulation results reproduce the experimentally found value of $3.6 \mu\text{m/ns}$. Although slightly dependent on the ASE intensity, which could not be varied during the experiment, this value can be used to estimate the effect of the prepulse in various laser systems, each having a fixed prepulse duration, on the rear side ion acceleration [9].

In conclusion, we demonstrated a strong influence of the ASE prepulse on the laser-initiated acceleration of protons. An optimal target thickness for the proton acceleration was found. This optimal value depends linearly on the ASE duration and it is determined by a prepulse-induced formation of an ion-density gradient at the rear side of the target. Furthermore, we were able to distinguish between the two main proton acceleration mechanisms, the fastest protons are accelerated from the rear side of the target having the optimal thickness. Analytical estimates support this interpretation. The determination of the optimal target thickness allows a better comparison between existing experimental results and can help to optimize the conditions for proton acceleration for a large range of laser systems in the future.

We thank S. Karsch and P. Mora for fruitful discussions and H. Haas and A. Böswald for the technical support. This work was supported by Euratom-IPP and the EU project SHARP (Contract No. HPRI-CT-2001-50012).

-
- [1] M. Borghesi *et al.*, Phys. Rev. Lett. **88**, 135002 (2002).
 - [2] M. Roth *et al.*, Phys. Rev. Lett. **86**, 436 (2001).
 - [3] A. Maksimchuk *et al.*, Phys. Rev. Lett. **84**, 4108 (2000).
 - [4] E. Clark *et al.*, Phys. Rev. Lett. **84**, 670 (2000).
 - [5] R. Snavely *et al.*, Phys. Rev. Lett. **85**, 2945 (2000).
 - [6] S. Hatchett *et al.*, Phys. Plasmas **7**, 2076 (2000).
 - [7] M. Roth *et al.*, Phys. Rev. ST Accel. Beams **5**, 061301 (2002).
 - [8] A. Mackinnon *et al.*, Phys. Rev. Lett. **88**, 215006 (2002).
 - [9] I. Spencer *et al.*, Phys. Rev. E **67**, 046402 (2003).
 - [10] E. Clark *et al.*, Phys. Rev. Lett. **85**, 1654 (2000).
 - [11] M. Hegelich *et al.*, Phys. Rev. Lett. **89**, 085002 (2002).
 - [12] A. Mackinnon *et al.*, Phys. Rev. Lett. **86**, 1769 (2001).
 - [13] S. Karsch *et al.*, Phys. Rev. Lett. **91**, 015001 (2003).
 - [14] M. Zepf *et al.*, Phys. Rev. Lett. **90**, 064801 (2003).
 - [15] S. Wilks *et al.*, Phys. Plasmas **8**, 542 (2001).
 - [16] A. Pukhov, Phys. Rev. Lett. **86**, 3562 (2001).
 - [17] S. Karsch, Ph.D. thesis [MPQ-Report 279 (2003)].
 - [18] Y. Sentoku *et al.*, Phys. Plasmas **10**, 2009 (2003).
 - [19] S. Wilks *et al.*, Phys. Rev. Lett. **69**, 1383 (1992).
 - [20] P. Mora, Phys. Rev. Lett. **90**, 185002 (2003).
 - [21] J. Santos *et al.*, Phys. Rev. Lett. **89**, 025001 (2002).
 - [22] K. Eidmann *et al.*, Phys. Rev. E **62**, 1202 (2000).
 - [23] <http://physics.nist.gov/>

J. SCHREIBER^{1,2,✉}
M. KALUZA¹
F. GRÜNER²
U. SCHRAMM²
B.M. HEGELICH³
J. COBBLE³
M. GEISSLER¹
E. BRAMBRINK⁴
J. FUCHS^{5,6}
P. AUDEBERT⁵
D. HABS²
K. WITTE¹

Source-size measurements and charge distributions of ions accelerated from thin foils irradiated by high-intensity laser pulses

¹ MPI für Quantenoptik, Hans-Kopfermann-Str. 1, 85748 Garching, Germany

² LMU München, Am Coulombwall 1, 85748 Garching, Germany

³ Los Alamos Natl. Lab, P.O. Box 1663 Los Alamos, NM 87545, USA

⁴ TU Darmstadt, Schloßgartenstr. 9, 64289 Darmstadt, Germany

⁵ Laboratoire pour l'Utilisation des Lasers Intenses,

UMR 7605 CNRS-CEA-École Polytechnique-Univ. Paris VI, Palaiseau, France

⁶ Physics Department, MS-220, University of Nevada, Reno, Nevada 89557, USA

Received: 16 June 2004/Revised version: 8 September 2004
Published online: 26 October 2004 • © Springer-Verlag 2004

ABSTRACT We report on measurements of source sizes and charge state distributions of ions accelerated from thin foils irradiated by ultrashort (100–300 fs) high-intensity ($1 - 6 \times 10^{19}$ W/cm²) laser pulses. The source sizes of proton and carbon ion beams originating from hydrocarbon contaminants on the surfaces of 5 μ m thick aluminum foils were investigated using the knife-edge method. For low-energy protons and low-carbon charge states, the source area was found to exceed the focal spot area by a factor of 10^4 . For the determination of charge state distributions, sandwich targets consisting of a 25 μ m thick tungsten layer, a 2-nm thin beryllium layer, and again a tungsten layer whose thickness was varied were used. These targets were resistively heated to remove the light surface contaminants. Peaked energy spectra of oxygen and argon ions corresponding to the equilibrium distribution after propagation through matter were observed.

PACS 41.75.Jv; 52.38.Kd; 52.25.Jm; 52.50.Jm; 52.70.Nc; 41.75.Ak

1 Introduction

The effective acceleration of ions by ultrashort (30 fs–1 ps) high-intensity (10^{18} – 10^{21} W/cm²) laser pulses interacting with thin foils attracted high attention during recent years. The emitted ion and, in particular, proton pulses reached large particle numbers between 10^{10} and 10^{13} with energies in the MeV- [1, 2] and multi-MeV-range [3–6]. In recent experiments, the high quality of proton beams emitted from the rear side of laser irradiated thin foils was proved [7–9]. On this account, they have been considered as an ion source for the injection into a conventional particle accelerator [10] and for fast ignition [11]. Moreover, laser-accelerated protons were successfully used for diagnosing the electromagnetic fields in overdense laser-produced plasmas with a picosecond time resolution soon after they were first observed [12]. The potential of using protons as an indirect

diagnostic for the electron transport through solid targets has also been demonstrated [13].

The acceleration of ions during the laser-plasma interaction is qualitatively understood. When a laser pulse of relativistic intensity ($I\lambda^2 > 10^{18}$ W/cm² \times μ m²) impinges on a solid surface or a preformed plasma, electrons are accelerated to relativistic velocities within half an oscillation period (1–2 fs for typical laser wavelengths). Simultaneously, they are bent into the propagation direction of the laser pulse because of the $\mathbf{v} \times \mathbf{B}$ -term in the Lorentz-force referred to as ponderomotive potential when cycle-averaged. There are additional mechanisms for energy absorption in presence of steep density gradients ([14] and references therein) which will not be discussed here. However, the ions remain at rest since they are too massive to follow the fast laser oscillation. Thus a quasi-stationary electric field is formed near the critical density surface due to this laser driven charge separation. This is most likely the source of the front-side accelerated ions observed in various experiments [15]. The fastest electrons (\sim MeV mean energy) travel through the foil and escape on their rear-side leaving a charged target behind. With increasing quasi-static electrical potential, slower electrons are no longer able to leave the target. They form a μ m-scale Debye-sheath at the target rear side, where the electric field reaches values in the TV/m-regime. Atoms on the target rear-side experience field ionization and are subsequently accelerated. Emerging from this sheath region, the ions gain kinetic energies of several MeV per nucleon [4, 6, 16]. As the electric field points normal to the target surface, this process is called target normal sheath acceleration (TNSA) [17]. For the laser parameter range and target properties this paper deals with, it has been shown that TNSA is dominant over front-side-acceleration [18, 19].

A series of experiments was performed to investigate the dependence of the observed ion spectra on the intensity [14, 20] and contrast ratio [2, 21] of the laser pulse as well as on different target properties [2, 4, 21]. Although some theories exist reproducing experimental data [22, 23], none of them includes all physically relevant processes. Since in most experiments hydrocarbons contaminated the target surfaces, protons got accelerated predominantly due to their high

✉ Fax: +49-89-32905-200, E-mail: joerg.schreiber@mpq.mpg.de

charge-to-mass ratio and thus were the subject of the most studies. Nevertheless, carbon and even heavier ions of various charge states are usually observed simultaneously under these conditions, albeit with lower number and energy [16, 20, 24]. However, neither the appearance of the observed charge state distributions nor their spatial origin in terms of source size and shape can be explained by the models so far. For the latter, some experimental estimates were already obtained showing that the source size of the rear-side accelerated protons is much larger than the laser focal spot [4, 7–9]. In all these experiments protons were studied. Their number usually exceeds the number of heavier ions by a factor of 100 or more. Additionally, stacks of radiochromic film were used as an ion-detector. These stacks are usually shielded with an aluminum foil, which stops the heavier ions. For a simultaneous source-size measurement of protons and, e.g., carbon ions, the different species and charge states must be separated. In a single shot experiment, this can be done with a Thomson parabola spectrometer only.

A rather simple experiment for source size measurements of protons and carbon ions will be described in Sect. 2 using the knife-edge method. Sect. 3 will address an experiment where oxygen and argon ions could be accelerated. This could be achieved by heating the target to temperatures exceeding 1000°C . Although it is not yet clear if a major fraction of the contaminant elements is removed or if it diffuses into the target, this technique is appropriate for heavy ion acceleration as demonstrated in [16, 24].

2 Source size measurements

The experiments were performed at the ATLAS10 10-Hz-tabletop-laser-system at the MPQ Garching providing laser pulses with energies of about 0.75 J and 150-fs full width at half maximum (FWHM) duration at a center wavelength of 790 nm. Single laser pulses were focused onto 5- μm thick aluminum foils with an incident angle of 30° reaching an intensity of $2 \times 10^{19} \text{ W/cm}^2$ in a spot of 3- μm FWHM diameter. The duration of the amplified spontaneous emission (ASE) was controlled by a fast Pockels cell and chosen to be 1 ns with an intensity contrast of better than 2×10^7 . This pedestal generated a pre-plasma with a scale length of 4 μm at the critical density. Ion spectra were recorded in the target normal direction ($\pm 5 \text{ mrad}$) using a Thomson parabola spectrometer with a pinhole of 300- μm diameter placed 80 cm behind the target (Fig. 1). Nuclear track detectors (CR39) were used inside the Thomson parabola spectrometer to record the ion tracks. After etching, the ion pits were counted by a commercial automated scanning system composed of a computer-controlled optical microscope and a pattern recognition software. This standard experimental setup was extended by the introduction of a scraper placed 8 mm behind the target to perform the knife-edge measurements by moving the scraper across the beam. A stainless steel razor-blade served for this purpose. Since the solid angle of the ion beam ($\sim 25 \text{ msr}$) was about 5 orders of magnitude larger than the detector solid angle (area of entrance aperture of the Thomson parabola spectrometer/(distance to target) 2 , 10^{-4} msr), only a small fraction of the signal passing the scraper was detected (Fig. 1). This is important for the interpretation of the results.

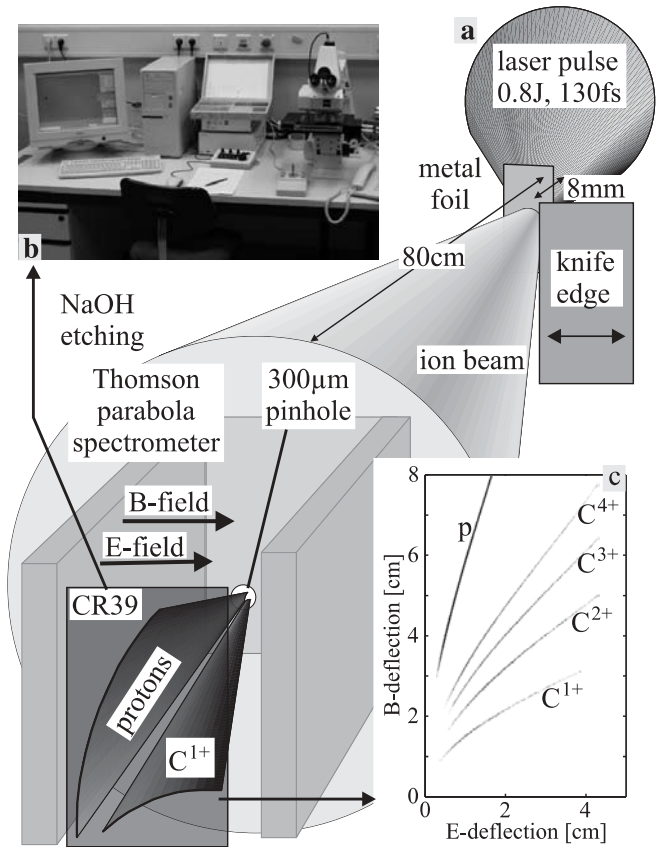


FIGURE 1 Experimental setup. (a) The laser pulse is focused by an off-axis parabola onto the foil target with an incident angle of 30° . The ions are detected in target normal direction with a Thomson parabola type spectrometer using CR39 plastic track detectors. After irradiation they are etched in sodium leauge and scanned by a computer controlled microscope (b). Every single ion track is counted leading to a density image (c) from which the spectra are calculated

Figure 2 shows the spectra of protons and carbon ions with charge states 1+ to 4+ for six selected scraper positions, namely with the scraper at the center of the ion beam (a) and successively moved inwards in 40 μm -steps (b–f). For the next scraper position, following (f) corresponding to 240 μm off center, no ions are detected. The high-energy protons ($E_{\text{kin}} > 0.8 \text{ MeV}$) and highly charged carbon ions (C^{4+} , $E_{\text{kin}} > 2.5 \text{ MeV}$) already vanish after the first scraper step (40 μm) whereas the low-energy protons ($< 0.8 \text{ MeV}$) and the lower carbon charge states appear to be unaffected. The maximum kinetic energy both of protons and C^{4+} -ions decreases with the scraper sliding into the ion beam. Only protons and singly-charged carbon ions remain at the last scraper position (Fig. 2f). The deflection of the ions with the lowest energies was calculated assuming that the scraper is charged with 1 nC. This is a reasonable value for the charge carried by the fast electrons leaving the target. The deflection in the plane of the Thomson parabola spectrometer pinhole was 40 μm and 100 μm for protons and C^{4+} -ions, respectively. Since the pinhole diameter was 300 μm , the influence of the scraper on the passing ions was neglected.

The appearance of only singly ionized carbon in the outer regions indicates a radial decrease in the strength of the quasi-static electric field. As it was discussed in [16], field ionization

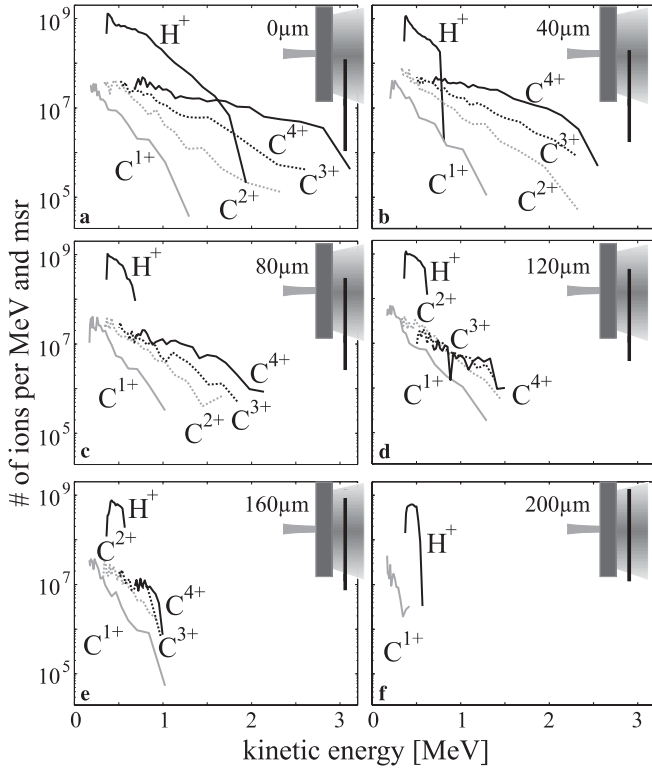


FIGURE 2 Proton and ion spectra for different scraper positions, starting from the center (a)

is the dominant ionization mechanism. In this case, a significant number of ions with a certain charge state can be produced only in regions where the field once exceeded the respective threshold. It thus depicts a lower boundary for the field in this place. The appearance of a maximum ion charge state suggests that the field was never larger than the threshold for the ionization to the next charge state thus giving an upper bound. Although the latter statement implies that no charge exchange occurs after the field ionization process, these assumptions have been used to derive the radial field profile. By reading out the ion spectra of Fig. 2 one can estimate the max-

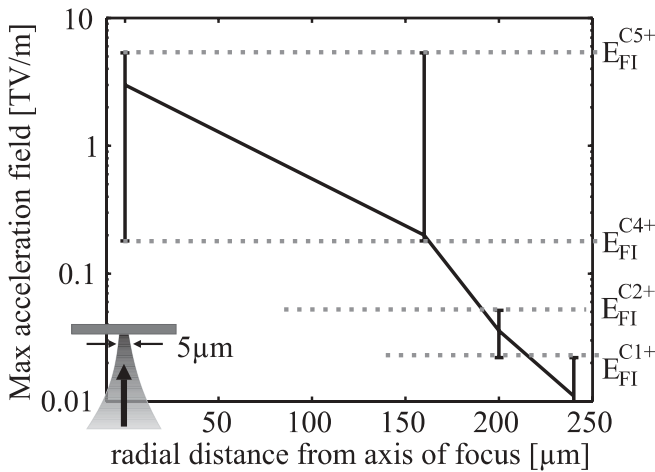


FIGURE 3 Radial profile of the maximum field present during the acceleration process. The error bars represent the threshold fields for field ionization (FI)

imal field which was present during the acceleration process (Fig. 3). The field strength in the center of the emission area was estimated using the formula $E = \sqrt{2/e \times n_{e0} k_b T_e / \epsilon_0}$ [25] where ϵ_0 is the vacuum dielectric constant and e is Euler's constant. The product of the mean energy ($k_b T_e$) and the density of the fast electrons (n_{e0}) can be expressed by $n_{e0} k_b T_e = \eta \cdot I / c$, where I is the laser intensity, c is the velocity of light, and η is the conversion ratio of laser energy into hot electrons chosen to be 10 percent.

Due to the small solid angle of the Thomson parabola spectrometer (10^{-4} msr) as compared to the opening angle of the emitted ion beam (~ 25 msr), the knife-edge method can not be used for the complete characterization of the source. In recent experiments [8], it was shown that the proton beams emitted from the rear side of thin foils exhibit a small normalized emittance ($< 0.004 \pi \text{mm} \times \text{mrad}$). Moreover, their angular divergence depends linearly on the radial distance to the laser focal spot for the considered proton energies. If these results apply to the present case, the ion signal should vanish as soon as the scraper passes the center of the emitting area. In fact this is what happens for the high-energy protons and C^{4+} -ions (Fig. 2a-b). Nevertheless this principle does not seem to apply to the low-energy protons and carbon ions. They might have a larger emittance or emit more straight than the high-energy ions, so ions stemming from the outer areas are able to hit the pinhole of the spectrometer. This could also be caused by a bumpy sheath, where different spatial zones emit ions in target-normal direction. To find a lower constraint for the measured source sizes, it appears most feasible to assume that the ions stem from a circular source, where every point was considered to make the same contribution to the spectrometer signal. For this case, the measured signal can be written as $S = N_0/2 \left[1 - 2/\pi \left(\sin^{-1} x_n + x_n \sqrt{1 - x_n^2} \right) \right]$, where N_0 is the number of ions in a certain energy interval observed without using the scraper and $x_n = 2x_s/s$ is the scraper position x_s divided by the energy-dependent source size s , which is the fit parameter. Figure 4 shows the calculated source sizes of

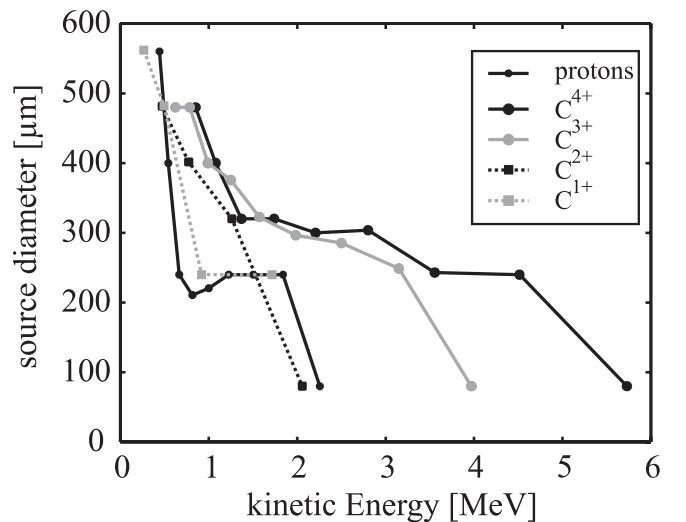


FIGURE 4 Proton and ion source sizes versus kinetic energy. The values represent lower limits for the source diameters

protons and carbon ions as a function of their kinetic energy resulting from the above model assumptions. The denoted values represent a lower boundary for the source diameters except for the high-energy ions. They are confined by the smallest detectable diameter of $80\ \mu\text{m}$, which is twice as high as the scraper step width.

The heavier ions, e.g. carbon, represent only a minor fraction of the total number of ions in experiments using hydrocarbon-contaminated metal targets. This picture changes dramatically once the targets are heated. In this case, protons can be completely removed from the target surfaces resulting in a much larger number and energy of the heavy ions. The next section addresses measurements of charge state distributions of ions accelerated from heated sandwich-targets.

3 Heavy ion measurements – heated targets

In most experiments, hydrocarbon and water contaminants cover the target surface. Here we describe experiments employing resistive heating to remove these contaminants [16]. The 100-TW laser system at the Laboratoire pour l'Utilisation des Lasers Intenses (LULI) at École Polytechnique was used for this campaign. It delivers pulses with an energy of 20 J and a FWHM duration of 320 fs in a focal spot of $6\text{-}\mu\text{m}$ FWHM diameter reaching an intensity of $6 \times 10^{19}\ \text{W}/\text{cm}^2$. Except for the fact that the laser was normally incident and the scraper was removed, the experimental setup was similar to that depicted in Fig. 1. Instead of the aluminum, we used tungsten foils (25 μm) the rear-sides of which were coated with a thin ($\sim 2\ \text{nm}$) beryllium layer followed by a layer of tungsten of variable thicknesses (0–40 nm). This target geometry was chosen aiming at a measurement of the depth profile of the rear-side acceleration field inside the foil by measuring the number of beryllium ions as a function of the tungsten layer thickness. This topic will be discussed in more detail elsewhere. To our surprise, we found oxygen ions from the first up to the sixth charge state in each shot. Since no protons or carbon ions were observed, the oxygen ions most probably originate from oxide layers of the tungsten rather than from water contaminants. Tungsten accumulates an oxide layer similar to aluminum. Furthermore, the 25 μm -tungsten foil was milled under red heat ($\sim 800\ ^\circ\text{C}$) resulting in an oxide-layer buried under the beryllium-tungsten-sandwich structure. Additionally, argon ions (1+ to 8+) were present in some of the shots. This is not surprising since they were used as sputtering projectiles for the target coating process. Usually a small fraction of these ions incorporate into the sputtered layers. The O^{6+} -ions with maximum kinetic energies of 2 MeV/u were the most energetic species measured. Typical spectra of oxygen and argon ions taken from one shot where both species were present are shown in Fig. 5a and b separately.

The total ion spectra were calculated by adding the spectral distributions of the different charge states for both elements. The spectra can be described by double exponential distributions with mean energies of 62 keV/u and 0.4 MeV/u for oxygen and 17 keV/u and 0.1 MeV/u for argon (Insets of Fig. 5a,b). The spectra of the individual charge states are shifted to higher energies with increasing charge. Note the

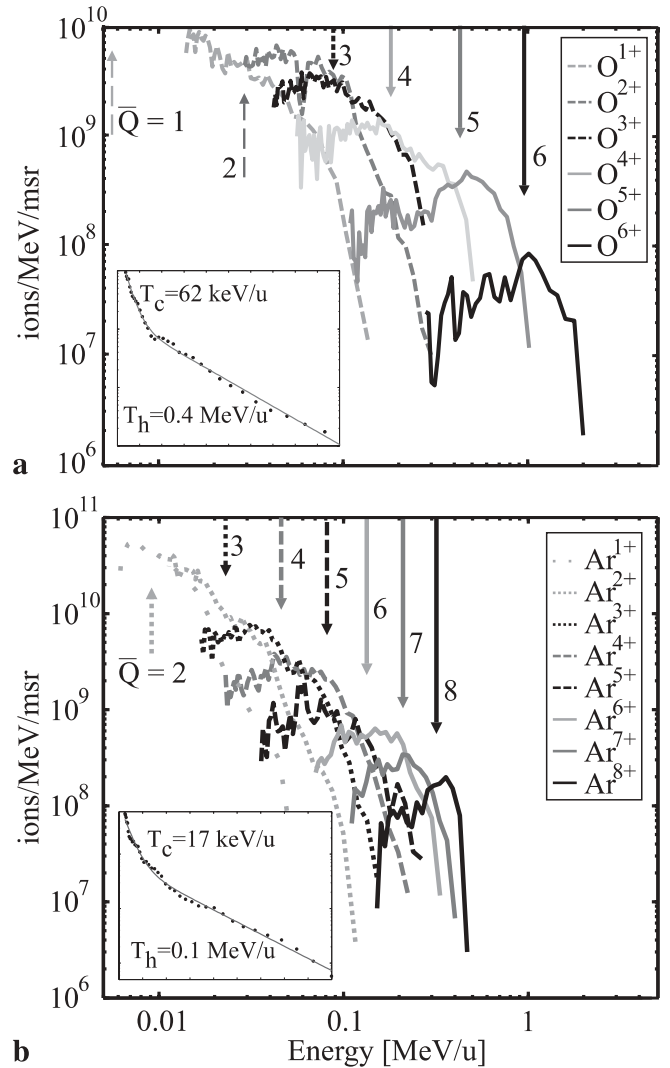


FIGURE 5 Spectra of oxygen (a) and argon (b) ions from an irradiated 25- μm tungsten/2-nm beryllium sandwich-target. The arrows depict the kinetic energy an ion needs to reach the given charge states in case of charge equilibrium. The total spectra of the oxygen and argon ions are shown in the insets. The spectra can be fitted by a double exponential function with mean energies, T_c and T_h

pronounced maxima appearing in the spectral distributions, especially for the higher charge states. The arrows depict the kinetic energies at which the corresponding ions, in case of charge equilibrium, take on the given charge states in solids. The values for O^{4+} to O^{6+} were taken from measured equilibrium charge states for oxygen ions after having passed through gold foils [26], which is close to tungsten. Since experimental data are lacking, the respective values for argon and the lower oxygen equilibrium charge states were calculated using the empirical formula given in [27]. The observed maxima are close to the equilibrium charge states. This finding basically means that the detected ions must have left the foil with their final energy and the corresponding charge state. Taking into account that these ions started at rest, a considerable acceleration distance inside the foil is required. This gives two possibilities for their original locations, because the rear-surface is ruled out as ions originating from there lack sufficient matter to reach charge state equilibrium by electron

exchange reactions. The front-side appears possible, however, oxygen ions need about 100 MeV to traverse 25 μm of tungsten. Therefore, we tentatively propose that the observed oxygen and argon ions came from the bulk of the foil, at least from a thick enough region underneath the rear-surface.

4 Conclusion

Experiments using the knife-edge method were performed to determine the source extension of protons and carbon ions accelerated from thin aluminum foils irradiated with high-intensity laser pulses. The quasi-static electric field was reduced by two orders of magnitude within a radial distance of 200 μm from the laser focus. The source extension of the most energetic protons (> 0.8 MeV) was smaller than 80 μm which is in good agreement with earlier proton source size measurements [4, 8, 9]. Moreover, it was shown that the most energetic C^{4+} -ions (> 2.5 MeV) originate from the same central spot. Source size diameter up to 500 μm were observed for the low energy protons and carbon ions.

In the second experiment oxygen and argon ions emitted from coated tungsten foils were observed. The targets were resistively heated to remove the hydrocarbon and water contaminant layers. The total spectra could be described by double exponential distributions, whereas the individual charge state spectra overlapped and were shifted to higher energies with higher charge states. The observed pronounced maxima were compared to equilibrium charge state distributions well known from stripper-foil experiments in accelerator physics [26, 27]. For the found agreement we have suggested an explanation in terms of starting positions of the detected ions underneath the rear-surface.

ACKNOWLEDGEMENTS This work was supported by grant E1127 from Région Ile-de-France, and UNR grant DE-FC08-01NV14050 as well as DFG HA 1101/7, GSI LM-HA3 and BMBF 06ML184.

REFERENCES

- 1 A.P. Fews, P.A. Norreys, F.N. Beg, A.R. Bell, A.E. Dangor, C.N. Danson, P. Lee, S.J. Rose: *Phys. Rev. Lett.* **73**, 1801 (1994)
- 2 A. Maksimchuk, S. Gu, K. Flippo, D. Umstadter, V.Yu. Bychenkov: *Phys. Rev. Lett.* **84**, 4108 (2000)
- 3 E.L. Clark, K. Krushelnick, J.R. Davies, M. Zepf, M. Tatarakis, F.N. Beg, A. Machacek, P.A. Norreys, M.I.K. Santala, I. Watts, A.E. Dangor: *Phys. Rev. Lett.* **84**, 670 (2000)
- 4 R.A. Snavely, M.H. Key, S.P. Hatchett, T.E. Cowan, M. Roth, T.W. Phillips, M.A. Stoyer, E.A. Henry, T.C. Sangster, M.S. Singh, S.C. Wilks, A. MacKinnon, A. Offenberger, D.M. Pennington, K. Yasuike, A.B. Langdon, B.F. Lasinski, J. Johnson, M.D. Perry, E.M. Campbell: *Phys. Rev. Lett.* **85**, 2945 (2000)
- 5 S.P. Hatchett, C.G. Brown, T.E. Cowan, E.A. Henry, J.S. Johnson, M.H. Key, J.A. Koch, A.B. Langdon, B.F. Lasinski, R.W. Lee, A.J. Mackinnon, D.M. Pennington, M.D. Perry, T.W. Phillips, M. Roth, T.C. Sangster, M.S. Singh, R.A. Snavely, M.A. Stoyer, S.C. Wilks, K. Yasuike: *Phys. Plasmas* **7**, 2076 (2000)
- 6 A.J. Mackinnon, M. Borghesi, S. Hatchett, M.H. Key, P.K. Patel, H. Campbell, A. Schiavi, R. Snavely, S.C. Wilks, O. Willi: *Phys. Rev. Lett.* **86**, 1768 (2001)
- 7 M. Roth, M. Allen, P. Audebert, A. Blazevic, E. Brambrink, T.E. Cowan, J. Fuchs, J.-C. Gauthier, M. Geißel, M. Hegelich, J. Kaae, S. Karsch, J. Meyer-ter-Vehn, H. Ruhl, T. Schlegel, R.B. Stephens: *Plasma Phys. Control. Fusion B* **44**, 99 (2002)
- 8 T.E. Cowan, J. Fuchs, H. Ruhl, A. Kemp, P. Audebert, M. Roth, R. Stephens, I. Barton, A. Blazevic, E. Brambrink, J. Cobble, J. Fernández, J.-C. Gauthier, M. Geißel, M. Hegelich, J. Kaae, S. Karsch, G.P. Le Sage, S. Letzring, M. Manclossi, S. Meyroneinc, A. Newkirk, H. Pépin, N. Renard-LeGalloudec: *Phys. Rev. Lett.* **92**, 204801 (2004)
- 9 M. Borghesi, A.J. Mackinnon, D.H. Campbell, D.G. Hicks, S. Kar, P.K. Patel, D. Price, L. Romagnani, A. Schiavi, O. Willi: *Phys. Rev. Lett.* **92**, 055003 (2004)
- 10 H. Haseroth, H. Hora: *Laser & particle beams* **14**, 393 (1996)
- 11 M. Roth, T.E. Cowan, M.H. Key, S.P. Hatchett, C. Brown, W. Fountain, J. Johnson, D.M. Pennington, R.A. Snavely, S.C. Wilks, K. Yasuike, H. Ruhl, F. Pegoraro, S.V. Bulanov, E.M. Campbell, M.D. Perry, H. Powell: *Phys. Rev. Lett.* **86**, 436 (2001)
- 12 M. Borghesi, S. Bulanov, D.H. Campbell, R.J. Clark, T.Zh. Esirkepov, M. Galimberti, L.A. Gizzi, A.J. MacKinnon, N.M. Naumova, F. Pegoraro, H. Ruhl, A. Schiavi, O. Willi: *Phys. Rev. Lett.* **88**, 135002 (2002)
- 13 J. Fuchs, T.E. Cowan, P. Audebert, H. Ruhl, L. Gremillet, A. Kemp, M. Allen, A. Blazevic, J.C. Gauthier, M. Geißel, M. Hegelich, S. Karsch, P. Parks, M. Roth, Y. Sentoku, R. Stephens, E.M. Campbell: *Phys. Rev. Lett.* **91**, 255002 (2003)
- 14 F.N. Beg, A.R. Bell, A.E. Dangor, C.N. Danson, A.P. Fews, M.E. Glinzky, B.A. Hammel, P. Lee, P.A. Norreys, M. Tatarakis: *Phys. Plasmas* **4**, 447 (1997)
- 15 K. Nemoto, A. Maksimchuk, S. Banerjee, K. Flippo, G. Mourou, D. Umstadter, V.Yu. Bychenkov: *Appl. Phys. Lett.* **78**, 595 (2001)
- 16 M. Hegelich, S. Karsch, G. Pretzler, D. Habs, K. Witte, W. Guenther, M. Allen, A. Blazevic, J. Fuchs, J.-C. Gauthier, M. Geißel, P. Audebert, T.E. Cowan, M. Roth: *Phys. Rev. Lett.* **89**, 085002 (2002)
- 17 S.C. Wilks, A.B. Langdon, T.E. Cowan, M. Roth, M. Singh, S. Hatchett, M.H. Key, D. Pennington, A. MacKinnon, R.A. Snavely: *Phys. Plasm.* **8**, 542 (2001)
- 18 S. Karsch, S. Düsterer, H. Schwoerer, F. Ewald, D. Habs, M. Hegelich, G. Pretzler, A. Pukhov, K. Witte, R. Sauerbrey: *Phys. Rev. Lett.* **91**, 015001 (2003)
- 19 J. Fuchs, Y. Sentoku, S. Karsch, J. Cobble, P. Audebert, A. Kemp, A. Nikroo, P. Antici, E. Brambrink, A. Blazevic, E.M. Campbell, J.C. Fernández, J.-C. Gauthier, M. Geißel, M. Hegelich, H. Pépin, H. Popescu, N. Renard-LeGalloudec, M. Roth, J. Schreiber, R. Stephens, T.E. Cowan: submitted to *Phys. Rev. Lett.*
- 20 E.L. Clark, K. Krushelnick, M. Zepf, F.N. Beg, M. Tatarakis, A. Machacek, M.I.K. Santala, I. Watts, P.A. Norreys, A.E. Dangor: *Phys. Rev. Lett.* **85**, 1654 (2000)
- 21 M. Kaluza, J. Schreiber, M.I.K. Santala, G.D. Tsakiris, K. Eidmann, J. Meyer-ter-Vehn, K.J. Witte: *Phys. Rev. Lett.* **93**, 045003 (2004)
- 22 A. Pukhov: *Phys. Rev. Lett.* **86**, 3562 (2001)
- 23 P. Mora: *Phys. Rev. Lett.* **90**, 185002 (2003)
- 24 M. Zepf, E.L. Clark, F.N. Beg, R.J. Clarke, A.E. Dangor, A. Gopal, K. Krushelnick, P.A. Norreys, M. Tatarakis, U. Wagner, M.S. Wei: *Phys. Rev. Lett.* **90**, 064801 (2003)
- 25 J.E. Crow, P. L. Auer, J.E. Allen: *J. Plasma Phys.* **14**, 65 (1975)
- 26 A.B. Wittkower, H.D. Betz: *At. Data* **5**, 113 (1973)
- 27 K. Shima, T. Ishihara, T. Mikumo: *Nucl. Instrum. Methods* **200**, 605 (1982)

Danksagung

Ich möchte mich bei allen bedanken, die zum Gelingen meiner Arbeit beigetragen und mich in jeder Hinsicht tatkräftig unterstützt haben.

Ich danke Herrn Prof. Dr. Dieter Habs für die Vergabe dieses interessanten und anspruchsvollen Themas sowie für die großzügige Unterstützung mit Rat, Tat, Reise- und Sachmitteln während der gesamten Arbeit.

Großer Dank gilt auch Herrn Prof. Klaus Witte für die liebenswerte Aufnahme in die Laser-Plasma-Gruppe und viele interessante, unterhaltsame und aufschlußreiche Gespräche. Den Kollegen Klaus Eidmann, Ernst Fill und George Tsakiris sowie Malte Kaluza, Matthias Dreher, Jürgen Stein, wie auch unseren technischen Mitarbeitern Harald Haas, Manfred Fischer und Alois Böswald danke ich für den einfachen Start und die mir gegenüber gezeigte Hilfsbereitschaft bei unzähligen Problemen.

Herrn Prof. Ferenc Krausz danke ich für die Übernahme und Erweiterung unserer Gruppe und damit ihrer Rettung sowie für das mir entgegengebrachte Vertrauen.

Herrn Prof. Friedhelm Bell danke ich für das objektive Hinterfragen unserer Methoden und Theorien, was sich als unersetzbare Hilfe herausstellte und schließlich zur Ordnung im Chaos führte.

Ich bedanke mich vielmals bei Ulrich Schramm der mich oft mit Rat und Tat unterstützte und immer mit Begeisterung bei der Sache war. Außerdem hielt er mir wo es nur ging den Rücken frei was das Schreiben von Berichten und Anträgen anbelangte.

Vielen Dank an unseren Theoretiker und PIC-Experten Michael Geissler, der, zusammen mit Jürgen Meyer-ter-Vehn, wie ein Fels in der Brandung unendlich vieler experimenteller Ergebnisse steht und einiges Licht ins Dunkel bringen konnte.

Bei Manuel Hegelich bedanke ich mich für die Einführung in den Kreis vieler Kollaborationen und die Einladungen zu den Experimenten in Los Alamos wie auch für das mir entgegengebrachte Vertrauen.

Ich danke Stefan Karsch für die Bereitstellung seiner Thomson Parabel zu Beginn meiner Arbeit und für die Organisation meines Aufenthaltes am Rutherford-Appleton Lab. Für die Vergabe des Stipendiums danke ich Peter Norreys und dem Team des Imperial College für meine Beteiligung an dem PetaWatt Experiment. Danke auch an das Team vom CLF für die freundliche Aufnahme.

Florian Grüner möchte ich für die Begeisterung für die von mir aufgeworfenen physikalischen Probleme bedanken und schließlich für die Bekanntmachung mit Friedhelm Bell. Florian, Walter Assmann und Andi Bergmaier verdanke ich viele nützliche Tips was schlechtes Vakuum bzw. Unterdruck angeht und natürlich die Charakterisierung etlicher Targets, so daß wir schlußendlich doch wußten worauf wir schießen.

Ohne die Target-Produktion durch Dagmar Frischke und Hans-Jörg Maier im Target-Lab der LMU und die schnelle Hilfe in unserer Werkstatt am MPQ wären viele Experimente nicht möglich gewesen, auch dafür vielen Dank.

Dem Team von LULI gilt mein Dank für einen fantastisch laufenden Laser. Speziell Julien Fuchs und Patrick Audebert möchte ich für die interessanten Experimente und die unzähligen Stunden im Labor danken, bei denen ich etliches dazulernen konnte.

Auch dem Team vom MBI, Berlin sei hier Dank gesagt für das vergleichsweise glatt laufende Experiment mit Matthias Schnürer und Sargis Ter-Avetisyan und die schnelle Veröffentlichung der Resultate.

Danke auch an das Phelix Team an der GSI, Darmstadt, wo wir nach einigen Anlaufschwierigkeiten doch noch ein Paar Experimente zustande brachten. Besonderer Dank gilt an dieser Stelle auch Erik Brambrink für einige interessante Nächte im Labor mit dem fulminanten Höhepunkt des explodierenden Verstärkerkopfes.

Für schöne und produktive 2 Wochen in Los Alamos danke ich neben Manuel Hegelich auch Kirk Flippo und Juan Fernández sowie dem TRIDENT laser team am LANL.

Vielen Dank an meinen lieben Schatz Ute, für die Liebe, Geduld und das Verständnis, daß sie mir in all den Jahren entgegengebracht hat, und für unser Krümelchen, das süßeste und wunderbarste Geschenk, daß man sich vorstellen kann.

Natürlich möchte ich mich an dieser Stelle auch bei meinen Eltern für ihre jahrzehnte lange Unterstützung und Geduld bedanken. Ich hoffe inständig meinem Kind einen eben so schönen Weg zu bereiten wie sie es für mich getan haben.

Lebenslauf

Persönliche Daten

Name	Jörg Schreiber
Geburtstag/-ort	19.11.76 in Suhl
Familienstand	ledig
Staatsangehörigkeit	deutsch

Schulbildung

9/82 - 8/83	1. Klasse, Botschaftsschule der DDR, Genf, Schweiz
9/83 - 8/91	4. POS, Gesamtschule, Suhl
9/91 - 5/95	Goethe-Gymnasium, Spezialklasse für Mathematik und Naturwissenschaften, Ilmenau

Militärdienst

7/95 - 6/96	Pioniertaucher, Volkach
-------------	-------------------------

Studium

10/96 - 3/97	Architektur an der Bauhaus- Universität Weimar
4/97 - 3/01	Studium der Physik an der Friedrich- Schiller-Universität, Jena
4/01 - 3/02	Diplomarbeit am Institut für Op- tik und Quantenelektronik, Prof. Sauerbrey: <i>Erzeugung und Charak- terisierung von frequenzverdoppelten ultrakurzen Terawatt Titan-Saphir- Laserimpulsen</i>

Beschäftigung während des Studiums

von 1998 bis 2002	Studentischer Mitarbeiter am IOQ, FSU Jena
von 1998 bis 2002	Studentischer Mitarbeiter am Biomagnetischen Institut der FSU Jena
von 01/07/1999 bis 31/08/1999	DAAD Stipendium für Kollaboation mit dem biomagnetischen Zentrum der Universität von Washington, USA

Arbeitserfahrung

von 01/05/2002 bis 31/08/2002	Wissenschaftlicher Mitarbeiter am Biomagnetischen Zentrum der FSU Jena
-------------------------------	--

Promotion

von 10/2002 bis 6/2006	an der Universität München, Lehrstuhl Habs und am Max-Planck-Institut für Quantenoptik in Garching bei München
------------------------	--

Auslandsaufenthalte und Experimente in Kollaborationen

von 01/07/2003 bis 31/08/2003	LULI, Ecolé Polytechnique, Palaiseau, France
von 01/05/2004 bis 31/07/2004	Marie-Curie-Stipendium, central laser facility (CLF), Rutherford Appleton Laboratory (RAL), Chilton, Didcot, England
von 10/10/2004 bis 20/11/2004	LULI, Ecolé Polytechnique, Palaiseau, France
von 14/02/2005 bis 09/03/2005	MBI, Berlin
von 23/05/2005 bis 13/06/2005	Los Alamos National Laboratories, Los Alamos, USA
von 14/06/2005 bis 24/06/2005	CLF at RAL, Chilton, Didcot, England

von 06/02/2006 bis 03/03/2006 GSI Darmstadt

Sprachen

Englisch

fließend in Wort und Schrift

Russisch

8 Jahre Schulbildung